KAUNAS UNIVERSITY OF TECHNOLOGY

JOLITA SAKALIŪNIENĖ

MATERIALS AND MICROSTRUCTURES FOR MICRO-SOLID OXIDE FUEL CELLS

Doctoral dissertation
Technological Sciences, Materials Engineering (08T)

2017, Kaunas

KAUNO TECHNOLOGIJOS UNIVERSITETAS

JOLITA SAKALIŪNIENĖ

MEDŽIAGOS IR MIKROSTRUKTŪROS KIETOJO OKSIDO KURO MIKROELEMENTAMS

Daktaro disertacija
Technologijos mokslai, Medžiagų inžinerija (08T)

2017, Kaunas

Interneto svetainės, kurioje skelbiama disertacija, adresas:
http://ktu.edu

Redagavo:

Dovilė Dumbrauskaitė (leidykla „Technologija")

Dedicated to

my Family

Acknowledgements

TABLE OF CONTENTS

10

LIST OF FIGURES

15

LIST OF TABLES

16

LIST OF ABBREVIATIONS AND SYMBOLS

E_a	− activation energy
f_i	− activity coefficient of the i component
AC	− alternating current
I_0	− amplitude of the current
σ	− amplitude of the residual stresses
E_0	− amplitude of the signal
S	− area of the electrodes
AFM	− atomic force microscopy
ALD	− atomic layer deposition
M	− atomic weight
D_{BET}	− average particle size
N_A	− Avogadro constant
BSE	− backscattered electrons
BSCF	− barium strontium cobalt iron oxide
k	− Boltzmann's constant ($0.86 \cdot 10^{-4}$ eV K^{-1})
BET	− Brunauer Emmett Teller
$\Delta E_{b,gb}$	− bulk and grain boundary conductivities
Y_0	− capacitance
q_i	− charge
CVD	− chemical vapour deposition
C_A^S	− concentration of element A in the vapour phase
C_B^S	− concentration of element B in the vapour phase
CP	− co-precipitation method
I	− current
SPM	− data processing
DRIE	− deep reactive ion etching
DSC	− differential scanning calorimetry
DTA	− differential thermal analysis
DC	− direct current
h	− distance between electrodes
x	− dopant concentration
S_1	− elasticity constants that can be expressed as a function of the Young's modulus
S_2	− elasticity constants that can be expressed as a function of the Young's modulus
R	− electrical resistance
ER	− electrical resistivity
EB-PVD	− electron beam physical vapour deposition
ESCA	− electron spectroscopy for chemical analysis
σ_{el}	− electronic conductivity
EDX	− energy dispersive X-ray analysis
α	− evaporation coefficient
F_{max}	− evaporation rate
F_i	− evaporation rate of separate component
F	− Faraday's constant (96485 C·mol^{-1}),

x_d	– fraction of dopant
GDC	− gadolinia doped ceria
GI-XRD	− grazing incidence X-ray diffraction
HT	− high temperature
IS	− impedance spectroscopy
θ	− incident angle
IWI	− incipient wetness impregnation
ICP	− inductively coupled plasma
ICP-OES	− inductively coupled plasma optical emission spectrometry
IR	− infrared
C_A^0	− initial concentrations of element A in the target material
C_B^0	− initial concentrations of element B in the target material
$N^0 = N_A^0 + N_B^0$	− initial number of molecules in the evaporated compound
IT	− intermediate temperature
ICDD	− International Centre for Diffraction Data
d_0	− interplanar distance
IBE	− ion beam etching
σ_i	− ionic conductivity
r_d	− ionic radius of dopant
r_O	− ionic radius of oxygen
JSC	− Joint-stock company
R_{ku}	− kurtosis, measure of the height randomness and sharpness of a surface
LSC	− lanthanum strontium cobalt oxide
LSCF	− lanthanum strontium cobalt iron oxide
a	− lattice parameter
LPCVD	− low pressure chemical vapour deposition
LT	− low temperature
LSGM	− magnesium-doped lanthanum gallate
m	− mass of molecule
μ-SOFC	− micro solid oxide fuel cell
μ_i	− mobility of the species
M_A	− molecular weight of element A
M_B	− molecular weight of element B
NMP	− N-methylpyrrolidone
n_i	− number density
n	− number of oxygen moles
$j(O_2)$	− oxygen flux
$V_O^{\cdot\cdot}$	− oxygen vacancy
r_{vo}	− oxygen vacancy
$P_{O_2,2}$	− partial oxygen pressures at another side of an electrolyte
$P_{O_2,1}$	− partial oxygen pressures at one side of an electrolyte
$p_a(O_2)$	− partial pressure of oxygen at the anode electrodes
$p_c(O_2)$	− partial pressure of oxygen at the cathode
ϕ	– phase shift

PVD	− physical vapour deposition
v	− Poisson ratio
PEN	– Positive electrode/Electrolyte/Negative electrode
E_t	− potential at time t
PDF	− powder diffraction files
σ_0	– pre-exponential factor
s	− probe spacing
PLD	– pulsed laser deposition
ω	– radial frequency
RF	− radio frequency
r_{Ce}	− radius of the cerium ion
RIE	− reactive ion etching
C_i	− relative concentration of component i
ρ	− resistivity
I_t	− response signal
R_q	− root mean square roughness, the average of the measured height deviations taken within the evaluation area and measured from the mean linear surface
SDC	− samarium-doped ceria
p_{As}	− saturated vapour pressure of element A at evaporation temperature
p_{Bs}	– saturated vapour pressure of element B at evaporation temperature
p_{si}	− saturated vapour pressure of component i
ScSZ	− scandia stabilized zirconia
SEM	− scanning electron microscopy
SE	− secondary electrons
STA	− simultaneous thermal analysis
SLR	− single-lens reflex
R_{sk}	− skewness, negative skewness indicates predominance of valley while a positive value indicates a surface dominated by peaks
SOFC	− solid oxide fuel cell
S_{BET}	− specific surface area
$\varepsilon_{\phi\psi}$	− strain in (ϕ, ψ) direction
T	− temperature
t	− the film/wafer thickness
d	− the spacing between diffracting planes or an iterplanar distance
d_{th}	− theoretical density of the solid solution oxide
TGA	− thermogravimetric analysis
TG-DSC	− thermogravimetric and differential scanning calorimetry
TG	− thermogravimetry
TG-DSC	− thermogravimetry-differential scanning calorimetry
TG-DTA	− thermogravimetry-differential thermal analysis

20

L	− thickness of the electrolyte
t	− time
TPB	− triple-phase boundaries
UV	− ultraviolet
R_u	− universal gas constant
p_v	− vapour pressure
$E; E_t$	− voltage; voltage at time t
λ	− wavelength
RCA-1	− wet chemical cleaning method with a base-peroxide mixture
XRD	− X-ray diffraction
XPS	− X-ray photoelectron spectroscopy
E	− Young's modulus
YSZ	− yttria-stabilized zirconia

ABSTRACT

This dissertation is dedicated to the development and improvement of the μ-SOFC manufacturing process by applying microelectromechanical system (MEMS) technologies with respect to the properties of μ-SOFC construction elements, such as electrode (anode and cathode), as well as electrolyte materials and thin films.

The co-precipitation synthesis and incipient wetness impregnation methods were tailored for the synthesis of YSZ and GDC micro- and nanostructures (ceramics), further used as a target in the electron beam evaporation technique for the deposition of μ-SOFC electrolyte thin films. A comprehensive study of ceramics and thin films was performed and presented.

The deviation of stoichiometry in the evaporated thin films, compared to the original target (ceramics) composition, was observed. It was shown that stoichiometry deviations in thin films may reach more than 30%. Synthesized oxygen vacancy conducting ceramics and thin films evaporated on Al_2O_3 and SiO_2/Si substrates have been studied by impedance spectroscopy. In order to investigate electrical properties of electrolyte thin films, several configurations of the Pt electrode were applied.

The photomasks were designed and produced. Also the design of geometry and technological route of μ-SOFC manufacturing process was developed and tested. The photomasks were fabricated from chromium and soda lime glass. The manufacturing process involved back-side photolithography, magnetron sputtering of platinum thin films, electron beam evaporation of YSZ or GDC electrolyte, deep reactive ion etching of silicon, and, finally, the release of free-standing membrane. The technological route of the micro-solid oxide fuel cell was modified during an investigation using direct Ar^+ ion beam etching of platinum and YSZ or GDC electrolyte thin films instead of lift-off lithography technique. Test samples of the μ-SOFC three-layered structure, sometimes called PEN (Positive electrode-Electrolyte-Negative electrode) membrane structures, were fabricated. The cell diameter was about 2.4 mm with the electrolyte and total cell thickness of about 600 and 1000 nm, respectively.

Suitable conditions and technological parameters for the manufacturing of μ-SOFC test sample were chosen. It was determined that the formation of positive/negative Pt electrode with appropriate properties, such as structure, morphology and porosity, is possible through controlling both deposition conditions (argon gas pressure in the chamber) during the magnetron sputtering process and by applying additional thermal treatment. It was found that Pt electrodes sputtered at 0.065 Pa argon gas pressure in the chamber and thermally treated at 600°C for 15 min reveal nanopores, which remain open after exposure at 800°C, even with increasing annealing duration. Thus, optimal conditions and additional thermal treatment were employed in order to create a PEN structure exhibiting the required mechanical, thermal stability, structural, and electrical properties.

INTRODUCTION

Lately, the development of small mobile electronic devices such as smartphones, laptops, portable digital assistants, camcorders, medical implements, industrial scanners or drones, usually powered by rechargeable batteries, has increased dramatically. These devices are projected to increase at faster rate than the capacity of rechargeable batteries. Therefore, it becomes difficult to supply reasonable operating time without increasing battery size [1–3].

Thus, the demand for mobile energy is constantly growing in our society and new generation, high power and long-use power sources are required. One of the promising and environmentally friendly electrochemical energy conversion devices is a solid oxide fuel cell (SOFC) [4–6]. It is designed for stationary applications in high power range, i.e. several 100 kW to the 1 MW region, while state-of-the-art miniaturized solid oxide fuel cell (μ-SOFC) is foreseen for lower power applications in the range of 1–20 W [2] and may be used in domestic applications of innovative small scale Combined Heat and Power (CHP) prime movers [7]. μ-SOFCs are predicted to be very attractive electrochemical power sources for portable devices due to their high efficiency and energy density compared to conventional rechargeable batteries, such as lithium ion and nickel metal hydride batteries [2,4,8–10]. Moreover, μ-SOFCs are desirable due to the capability of operating on different handle and secure fuels, such as methane, ethane, and compressed butane [11].

Manufacturing of μ-SOFC has been extensively studied in last decade. Usually, μ-SOFC is developed by adopting microfabrication, or microelectromechanical system (MEMS) fabrication techniques [12]. The process implies bulk and surface micromachining using lithography, wet and dry etching, and thin film deposition [13]. As a result, any massive fabrication of certain MEMS-based products requires a comprehensive analysis which would ensure qualitative, efficient and relatively easy manufacturing of appropriate goods. μ-SOFCs consist of a fuel cell membrane supported on a micromachinable substrate material, typically on Si wafers. The thickness of the anode/electrolyte/cathode membrane is in the micron range, requiring thin film preparation methods for the electrodes and the electrolyte with film thicknesses of not more than several hundred nanometers each [14]. Therefore, the design and geometric solutions of the μ-SOFC manufacturing, as well as properties of materials used in the nanometre range are crucial at this time.

Despite the aforementioned advantages of μ-SOFC, the commercialization of the technology and practical application of μ-SOFC systems has not fully succeeded [15]. They have extremely short lifetime, mainly due to the instability of nano-porous metal electrodes. In addition, free-standing membranes frequently buckle or fracture during fabrication and operation, thus the survival probability of the free-standing membrane upon thermal cycling is poor. These problems may arise mainly due to the low thermal expansion coefficient of Si substrate. More efforts are now being made to increase the stability of the cell. In respect of stability control, the supported-membrane design is superior because it can provide the mechanical strength required to support the thin-film membrane. Although various

designs, geometrical solutions and material preparation methods have been proposed, some problems, such as mechanical, chemical or thermal stability related to high operating temperatures of the cell still remain. Recently, SOFC and µ-SOFC systems have existed only as prototypes due to high cost and long payback period for consumers and are still not competitive in the energy market [15]. As mentioned earlier, the main problem is related to high operating temperatures of these devices. Due to high temperatures, special materials are required, especially for high temperature sealing and current collection [15]. To sum up, high cost and technological immaturity of fuel cells relate to the expensive materials and techniques used in the process of cell manufacturing as well as maintenance. Due to the fact that all the degradation mechanisms are based on thermally activated processes, the considerable lowering of operation temperature in combination with a miniaturization of the device may diminish the aging issues [11].

As a result, the search of new and inexpensive materials exhibiting appropriate properties, as well as synthesis methods which could reduce the overall cost are of potential interest. However, conventional zirconia- and ceria-based ceramics used as electrolytes in the µ-SOFC manufacturing process are irreplaceable materials and still widely used due to their stability and sufficiently high ionic conductivity at reducing environments compared to the new materials [16]. Various advanced synthesis techniques may be employed for the fabrication of electrolyte ceramic powder. However, the choice of the synthesis route may influence the properties of materials, moreover – fuel cell performance and definitively cost. In this research, significantly low-cost co-precipitation synthesis method was applied obtaining electrolyte materials. It was shown that this method leads to an easier synthesis of electrolyte ceramics with the required properties by changing a process parameter, e.g. pH value of the solution. The structural and electrical properties of obtained ceramics were thoroughly investigated by varying the concentration of the dopant. In addition, a simple impregnation method was tailored.

In the development of µ-SOFC systems, high quality, ionic conductivity, and dense electrolyte thin films are required [17,18]. Preferably, an ultra-thin and dense electrolyte membrane is deposited on a Si wafer and electrodes are placed on the electrolyte membrane after removing the Si by lithography and etching [19]. Various effective deposition techniques, such as pulsed laser deposition (PLD), magnetron sputtering, electron beam evaporation (EB-PVD) or other physical (or chemical) vapour deposition techniques may be employed for the fabrication of electrolyte or electrode thin films in the sub-micron range. EB-PVD technique was tailored for the formation of electrolyte thin films in this research. There are some challenges related to the evaporation of composite material; however, the significant advantages, such as high deposition rates, simple operation and, most importantly, the possibility to form dense, crystalline thin films of electrolyte material with a columnar structure on large areas desired for µ-SOFC electrolyte applications, overcomes disadvantages.

Now, as energy issues are at the forefront of current events, fuel cell technology is ripening and on the verge of being ready for large-scale commercial implementation [16]. Since recent high priority is paid to search for new electrode,

electrolyte, and support materials used in the μ-SOFC manufacturing process, it is necessary to improve the electrical and ionic conductivity properties as well as catalytic activity of conventional and still irreplaceable and excellent performance materials. This thesis reviews the synthesis of conventional electrolyte materials currently used in the fabrication of μ-SOFC electrolyte thin films, together with the design and manufacturing of the cell. To sum up, this dissertation covers the properties of μ-SOFC construction elements involving electrolyte and electrode materials as well as thin films with a focus on requirements for manufacturing of μ-SOFC membrane structure. Microstructure, electrical properties, chemical composition behaviour of materials, and thin films were comprehensively reviewed.

Motivation

Micro-solid oxide fuel cells (μ-SOFCs) are considered promising power sources for portable devices which occupy a major part of the energy market. The widest application of μ-SOFC should occur approximately after 20 years. The implementation of μ-SOFC in the industry is still complicated due to high cost and operating temperature, also a complex manufacturing process. Moreover, new or improved conventional materials along with the manufacturing of high performance thin films are required.

Thus, the desire of this type of energy has motivated research on the development and improvement of the μ-SOFC manufacturing process with respect to the study of materials and formation of μ-SOFC construction elements (electrodes and the electrolyte). In terms of materials, it was aimed to improve the ionic conductivity of the electrolyte at a lower temperature and to provide a stable device. The achievement of these goals would mean a technological breakthrough and a further step towards industrial production of μ-SOFC [15].

Research objective

The aim of this work is to develop a manufacturing process for the multi-layered membrane of micro-solid oxide fuel cell (μ-SOFC) with respect to the synthesis of metal oxide materials, formation of thin films, and application of microelectromechanical system processing.

Tasks of the dissertation

1. To apply the co-precipitation synthesis and impregnation technique in order to synthesize ceramics with appropriate properties necessary for μ-SOFC electrolyte material, and to use these electrolytes in the thin film manufacturing by electron beam evaporation technique with respect to the chemical composition of the ceramics (target).

2. To characterize the structural and electrical properties of synthesized electrolyte materials and electron beam evaporated thin films.

3. To adjust the magnetron sputtering process for the formation of μ-SOFC electrode (anode and cathode) thin films with the required structure, morphology and electrical properties by varying the magnetron sputtering process parameters and applying additional thermal processing.

4. To contribute to the development of the technological route for the production of μ-SOFC multi-layered membrane structure by using thin film deposition and microelectromechanical system (MEMS) processing techniques.

Scientific novelty of the work

1. The electron beam evaporation technique was successfully applied for the deposition of high quality and manageable chemical composition thin films which may be used as the electrolyte in μ-SOFC (thickness up to 1 μm) by changing the elemental composition of the target material in the evaporation process.

2. A comparative analysis of methods for measuring the impedance spectroscopy of electrolyte thin films in the wide range of frequencies was performed.

3. An original technological route for manufacturing the μ-SOFC multi-layered membrane structure compatible with the thin film formation and microelectromechanical system technologies was proposed.

The key statements of the dissertation

1. The co-precipitation and incipient wetness impregnation for the synthesis of electrolyte materials (yttria stabilized zirconia, gadolinia doped ceria, and yttria stabilized zirconia doped ceria) are suitable methods which ensure the precise control of elemental composition. The synthesized ceramics may be further used as target materials in the electron beam evaporation technique.

2. In the application of impedance spectroscopy measurements for electrolyte thin film analysis it is necessary to correctly select the configuration of electrodes.

3. Magnetron sputtering deposition, electron beam evaporation and following thermal annealing conditions to produce three-layered positive electrode-electrolyte-negative electrode structure were identified.

Structure of the dissertation

This dissertation is organized as follows. Chapter 1 presents the literature review. It covers the work principles and the existing designs of μ-SOFC; materials and their requirements; synthesis routes; the formation of electrolyte and electrode thin films and finally, an overview of the technological routes for the manufacturing of μ-SOFC.

Chapter 2 presents the materials, provides short descriptions and experimental details of the basic technological and analytical methods used in this thesis.

The obtained results are divided into three parts and presented in Chapter 3 as follows: the first part is devoted to the development and characterization of electrolyte materials and the preparation of thin films; the second part is related to the characterization and formation of electrodes in a form of sputtered thin films; and the third one reveals the development of technological route designed for manufacturing μ-SOFC.

Chapter 4 gives an overall discussion, conclusions and reviews potential improvements for the future technologies.

This dissertation consists of 138 pages, including 73 figures and 17 tables. The list of references contains a total of 203 items.

Personal input of the author

Most results presented in the dissertation were obtained at Kaunas University of Technology. The author has planned all experiments and carried out the technological as well as analytical processes, personally performed the co-precipitation synthesis and formation of electrolyte thin films using the electron beam evaporation technique. The research was funded by the National Research programme "Future energy" project "Technological processes of membranes production for micro-solid oxide fuel cells" (MIKROKOKE-2) in which the author participated as a junior researcher.

Incipient wetness impregnation synthesis of the ceramics was performed by Dr. María del Pilar Yeste Sigüenza from Cadiz University. Dr. Tomas Šalkus from Vilnius University and Edvinas Navickas from Vienna University of Technology performed the impedance measurements of thin films by Agilent E5062A and Alpha-A network analyser, respectively. Colleagues from the Institute of Materials Science who contributed to this work: Vitoldas Kopustinskas accomplished the direct Ar^+ ion beam etching of structures; Dr. Kęstutis Šlapikas carried out the formation of platinum electrodes using magnetron sputtering; Assoc. Prof. Dr. Mindaugas Andrulevičius performed X-ray photoelectron spectroscopy measurements; Dr. Igoris Prosyčevas and Valentinas Baltrušaitis advised on the matters concerning co-precipitation synthesis route. The analysis and interpretation of results was performed by the author in consultation with the scientific supervisor Prof. Habil. Dr. Sigitas Tamulevičius and the scientific advisor Assoc. Prof. Dr. Brigita Abakevičienė from Kaunas University of Technology.

Approbation of the research results

The original results of this research were published in four scientific publications: three of them in research journals indexed by the Web of Science (Thomson Reuters) and one in proceedings. The results have been presented at 13 international (the author personally participated in 7 conferences; 1 oral and 6 poster presentations were presented) and 2 national conferences (the author personally participated in 2 conferences; 1 oral and 1 poster presentation was presented).

List of publications related to the dissertation

1. Abakevičienė, Brigita; Grigaliūnas, Viktoras; Sakaliūnienė, Jolita; Virganavičius, Dainius; Šlapikas, Kęstutis; Mikolajūnas, Marius; Tamulevičius, Sigitas. Modelling and fabrication of micro-SOFC membrane structure // Materials science = Medžiagotyra / Kaunas University of Technology, Academy of Sciences of Lithuania. Kaunas: KTU. ISSN 1392-1320. 2014, Vol. 20, no. 2, p. 223-227. [Science Citation Index Expanded (Web of Science); Inspec; Scopus]. [IF (E): 0,510 (2014)]

2. Sakaliūnienė, Jolita; Abakevičienė, Brigita; Šlapikas, Kęstutis; Tamulevičius, Sigitas. Influence of magnetron sputtering deposition conditions and

thermal treatment on properties of platinum thin films for positive electrode–electrolyte–negative electrode structure // Thin solid films. Lausanne: Elsevier. ISSN 0040-6090. 2015, vol. 594, part A, p. 101-108. [Science Citation Index Expanded (Web of Science); Current Contents (Physical, Chemical & Earth Sciences); Current Contents (Engineering, Computing & Technology); Science Direct]. [IF (E): 1,761 (2015)]

3. Žarkov, Aleksej; Stanulis, Andrius; Sakaliūnienė, Jolita; Butkutė, Skirmantė; Abakevičienė, Brigita; Šalkus, Tomas; Tautkus, Stasys; Orliukas, Antanas Feliksas; Tamulevičius, Sigitas; Kareiva, Aivaras. On the synthesis of yttria-stabilized zirconia: a comparative study // Journal of sol-gel science and technology. New York: Springer Science+Business Media. ISSN 0928-0707. 2015, vol. 76, iss. 2, p. 309-319. [Science Citation Index Expanded (Web of Science); SpringerLINK]. [IF (E): 1,473 (2015)]

4. Sakaliūnienė, Jolita; Abakevičienė, Brigita; Muñoz Fuentes, Miguel Ángel; Cauqui López, Miguel Ángel; Tamulevičius, Sigitas; del Pilar Yeste Sigüenza, María. Pelicula delgada de CeO$_2$-YSZ depositadas mediante evaporacion por haces de electrones: uso como interfase electrodo-electrolito en las µ-SOFC // Libro de comunicaciones: II congreso Iberoamericano de Hidrógeno y Pilas de Combustible, 20-22 April 2016, Torremolinos (Málaga). Madrid: Asociación Española de Pilas de Combustible - APPICE, 2016, ISBN 9788460866145. p. 117-120.

List of conference contributions related to the dissertation

1. Sakaliūnienė, Jolita; Abakevičienė, Brigita; Šalkus, Tomas; Tamulevičius, Sigitas. Characterization of YSZ and GDC thin films evaporated by e-beam technique // E-MRS Spring Meeting 2013, May 27th-31st, Strasbourg, France. Strasbourg: European Materials Research Society, 2013. p. P.III-26.
2. Sakaliūnienė, Jolita; Rajackaitė, Erika; Šalkus, Tomas; Kazlauskas, Saulius; Kežionis, Algimantas; Abakevičienė, Brigita. Investigation of structural and electrical properties of YSZ nanopowders and ceramics synthesized by coprecipitation method // SSI-19 : 19th international conference on solid state ionics, June 2-7, 2013, Kyoto, Japan : book of abstracts / Solid State Ionics Society of Japan. [S.l.: s.n, 2013]. p. Thu-D-107.
3. Sakaliūnienė, Jolita; Virganavičius, Dainius; Abakevičienė, Brigita; Grigaliūnas, Viktoras; Šlapikas, Kęstutis; Mikolajūnas, Marius; Tamulevičius, Sigitas. Preparation and simulation of micro-solid oxide fuel cell // Advanced materials and technologies : book of abstracts of the 15-th international conference-school, 27-31 August 2013, Palanga, Lithuania. Kaunas: Technologija. ISSN 1822-7759. 2013, p. 175.
4. Sakaliūnienė, Jolita; Abakevičienė, Brigita; Grigaliūnas, Viktoras; Šlapikas, Kęstutis; Mikolajūnas, Marius; Tamulevičius, Sigitas. Production of positive electrode-electrolyte-negative electrode structure for micro solid oxide fuel cells application // 5th International conference on advanced nanomaterials, 2-4 July 2014, Aveiro, Portugal : abstract book / Center of Mechanical Technology and

28

Automation. Department of Mechanical Engineering. University of Aveiro, Portugal. [S.l.: s.n, 2014]. p. [1].

5. Sakaliūnienė, Jolita; Abakevičienė, Brigita; Šlapikas, Kęstutis; Tamulevičius, Sigitas. Influence of magnetron sputtering deposition conditions and thermal treatment on properties of platinum thin films // E-MRS Spring Meeting 2014, from May 26th to 30th, Lille, France. Strasbourg: European Materials Research Society, 2014. p. C.C/P1.18.

6. Sakaliūnienė, Jolita; Rajackaitė, Erika; Abakevičienė, Brigita; Tamulevičius, Sigitas. Characterization of gadolinia doped ceria electrolyte prepared by co-precipitation synthesis method // Advanced materials and technologies : book of abstracts of the 16-th international conference-school, 27-31 August 2014, Palanga, Lithuania. Kaunas: Technologija. ISSN 1822-7759. 2014, p. 156.

7. Sakaliūnienė, Jolita; Abakevičienė, Brigita; Grigaliūnas, Viktoras; Šlapikas, Kęstutis; Mikolajūnas, Marius; Tamulevičius, Sigitas. Fabrication and characterization of a micro-SOFC membrane structure // Nanotechnology: research and development : conference book. Vilnius: Lithuanian Academy of Sciences, 2014, ISBN 9789955937142. p. 71.

8. Abakevičienė, Brigita; Sakaliūnienė, Jolita; Žarkov, Aleksej; Stanulis, Andrius; Butkutė, Skirmantė; Pilipavičius, Jurgis; Beganskienė, Aldona; Kareiva, Aivaras; Šalkus, Tomas; Kežionis, Algimantas; Orliukas, Antanas Feliksas; Tamulevičius, Sigitas. Deposition of synthesized YSZ and GDC thin films by electron beam evaporation technique // 13th European vacuum conference. 9th lberian vacuum meeting. 7th European topical conference on hard coatings : 8-12 September, 2014, Aveiro, Portugal : book of abstracts. [S.l.: s.n, 2014]. p. 194.

9. Sakaliūnienė, Jolita; Abakevičienė, Brigita; Grigaliūnas, Viktoras; Tamulevičius, Sigitas. Kietojo oksido kuro mikroelemento kūrimas ir tyrimai// 41-oji Lietuvos nacionalinė fizikos konferencija, 2015 m. birželio 17-19 d, Vilnius : programa ir pranešimų tezės / Fizinių ir technologijos mokslų centras, Vilniaus universitetas, Kauno technologijos universitetas, Lietuvos fizikų draugija. Vilnius: Vilniaus universitetas, ISBN 9786099551128. p. 111.

10. Sakaliūnienė, Jolita; Grigaliūnas, Viktoras; Šalkus, Tomas; Abakevičienė, Brigita; Tamulevičius, Sigitas. Geometrical effects of Pt electrode on ionic conductivity of YSZ electrolyte thin films deposited using the electron beam evaporation technique // E-MRS Spring Meeting 2015, from May 11th to 15th, Lille, France. Strasbourg: European Materials Research Society, 2015. p. N.31. [Sc. fields: 08T]. [Contribution: 0,200]

11. Sakaliūnienė, Jolita; Abakevičienė, Brigita; Grigaliūnas, Viktoras; Šalkus, Tomas; Tamulevičius, Sigitas. Geometrical effects of Pt electrode on ionic conductivity of thin films deposited using electron beam evaporation technique// Advanced materials and technologies: book of abstracts of the 17-th international conference-school, 27-31 August 2015, Palanga, Lithuania. Kaunas: Kauno technologijos universitetas. ISSN 1822-7759. 2015, p. 150.

12. Muñoz Fuentes, Miguel Ángel; Sakaliūnienė, Jolita; Abakevičienė, Brigita; del Pilar Yeste Sigüenza, María; Cauqui López, Miguel Ángel; Tamulevičius,

Sigitas. Ce0.13Zr0.75Y0.12O1.94 thin film deposited by e-beam evaporation technique as interlayer between electrode/electrolyte // E-MRS Spring Meeting 2016, from May 2nd to 6th, Lille, France. Strasbourg: European Materials Research Society, 2016. p. D.P2.12.

13. Kazlauskas, Saulius; Šalkus, Tomas; Sakaliūnienė, Jolita; Butkutė, Skirmantė; Maciulevičius, Mindaugas; Abakevičienė, Brigita; Kežionis, Algimantas. YZS thin films deposited by e-beam technique // 12th international symposiun on systems with fast ionic transport (ISSFIT-12), July 3-7, 2016, Kaunas, Lithuania: program and abstracts / Kaunas University of Technology. Kaunas: [s.n.], 2016. p. 130.

14. Abakevičienė, Brigita; Sakaliūnienė, Jolita; Rajackaitė, Erika; Tamulevičius, Sigitas. Synthesis of nanocrystalline gadolinia doped ceria by co-precipitation method // 12th international symposiun on systems with fast ionic transport (ISSFIT-12), July 3-7, 2016, Kaunas, Lithuania : program and abstracts / Kaunas University of Technology. Kaunas: [s.n.], 2016. p. 132.

15. Rajackaitė, Erika; Sakaliūnienė, Jolita; Abakevičienė, Brigita; Muñoz Fuentes, Miguel Ángel; del Pilar Yeste Sigüenza, María; Cauqui López, Miguel Ángel; Tamulevičius, Sigitas. Preparation and characterization of Ce0.13Zr0.75Y0.12O1.94 thin films deposited by electron beam evaporation technique for μ-SOFC // Advanced materials and technologies : book of abstracts of the 18th international conference-school, 27-31 August 2016, Palanga, Lithuania. Kaunas: Kauno technologijos universitetas. ISSN 1822-7759. 2016, p. 146.

16.
1. LITERATURE REVIEW

1.1. Micro-solid oxide fuel cells

The search for new energy production technologies as alternatives to fossil fuel combustion needs to consider renewable sources [3,8,15]. Unlike conventional electric energy generators, fuel cells are electrochemical devices which convert the chemical energy of a fuel directly into electrical energy with an additional amount of valuable heat energy [15]. The essential difference between fuel cells and ordinary batteries is the origin of the power. Depending on the supply of the fuel as H_2 and air (O_2) to the element, the fuel cell will continue to generate power, i.e. the open energy system is created; while batteries can't be replenished, i.e. there is a closed energy system.

There are many types of fuel cells, but generally, they all consist of an anode, a cathode, an electrolyte, interconnect and sealing materials [5,8,15,16,20]. The main difference among the fuel cell types are the nature of the electrolyte. It can be a polymer, a liquid or a ceramic. Depending on the choice of electrolyte, the material requirements, the operating temperature, the fuel and even geometry of the fuel cell differ. If the operating temperature of the fuel cell is over 600°C, the use of hydrocarbon fuels, such as methane or propane that is reformed into hydrogen within the cell during internal gas reforming process, is possible. Furthermore, high operating temperature carries the advantage to reach a better overall efficiency due to transforming the exhausted heat into energy [11]. However, high temperature is a major disadvantage when considering to involve fuel cells to the market (industry). Therefore, researchers devote their considerable efforts to reduce the operating temperatures. Low temperature fuel cells have the advantage of smaller requirements for material properties, such as resistance to corrosion and thermal dilatation [11].

Solid-oxide fuel cells (SOFCs) reveal extremely high net efficiency, approaching 70%, compared to the other type of fuel cells. According to the operating temperature, SOFC can be classified into low temperature (LT), high temperature (HT) and intermediate temperature (IT) SOFCs. This element is composed of three basic active layers: the porous anode (negative electrode) and the porous cathode (positive electrode) which are separated by a dense oxygen-ion conducting electrolyte. This tri-layer structure is referred to as the Positive electrode–Electrolyte–Negative electrode (PEN) element.

Currently, state-of-the-art miniaturized micro-solid oxide fuel cells (μ-SOFCs) are of potential interest due to their unique properties and widest possible application in portable devices. They differ from the conventional SOFCs in size, i.e. the overall size for key components, such as μ-SOFC membrane (three-layered PEN structure) is down to sub-microns. Miniaturization leads to a decrease ohmic losses which are linearly dependent on the thickness of the electrolyte, i.e. the diffusion length of the oxygen ions [13], thereby to enhance the total efficiency.

Fig.1 displays the performance of μ-SOFCs comparing specific energy and energy density with respect to other portable energy-delivering devices, e.g. conventional batteries [5].
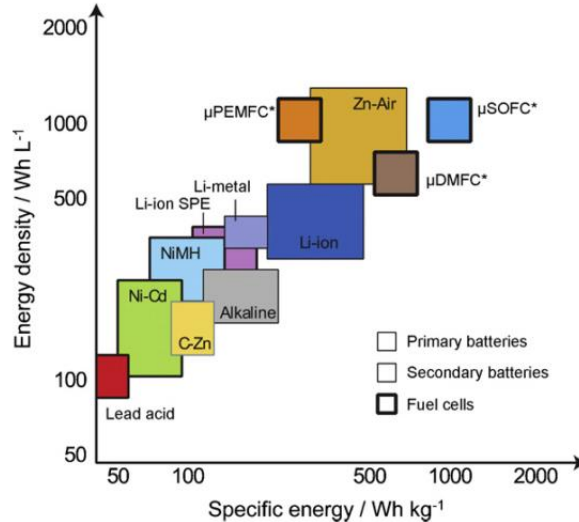
Fig. 1. Specific energy (per mass of device) and energy density (per volume of device) of several portable energy sources [5,11] (Note: μ-PEMFC is micro-proton exchange membrane fuel cells, μ-DMFC is micro-direct methanol fuel cells, NiMH is nickel-metal hydride

Due to the fact that μ-SOFCs are significantly smaller and lighter compared to other portable energy devices, they provide a higher output with the same dimensions as conventional lithium-ion batteries, or reduce the weight and dimension without decreasing the power output [13]. Moreover, μ-SOFCs manufactured using nanoscale thin film electrolytes have shown great promise as portable power sources because of their high performance at drastically reduced operating temperatures, i.e. below 600°C [21], while the conventional SOFCs operate at temperatures around 1000°C [13,22]. This allows diminishing the difficulties associated with material stability.

1.1.1. Principle of work

The operation mechanism of μ-SOFCs is the same as conventional SOFCs. The principal scheme of operation is demonstrated in Fig. 2.

Basically, the PEN element is a membrane which separates two different gas atmospheres [11,23]. The fuel and oxidant gases (or air) flow through the surface of the anode and cathode, respectively. Electrochemical reactions occur in the three-phase-boundary (TPB) region determined at the gas-electrolyte-electrode interface [16,24]. In other words, when hydrogen and oxygen are used as fuel and oxidant, respectively, the chemical reactions in a fuel cell involve the oxidation and reduction of oxygen at the electrodes, i.e. oxidant is reduced at the cathode and fuel is oxidized at the anode side.
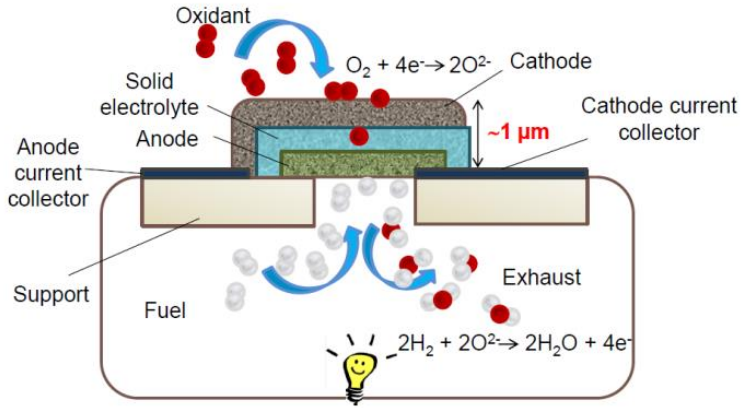
Fig. 2. The principal scheme of μ-SOFC operation

One oxygen molecule in contact with the cathode/electrolyte interface catalytically acquires four electrons from the cathode and splits into two oxygen ions. These ions diffuse into electrolytes and migrate towards the anode due to the oxygen partial pressure difference between the cathode (high p) and anode (low p). O_2 ions contact with the fuel at the anode/electrolyte interface and catalytically react, producing water, carbon dioxide and heat as by-products. Four electrons are released as well, which pass through the anode to the external circuit and back to the cathode providing a source of useful electrical energy in the external circuit. Summarizing, the overall chemical reactions in a fuel cell can be written as follows:

$$O_2 + 4e^- \rightarrow 2O^{2-} \tag{1}$$

$$2H_2 + 2O^{2-} \rightarrow 2H_2O + 4e^-. \tag{2}$$
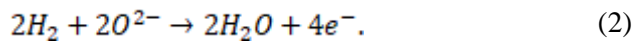
A μ-SOFC element generates the electromotive force (*emf*) or reversible (thermodynamic) voltage, E_r, which can be expressed with the Nernst equation:

$$E_r = \frac{R_u T}{nF} \ln \frac{p_c(O_2)}{p_a(O_2)}; \tag{3}$$

where R_u is the gas constant (8.3145 J/mol·K), T is the temperature (K), n is a number of oxygen moles, F is the Faraday's constant (96485 C·mol^{-1}), $p_c(O_2)$ and $p_a(O_2)$ are partial pressures of oxygen at the cathode and anode electrodes, respectively (Pa).

Hydrogen which is usually obtained from either light hydrocarbons, such as ethane, methane, propane, butane etc., as well as heavier ones, like gasoline, diesel, bio-fuel, etc. can be used to feed a μ-SOFC. However, solid or liquid fossil fuels need to be gasified before they can be used as a fuel [16].

1.1.2. The architecture of μ-SOFC

An electrolyte sandwiched between two porous electrodes serves as the basic block of a fuel cell [9]. Due to some challenges concerning a relatively high operating temperature and complicated packaging, the architecture of μ-SOFCs is still under development. Scientists from Europe, Asia and the USA devote their efforts to create two basic (planar and tubular) designs of such micro-fuel cell, which identically include substrate (e.g. silicon), anode (Ni-YSZ, Pt, etc.), electrolyte (YSZ, GDC, SDC, etc.), cathode (Pt, lanthanum compounds), current collectors (Ag, Pt, etc. pastes) and several other elements [3,15].

Planar and tubular designs may consist of one or several single cells per stacking unit, i.e. on a single tube or in a single film. Moreover, the planar designs can be divided into cells with thick (electrolyte-supported) or thin (anode-supported) membranes as well as into stack systems with metallic or ceramic interconnect material [25]. Although a planar design is more applicable in portable devices, the micro-tubular SOFC are also widely developed [8,26,27].

Generally, the principal structure of any planar design μ-SOFC can be illustrated by the following scheme (see Fig. 3).
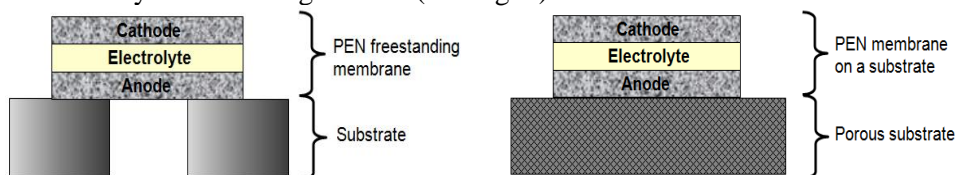
Fig. 3. Possible schematic designs for planar construction of PEN element (here PEN stands for *Positive electrode-Electrolyte-Negative electrode*)

In a case of producing a planar μ-SOFC, the substrate plays an important role. The materials used as substrates in μ-SOFCs should be inert so as to avoid poisoning of thin electrochemically active films deposited on them, moreover, they should also be thermally and mechanically stable within the μ-SOFC manufacturing and operating temperature range [5]. The opportunity to be etched is a basic requirement for all substrates. Very often, the substrates used in the manufacturing process are made up with additional sacrificial layers to enhance the mechanical stability of the cell during the process [28–30]. Suitable geometric shapes inside the structure should allow free electrochemically active cell components for a supply of gas to both an anode and a cathode. There are such substrates available on the market: silicon wafers, glass-ceramics (Foturan) and metallic nickel [1–5].

1.2. Materials and thin films for μ-SOFC

1.2.1. The electrolyte

The performance of SOFC and μ-SOFC strongly depends on the quality of the electrolyte. Generally, electrolyte materials have to satisfy requirements such as high ionic and low electronic conductivity [2,11], chemical stability in both oxidizing and reducing environments, good mechanical properties and long-term stability with respect to dopant segregation [31]; they also have to be chemically and mechanically

34

compatible with other fuel cell components, e.g. electrode materials [32–34]. Good ionic conduction of oxygen ions and a block of conduction of electrons is needed to minimize cell impedance and leakage currents, respectively. Therefore, the control of the concentration and mobility of ionic and electronic charge carriers is critical [32].

Maximum ionic conductivity can be achieved by optimizing the electrolyte composition, microstructure, and processing. As a result, the choice of materials and synthesis routes, also processing stages and conditions are particularly important. Hui et al. [33] summarized the major sources of ionic carriers in oxides and their mobilities, as well as evaluated the correlation of composition, microstructure, processing, and electrical conductivity in polycrystalline materials (Fig. 4).

(a)   (b)
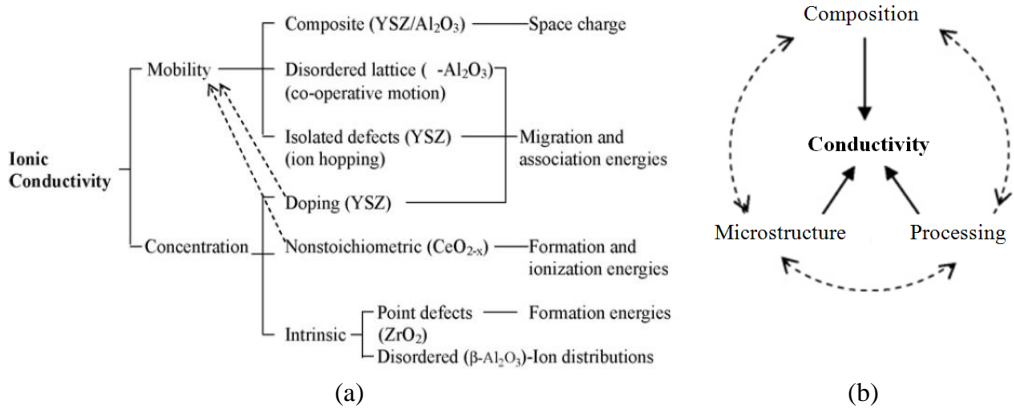
Fig. 4. An example of the major sources of ionic carriers in oxides (a) and the correlation of composition, microstructure, processing, and electrical conductivity in polycrystalline materials under given temperature and surrounding atmosphere (b) [33]

Hence, for a better understanding of a good operation of the μ-SOFC element, ionic conduction mechanisms in the electrolyte, and the properties related to the microstructure have to be emphasized. Generally, electrolyte operation is related to the oxygen-ion transport through the doped crystal lattice [24,35]. This transportation of ions occurs via a lattice-hopping mechanism, where the oxygen ions move into vacancies. Due to the fact that oxygen concentration on the cathode side is higher than on the anode side in μ-SOFC, the gradient that drives the ion transport from cathode toward anode appears [24].

The transport of oxygen ions through the electrolyte can be described with the Wagner theory [34]:

$$j(O_2) = \frac{R_u T}{4^2 F^2 L} \sigma_a \ln\left(\frac{P_{O_2,1}}{P_{O_2,2}}\right);$$ (4)

where $j(O_2)$ is the oxygen flux (mol/m²s), R_u is the gas constant, T is temperature, F is the Faraday constant, L is the thickness of the electrolyte (m) and $P_{O_2,1}$ and $P_{O_2,2}$ are partial oxygen pressures at both sides of an electrolyte, respectively. The ambipolar conductivity then can be expressed as:

$$\sigma_a = \frac{\sigma_i \sigma_{el}}{\sigma_i + \sigma_{el}}; \qquad (5)$$

where σ_i and σ_{el} are ionic and electronic conductivity, respectively. The most important property for SOFCs electrolyte ionic conductivity can be defined as:

$$\sigma_i = n_i q_i \mu_i; \qquad (6)$$

where q_i is the charge, n_i is the number density and μ_i is the mobility of the species. Eq. (6) evidently shows that the ionic conductivity is directly proportional to density, charge and mobility of the species.

The best known and most applicable solid electrolytes for SOFC are ceramics with a fluorite-type structure, such as zirconia- and ceria-based materials, i.e. yttria-stabilized zirconia (YSZ) or gadolinia-doped ceria (GDC) [36].

For more than 90 years, zirconia has been known as a good oxygen conductor at high temperatures (800–1000°C) [16], whereas, the applications of pure zirconia are limited due to the polymorphism [37]. Zirconia has two phase transition points [38] and may exist in three different crystalline phases: monoclinic at room temperature, tetragonal at about 1170°C, and cubic fluorite structure (Fm3m) above 2370°C [34,37,39,40] (see Fig. 4, a). A monoclinic phase is not suitable for high-temperature applications due to the volume expansion during the transformation from a tetragonal to a monoclinic phase [40]. In the case of zirconia-based systems, the cubic polymorph, as noticed, has the highest ionic conductivity and can be stabilized at room temperature by adding such aliovalent oxides as, e.g., Y_2O_3, Sm_2O_3, Sc_2O_3, Ce_2O_3, CaO, MgO, La_2O_3, etc. [32,33,39]. The properties of an electrolyte can be strongly influenced by the concentration and type (ionic radius) of the dopants, which transform the parent lattice and may have the biggest effect on the conductivity. Sc^{3+} is the most effective among all mentioned dopants; however, the initial high conductivity in scandia-stabilized zirconia (ScSZ) is followed by, at first, a rapid and then a gradual drop in conductivity [33].

Zirconia stabilized with 8–9 mol% yttria (YSZ) reveals a cubic phase structure and it is a proven solid electrolyte, demonstrating mainly ionic conductivity over a wide range of oxygen partial pressures [34], whereas doping up to 3 mol% exhibits a monoclinic structure. YSZ in the range of 3–5 mol%, leads to form a tetragonal phase or a mixture of tetragonal and cubic phase [38]. In some cases, tetragonal phase zirconia has also been added to YSZ in order to strengthen the electrolyte structure, therefore the thinner materials can be produced [16].

The ZrO_2-Y_2O_3 phase diagram and formation of YSZ cubic fluorite structure are illustrated in Fig. 5.

Fig. 5 (b) evidently shows that the cubic fluorite structure has a face-centred cubic (FCC) zirconia lattice with a cubic oxygen lattice placed in the FCC lattice. Zr^{4+} cations occupy the tetrahedral sides, while O^{2-} anions the octahedral sites. The residual octahedral sites are occupied by the Zr^{4+} cations [34].

The most commonly used composition for the YSZ electrolyte in SOFCs as well as μ-SOFC is $(Y_2O_3)_{0.08}$-$(ZrO_2)_{0.92}$, because the material possesses an attractive

36

level of oxygen ion conductivity, stability in both oxidizing and reducing environments, and compatibility with the electrode materials [33,34].
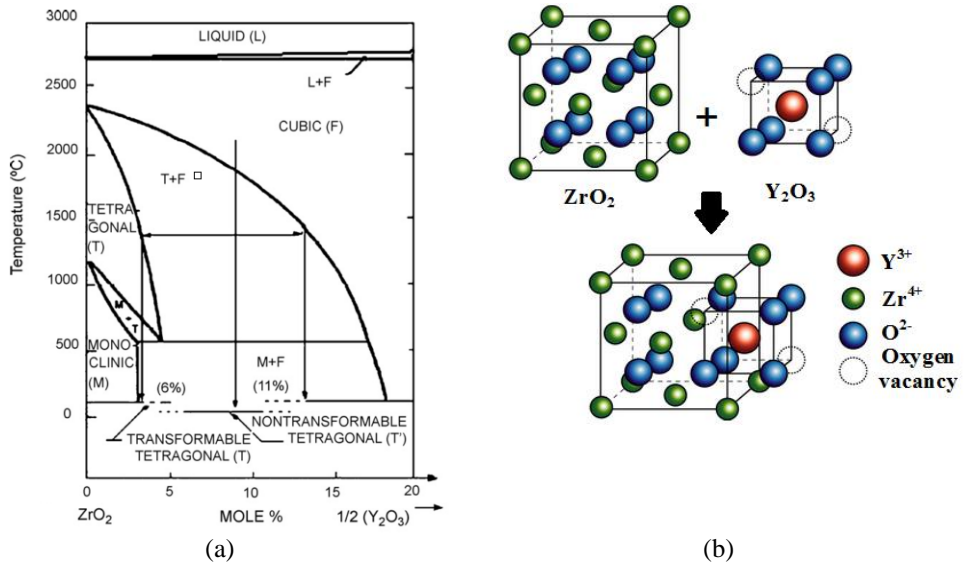
Fig. 5. (a) the phase diagram of yttrium stabilized zirconia [41]; (b) the structure of partially stabilized zirconia lattice [42]

However, at low operation temperatures (lower than 600°C), the ionic conductivity of YSZ is much lower than that of ceria-based electrolytes, such as gadolinia-doped ceria (GDC), samarium-doped ceria (SDC) or bismuth-based oxides and lanthanum gallate-based electrolytes, such as strontium, magnesium-doped lanthanum gallate (LSGM) [31,33,36,43] (see Fig. 6).
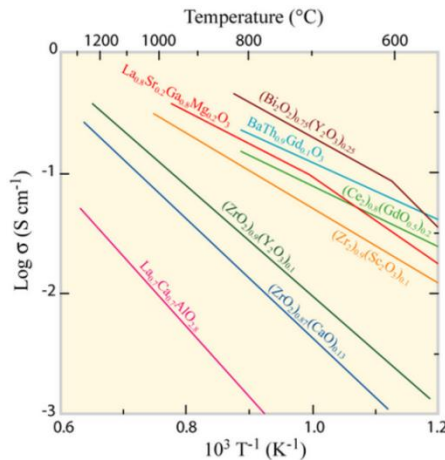
Fig. 6. Conductivity as a function of time of the most commonly used electrolytes for SOFC [43]

Alternatively to YSZ, ceria-based electrolytes, i.e. GDC, are more suitable for low-temperature applications, but it is known that ceria is reducible due to the reduction of Ce^{4+} to a Ce^{3+} state [16]; hence it becomes electronically conductive at higher temperatures. Its reducibility results in the failure of electrolyte material at higher than 750°C temperature [44]. However, regarding the objective to decrease the operating temperature of μ-SOFC by reducing the thickness of the membrane, GDC electrolyte exhibits much better properties than YSZ at the temperatures lower than 600°C. Moreover, due to the superior properties, such as high ionic conductivity and low activation energy [45], ceria-based electrolytes are often used as additives to enhance the performance of SOFC cathodes and anodes [46] or used as an interlayer [12] or bi-layer electrolyte material [16,47].

Generally, in both YSZ and GDC ceramics, a large concentration of oxygen vacancies (defects) are created by the substitution in the lattice of ions of lower valency than the predominant cations [11,48,49]. Moreover, it is generally recognized that the most effective aliovalent ion addition seems to be determined by the relationship between the ionic radii of the additive and the parent lattice [24]. In addition, the cubic fluorite structure is also stabilized [23]. The defect reactions of YSZ and GDC are the following [11]:

$$Y_2O_3 \xrightarrow{ZrO_2} 2Y'_{Zr} + V^{\cdot\cdot}_O + 3O^x_o \tag{7}$$

$$Gd_2O_3 \xrightarrow{CeO_2} 2Gd'_{Ce} + V^{\cdot\cdot}_O + 3O^x_o; \tag{8}$$
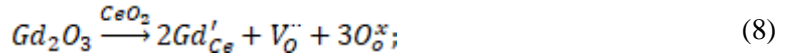
where $V^{\cdot\cdot}_O$ is the oxygen vacancy and point defects, Y'_{Zr} and Gd'_{Ce}. In the GDC structure, identically to YSZ, the Gd^{3+} cations replaced the Ce^{4+} cations located on the plane of the Ce^{4+} lattice thus creating vacancies. In the fluorite unit cell structure, the Ce^{4+} cations occupy the FCC lattice sites, while the anions (O^{2-}) are located at the eight tetrahedral sites [50].

Alternate electrolyte materials mentioned above, e.g. bismuth, lanthanum gallate-based electrolytes, etc., exhibited some shortcomings, such as poor stability at low oxygen partial pressures, reducing their suitability [16], reducibility losing their electrolytic properties; they also tend to become volatile and be chemically reactive with electrode materials [36].

Recently, more efforts have been dedicated to the synthesis of ionic conductive electrolyte materials [6,33,40,51,52]. However, regarding the reliability and well-known characteristics, zirconia- and ceria-based ceramics are still widely used as electrolytes for SOFCs and μ-SOFCs. Many works have studied the ionic conductivity properties of both YSZ and GDC, even investigating the effect of the Y_2O_3 and Gd_2O_3 additions on the ionic conductivity of these materials, respectively [20,40,49,53,54], etc. However, some problems concerning the application of synthesized materials still occur. In order to synthesize electrolyte materials with the required properties, such as microstructure, ionic conductivity, mechanical, chemical and thermal stability for further application in the manufacturing of μ-SOFC, e.g. in

38

the preparation of thin electrolyte films, new or simplified synthesis routes with optimized processing conditions are necessary.

1.2.1.1. The methods of electrolyte ceramics synthesis

The microstructure, mechanical, chemical and electrical properties of electrolyte ceramics can be designed using different chemical routes. A number of advanced synthesis methods have been used for the synthesis of YSZ and GDC ceramics, including solid-state reaction [55], sol-gel process [56], combustion [6], hydrothermal synthesis [57], polyol synthesis [45,58], wet impregnation [15,59], acetic-acrylic method [60] as well as co-precipitation from nitrates [49,54,61,62], oxalates [63,64] and acetates [65,66], spray pyrolysis [9], plasma spray [10], hydrothermal [11], solvothermal [12,60], molecular decomposition [13], microwave synthesis [14], etc.

Due to low manufacturing cost and simplicity, the most common synthesis adopted for the preparation of ceramic compounds is the solid-state reaction [55,67,68]. However, a high calcination temperature, poor compositional homogeneity, small surface area, uncontrollable particle size distribution, along with poor sintering of the products [69] leads to degraded quality of ceramics and electrolyte thin films, even if these ceramics are further used as a target for the fabrication of thin films. The methods mentioned above overcome these disadvantages because of atomic scale homogenous mixing of raw materials, which ensures a lower synthesis temperature and, at the same time, the cost of production. Moreover, the control of some characteristics of ceramics, such as the particle size and distribution, particulate morphology and surface area [69], allows to enhance the quality and durability of thin films.

Compared to the other techniques, the co-precipitation (CP) synthesis method has the advantages of good control of the starting material and the processing parameters, low temperature of the process and high purity and homogeneity of the product due to the possibility to control the starting solution [69]. The control of the initial material synthesis process is essential for the preparation of electrolyte material with the required properties: crystalline structure, crystallite size, distribution of grains [63,64]. This can be achieved by changing the synthesis parameters, such as deposition rate and duration, precipitation material and precipitator concentration, stirring speed, residue solubility, ambient pH, temperature, etc. [69].

Among the tremendous chemical synthesis routes used for the preparation of μ-SOFC materials, an impregnation method, e.g. incipient wetness impregnation (IWI) [70], can be used for both electrolyte and electrode materials preparation, even for straightforward compounds, where the precise stoichiometry is not necessary.

This dissertation focuses on the study of conventional YSZ and GDC electrolyte ceramics with varied concentration of the dopant, i.e. Y_2O_3 and Gd_2O_3, respectively, synthesized via CP synthesis method from acetates. The main goal of the use of CP synthesis was to synthesize electrolyte targets applied in the EB-PVD technique, in order to deposit the electrolyte thin films of the required composition.

The combination of YSZ and ceria (CeO$_2$-YSZ) materials was produced and characterized.

1.2.1.2. Manufacturing of an electrolyte thin film

Another important issue of electrolyte synthesis is the fabrication of electrolyte thin films used in the μ-SOFC [17,28,47]. The reduction of electrolyte thickness by improving the resistance is another important way to lower the operation temperature of μ-SOFC. However, it should be emphasized that the properties of dimensionally reduced systems, such as thin films, are modified due to the fact that they often consist of nano-crystalline grains and exhibit high density of grain boundaries thus revealing different behaviour of conductivity and thermal stability compared to micro-crystalline solids [4,38,39,71–75], etc. Thus, studies dealing with grain and grain boundary effects are important [76].

For the preparation of thin films, both chemical (CVD) and physical vapour deposition (PVD) techniques can be applied. PVD is more favourable then CVD due to the lower process risk and cheaper material [77]. While, the deposition of thin electrolyte films using the electrophoretic technique has received potential interest in recent years [78]. Many studies have been done, for example [13,17,39,79–83], employing vacuum deposition techniques for the production of electrolyte thin films. PVD techniques have some challenges, e.g., relatively high cost and complexity, however by using them, very thin and fully dense films can be produced on either porous or dense substrates [5,83], which may enable higher power densities to be achieved. PVD processes can be used to deposit films of elements and alloys as well as compounds using reactive deposition processes [84]. Moreover, films can be formed at temperatures much lower than it is required in traditional ceramics processing [80]. Unfortunately, the film's stoichiometry is found to be difficult to control because of the deposition of composite material [47,85].

For optimum performance of μ-SOFC, the electrolyte has to be of a dense structure avoiding gas permeation from one side to the other. Moreover, films should also be uniformly thin to minimize ohmic losses, and exhibit high oxygen ion conductivity [16]. Another issue in terms of nano-crystalline thin film are stresses within the films [4] caused by thermal expansion mismatch between the substrate and the film; or phase-transformation-induced stresses [86]. These stresses may cause mechanical and thermal stability failures during the operation of μ-SOFC. Therefore, in order to ensure satisfactory performance of the cell, the choice of the deposition technique and experimental conditions, initial materials and substrate has to be considered.

The most common techniques for the formation of μ-SOFC electrolyte are magnetron sputtering, atomic layer deposition (ALD), and pulsed laser deposition (PLD), while e-beam evaporation (EB-PVD) of complex materials is thought to be complicated and, therefore, is rarely used [47]. However, compared to the other PVD methods, the EB-PVD technique has the advantages of high deposition rate and large deposition area [83][87]. Using this method, any type of refractory

materials, such as most ceramics, glasses, carbon, and refractory metals can be evaporated [84].

Rupp et al. [88] demonstrated that grain size, thereby grain boundaries effect the microstructure and electrical properties of GDC thin films formed by using the spray pyrolysis and PLD technique. It was shown that the activation energies of ionic conductivity decrease with decreasing grain size from the micro- to the nano-crystalline scale, independently of the chosen preparation method. Infortuna et al. [89] presented the variation of YSZ and GDC thin film microstructure and growth behaviour with respect to pressure and temperature used in the PLD process (see Fig. 7.). The trends of pressure and temperature effects on the thin film's microstructure were obtained as well by using other PVD techniques.
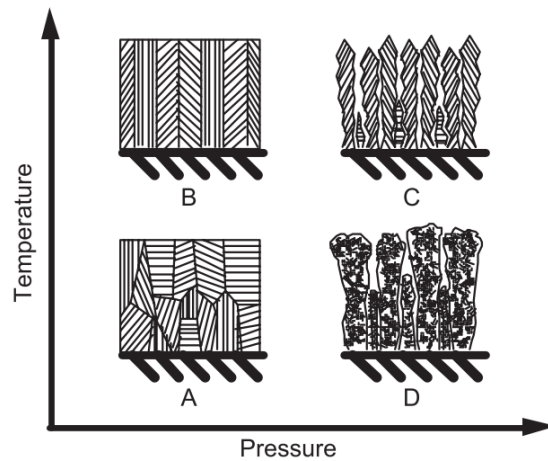
Fig. 7. The influence of pressure and temperature on the YSZ and GDC thin film's microstructures [89]

Generally, it is evident that thin films formed at low pressure exhibit disordered but coherent grains at low temperatures (Fig. 7, A), and strongly ordered grains at higher temperatures (Fig. 7, B). Maintaining the corresponding conditions, thin films formed by PLD technique exhibit microstructures similar to those obtained by sputtering. At high pressure, stable crystalline clusters nucleate in the supersaturated plasma of the plume. They collect on the substrate in a loose structure and pores form because of the shadowing effect at low temperature (Fig. 7, D). Both high pressure and temperature causes the "dissolution" of the clusters in columnar grains including the entire thickness of the film (Fig. 7, C). The shadowing effect prevents full densification of the microstructures and thus voids remain between grains [89]. In conclusion, the management of the deposition conditions leads to an improvement of quality, properties and microstructure of thin film.

There are only a few studies where the EB-PVD technique is applied for the formation of electrolyte thin films. Laukaitis et al. [80,81,87,90] has reported studies representing the influence of the EB-PVD operating technical parameters, e.g. deposition rate, e-beam gun power, substrate heating temperature, etc. on the GDC and YSZ electrolyte thin film growth behaviour, microstructure and crystallite sizes,

and assessed the impact of the substrate on these properties. However, the authors formed relatively thick films, i.e. thicknesses varied in the range of 1.5–5 μm. Huang et al. [79] presented the effects of different substrate heating temperatures during the EB-PVD processing on the crystalline structure, the lattice constant, the grain growth, and the strain of YSZ thin films (thickness of about 600 nm). The authors observed that the lowest strain of the YSZ film was obtained when the heating of the substrates reached 200°C. In all aforementioned studies, the target material used in the EB-PVD was prepared from commercially available ceramic powder. While, Hong et al. [83] presented the formation of GDC thin films evaporated from the target synthesized by ammonium carbonate CP method.

From another point of view, there is a limited number of studies concerning the evaluation of stoichiometry deviations in the deposited thin films with respect to the initial target (composite oxide material) [91,92]. However, it is an essential and related to effective operation of the electrolyte, as well as performance of μ-SOFC. Saporiti et al. [91] showed that PLD technique is well suited to the formation of well-adhered to the substrate electrolyte thin films due to the possibility to produce thin films with the same stoichiometry as the target was. However, it is difficult to control the surface morphology as well as porosity of the film. Uhlenbruck, et al. [92] employed magnetron sputtering and EB-PVD technique for the fabrication of GDC electrolyte thin film. The authors summarized that the measured ratio of Ce and Gd of the GDC thin film corresponds almost exactly to the theoretical value of the target composition despite the deposition temperatures. While Sanghoon Ji et al. [93] showed that the chemical composition of deposited thin film depends on the target material and substrate temperature during the deposition process. In addition, Rachmat Adhi Wibowo et al. [85] explained the deviation of chemical composition due to the different sputtering yield or re-evaporation process during the deposition. However, the lack of stoichiometry in electrolyte thin films produced by EB-PVD technique has not been sufficiently studied. Hong et al. [83] described the stoichiometry in evaporated thin films (thicknesses varied as follows: 1, 3 and 5 μm). According to the energy dispersive X-ray (EDX) analysis of the films, the chemical composition of GDC film slightly differs from GDC bulk powder, i.e. GDC thin film appeared to have more Gd content and less Ce content than the evaporating GDC powder. The observed deviations from the bulk material composition show different evaporation behaviour of each component. The authors concluded that the Gd content in the evaporating GDC powder should be controlled to obtain a thin film of the required composition. Paek et al. [17] presented the deviations in stoichiometry of thin films deposited by different PVD techniques, i.e. ALD, PLD and sputtering. While Sanghoon Ji et al. [93] presented the dependence of chemical composition of thin films on the target material and substrate temperature.

According to the theoretical framework [94–96], there are many factors which may influence the deviation of chemical composition in the condensed thin films compared with the target material. The evaporation of multinary compounds which may create solid solution is complex, particularly if the elements (generally, metals) of the compound are very close to each other on the periodic table. The complexity

of the evaporation process occurs due to a different evaporation temperature and evaporation rate of the individual component at the same process temperature.

The evaporation rate is also directly related to the furnace pressure. The pressure exerted by the vapour of a liquid in isolated space is called its vapour pressure and depends on the temperature. The vapour pressure differs for all substances at any given temperature, but each substance has a specific vapour pressure for each given temperature [95]. Metals evaporate as a function of temperature and vacuum level. High vacuum conditions lead to greater evaporation rate. Eq. (9) can be used to determine the evaporation rate [95]:

$$F_{max} = 0.058 p_v \sqrt{\frac{M}{T}} \tag{9}$$

where evaporation rate, F_{max}; vapour pressure, p_v; temperature, T; molecular weight, M. In a case where the element is part of a metal alloy system, the vapour pressure relationship will change, i.e. the total vapour pressure of the alloy is the sum of the vapour pressures of each constituent times the percentage in the alloy [95].

Generally, the evaporation rate of the compound can be expressed as follows [94]:

$$F = \sum_i F_i; \tag{10}$$

where the evaporation rate of a separate component, F_i, which can be described as:

$$F_i = \frac{\alpha f_i C_i p_{si}}{\sqrt{2\pi m k T}}; \tag{11}$$

where α is the evaporation coefficient; p_{si} is the saturated vapour pressure of the i component; m is the mass of molecule; k is Boltzmann's constant; T is the temperature; C_i is the relative concentration of the i component; f_i is the activity coefficient of the i component. The later coefficient is equal to 1 only for the ideal substances (Raoult's law). However, many compounds have $f_i \neq 1$ which also depends on the concentration of an indivudual component. Due to this reason, different elements evaporate at different rates during the process and the chemical composition of the condensed material may vary compared to the target material. After equilibration, the difference between the composition of vapour and condensed phases can be expressed as:

$$\frac{C_A^S}{C_B^S} = \frac{f_A}{f_B} \frac{p_{As}}{p_{Bs}} \left(\frac{M_B}{M_A}\right)^{\frac{1}{2}} \frac{C_A^C}{C_B^C} = K \frac{C_A^C}{C_B^C}; \tag{12}$$

where the concentration of elements A and B in the vapour phase, C_A^S and C_B^S, respectively; the concentration of elements A and B in the condensed phase, C_A^C and C_B^C, respectively. Then, value of K can be expressed as:

$$K = \frac{f_A}{f_B} \frac{p_{As}}{p_{Bs}} \left(\frac{M_B}{M_A}\right)^{\frac{1}{2}}; \tag{13}$$

where the saturated vapour pressure of elements A and B at the evaporation temperature are p_{As} and p_{Bs}, respectively; M_A and M_B are molecular weight of elements A and B, respectively. Parameter K is a factor which displays the composition difference between the vapour and condensed phases. Therefore, the composition of thin film deposited using the evaporation technique may vary with respect to the target material. Moreover, this difference depends on the evaporation time. Firstly, more volatile elements are evaporated; secondly the evaporation rate of less volatile elements is increased as the amount of evaporated material increases. This process leads to the surface elemental composition changes in the condensed film. Equal volatility of elements is a necessary but not sufficient condition to obtain the same chemical composition of the films compared to the bulk material. In order to combine the initial stoichiometry compound AB, adsorption of the two components, A and B, in correct proportions on the substrate is required. The surface elemental composition remains the same as the bulk one and depends on the content of evaporated material (target). This dependence can be described as:

$$\frac{N_A}{N_A^0}\left(\frac{1-C_A^0}{1-C_A}\right)^K = \left(\frac{N}{N^0}\right)^{K-1} \text{ and } \frac{1-C_B}{1-C_B^0}\left(\frac{C_B^0}{C_B}\right)^K = \left(\frac{N}{N^0}\right)^{K-1}; \qquad (14)$$

where C_A^0 and C_B^0 are the initial concentrations of elements A and B in the target material, respectively; $N^0 = N_A^0 + N_B^0$ – the initial number of molecules in the evaporated compound.

Furthermore, the composition of the condensed film depends on the element diffusion process from the deeper layers to the surface. Diffusion can be activated using additional substrate heating. Therefore, a higher substrate temperature (> 600°C for ceramics) during the deposition process is preferred and leads to the formation of required elemental composition of thin films.

Overall, the evaporation process is complex and depends on many factors, therefore the formation of homogenous thin films with the required composition often is complicated and possible only under certain conditions or by adjusting a specific composition of the source material.

1.2.2. The electrodes: an anode and a cathode

Electrodes are critical components in SOFCs (as well as μ-SOFC) due to the obligation to provide the interface between the chemical energy associated with fuel oxidation and electrical power [31]. During the operation conditions, electrons are produced at the most electrically negative anode, flow through the load and back to the fuel-cell at the most electrically positive cathode. Hereby, the electrochemical oxidation of the fuel supplies electrical power to the external load [24].

Generally, both an anode and a cathode must have high (electro)catalytic activity and electronic conductivity to minimize the effective resistance and be permeable to gas (oxygen and fuel) during the operation of μ-SOFC [11]. In addition, sufficient porosity of the anode in the range of 40÷60% for H_2 ions exchange at gas-electrolyte-anode interface and formed water to get away has to be ensured.

Typically, the anode is very catalytically active towards the hydrogen and hydrocarbon oxidation reaction, but at the same time suffers stability issues at relatively high temperature and reducing environments [97]. However, the anode has to maintain zero-chemical reactivity with the substrate or other membrane thin films which contact it [2,5].

During the µ-SOFC operation, oxygen ions from the electrolyte membrane enter the ion-conducting phase. Upon charge-transfer reaction at the three-phase regions, called *triple-phase boundaries* (TPB), formed by the interface of electron conducting electrode, ion conducting electrolyte, and gas phases [24,69], negative charge is then transferred from the ion into the electrode phase [10].

Cathodes have to be manufactured as porous structures for a rapid mass transport of reactant and product gases [16,24]. Also, they have to present high electronic and ionic conductivity, adequate thermal and chemical stability at high temperature in air and good compatibility with the electrolyte. Moreover, it should exhibit sufficient porosity to facilitate the transport of molecular oxygen from the gas phase to the air electrode/electrolyte interface [16].

Tsipis et al. [98] and Chandran et al. [16] published excellent reviews on electrode/electrolyte materials used in SOFCs (µ-SOFC). The authors summarized that metals such as nickel, platinum, ruthenium, palladium or the ceramic–metal composites (cermets), usually containing YSZ and Ni, where the metallic phase acts as electronic conductor and catalyst, are the most common anode materials up to now. The fuel cell can also be supported by a metallic substrate, e.g. by a nickel porous plate [11]. The most frequently used cathode or air electrode materials are platinum or compounds such as lanthanum strontium cobalt oxide (LSC), lanthanum strontium cobalt iron oxide (LSCF), barium strontium cobalt iron oxide (BSCF), etc. [4,24,99,100].

In all the cases, the effect of the microstructure and the composition of the anode and cathode are very important for the efficiency of the µ-SOFC. Fleig et al. [18] emphasized the importance of the electrode microstructure for using electrodes with nanometer-sized grains or dense electrodes with a mixed ionic–electronic conductor [47]. While Rey-Mermet [11] highlighted that for thin films (thicknesses lower than 100 µm), the electrolyte conductivity deviates from the linear law, i.e. 1/thickness, and becomes dependent on the electrode microstructure dimensions (grain size and space between them).

1.2.2.1. Manufacturing of the electrode thin films

The anode and cathode thin films are also used in the manufacturing of state-of-the-art µ-SOFC [14]. Identically to the electrolyte thin film preparation, PVD techniques for the fabrication of electrode thin films are the most popular, e.g. sol-gel, spray pyrolysis, PLD, magnetron sputtering, etc. [101].

The thermal and mechanical stability, chemical compatibility during preparation and operation, reliability and electrochemical performance of the microfabricated µ-SOFC membranes are scale-dependent properties, therefore, the structural design and behaviour of all components, especially at high temperatures, of the electrochemically active membrane must be configured carefully [5,18,102].

Platinum with low electrical resistivity, stable structure at the substrate interface, catalytic behaviour and appropriate porosity is one of the most widely used catalysts in the fuel cells. Recently, researchers have shown an increased interest in sputtered platinum, as a potential electrode for μ-SOFCs [2]. Porous Pt films were used as an anode and a cathode in miniaturized cells by Rey-Mermet [11], Kerman et al. [10], Tsuchiya et al. [103], An et al. [104], Huang et al. [19], etc.

Various methods of deposition for the formation of platinum thin films have been actively investigated in terms of low loading control via vacuum technology. Magnetron sputtering is one of the physical vapour deposition methods distinguished by precise control of Pt loading, extremely uniform dispersion and high through-put [47,105].

Several reports [105–108] proved that argon pressure during the magnetron sputtering process and further thermal treatment can influence the surface morphology and electrical properties of platinum films. For example, Ikwhang Chang et al. [106] reported the electrochemical surface area dependency on the thicknesses and porosity of Pt thin film anodes. The porosity and roughness of Pt thin film were controlled by Ar pressure during the sputter deposition process. The surface roughness of sputtered Pt deposited at various pressures showed two separate areas: dense (0.67–5.33 Pa) and porous (8–16 Pa) films. The authors argued that relatively porous Pt films (sputtered at 8–16 Pa) showed significantly larger exchange current densities, by 4–5 orders of magnitude relative to the dense film.

One of the main disadvantages of this method is poor adhesion of the layers on typical dielectrics, such as silicon dioxide and silicon nitride, which are most frequently used in μ-SOFC microfabrication processes as a sacrificial layer. Pt easily reacts with silicon and forms platinum silicide at relatively low temperatures (200 – 450°C) [109]. Therefore, intermediate titanium (Ti), tantalum (Ta), zirconium (Zr) or chromium (Cr) protective layers between the Pt film and the substrate are often used to improve adhesion and to prevent the formation of silicides [110].

The determination and control of residual stress in the Pt thin films is important for producing a mechanically stable μ-SOFC (PEN) structure. Stress is mostly a result of the manufacturing processes [15]. Moreover, the stress could be caused by the localized yielding of the material or by certain surface treatments (like annealing at high temperatures) [111]. Despite their importance, residual stresses are difficult to foresee. There are only a few studies on stress evaluation of Pt thin films [110,112–114].

On the other hand, with the development and miniaturization of components of μ-SOFC devices, the state of surfaces at operating conditions of these components becomes more and more important.

In this thesis, electrical properties, morphology and residual stress of Pt thin films versus technological conditions with the aim to contribute to the understanding of the role of thermal treatment of Pt electrodes deposited on typical surfaces used in the technology of μ-SOFC (SiO$_2$, Ti/SiO$_2$, yttria-stabilized zirconia) were investigated. Microstructure, roughness parameters, resistivity, porosity and microstrain of platinum electrodes were evaluated.

1.3. Technological routes for μ-SOFC manufacturing

The design of miniaturized solid oxide fuel cells (μ-SOFCs) is compatible with conventional semiconductor fabrication technologies [18]. However, from the theoretical point of view, they differ in electrode and electrolyte geometries. The development of μ-SOFC manufacturing routes by applying cutting-edge technologies allows to optimize the performance of the cell, thus reducing the cost. The majority of μ-SOFC designs were generated and fabricated in Stanford and Cambridge Universities (USA), ETH Zurich (Switzerland), EPF Lausanne (Switzerland) and some High education Korean institutions [5]. However, without a doubt, Swiss scientists as Evans, Bieberle-Hütter, Beckel, Rupp, Gauckler etc. contributed most to the development of μ-SOFC [2,4,47]. Their scientific achievements are fundamental for other authors. This subchapter overviews the developed structures and their characteristics.

A review article [5] describes the achievements of different scientific groups in developing the μ-SOFCs. It was shown that mechanical and thermal stability as well as the reliability of μ-SOFC is largely determined by the size and geometry of the membrane and the material properties, so it is very important to choose the right device technology route, geometry and materials for the fabrication of electrode and electrolyte thin films as well as an appropriate sacrificial layer.

The thickness of the electrode membrane in different works varies from parts up to a few microns, when the area of membrane varies from a few square microns up to twenty millimetres [18,115]. For example, Shim et al. [116] successfully applied silicon bulk micromachining to fabricate a thin film membrane structure (thickness of membrane 220 nm, active area size varied from 20 to 100 square microns). 300 nm thick thin film membrane (active area size varied from 50 to 240 square microns) was fabricated using sputtering, lithography, and deep etching by Huang et al. [19].

In other work, a corrugated μ-SOFC membrane was fabricated on the pre-patterned silicon substrate in order to increase the active surface area and mechanical strength of membrane as well as the resistance to thermal stress of the layered membrane structure [117]. A two-step fabrication technique of SiO_2/Si membrane combining deep wet silicon etching and SF_6/O_2 reactive ion etching was demonstrated in [118]. Here, the simulation revealed that an increase in size of the membrane contributes to the rise of deformations as well as stresses at the membrane edges and corners.

Garbayo et al. [119] describes the fabrication of composite SiO_2/Si_3N_4 membrane obtained using wet silicon etching in KOH solution following removal of SiO_2 layer in order to obtain Si_3N_4 membrane (thickness of Si_3N_4 membrane 300 nm, active area size varied from 50 to 820 square micrometres). A. Johnson [120] also utilizes Si_3N_4 insulating layer to deposit 75 nm–150 nm thick yttria-stabilized zirconia (YSZ) electrolyte, a 40 nm–80 nm porous Pt anode, and a 130 nm porous Pt cathode. Recently, it was shown that a Pt anode can be successfully replaced [121] by a nano-porous palladium (Pd) film or ruthenium and gadolinia-doped ceria composite nano-crystalline thin film [122]. The thickness effects of yttria-doped ceria interlayers on solid oxide fuel cells [123] and mechanical and thermal stability

of free standing membranes was studied in [124,125]. Modelling shows [125] that the edge-clamped thin film membrane presents multi-stage wrinkles (the largest ones are in the centre and the smaller ones are near the clamped boundary) and the largest tensile stress is close to the clamped boundary.

However, the most recent development in manufacturing of μ-SOFC was carried out by Kim et al. [126]. The authors reported a new strategy for enhanced thermal cycling ability (robustness) in μ-SOFC manufactured by employing oxide-based thin-film electrode and porous stainless steel substrate. Also, simpler fabrication processes, such as tape casting and lamination processes were used to avoid conventional procedures as lithography, etching or templating. The fabrication process is demonstrated in Fig. 8.
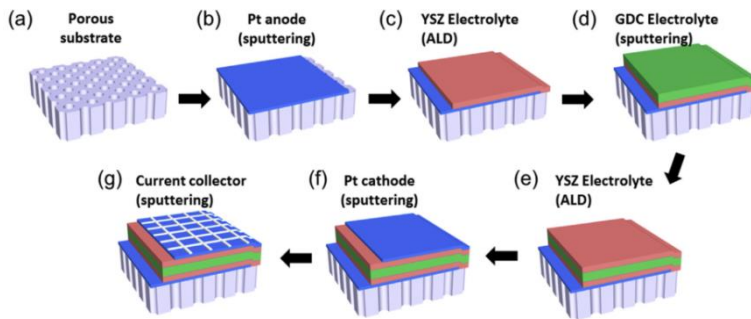
Fig. 8. Diagrams for the fabrication of thin-film SOFC composed of (a) anodic aluminium oxide substrate (with 80 nm pores and a thickness of 100 μm), (b) Pt anode, (c)-(e) multilayer electrolyte (YSZ-GDC-YSZ), (f) Pt cathode, and (g) current collector [126]

In this recent work, a multilayer electrolyte was composed of 100-nm-thick YSZ thin film deposited by atomic layer deposition (acts to clog any possible nano-pinholes within the porous Pt anode), 300-nm-thick sputtered GDC thin film and another 100-nm-thick YSZ thin film formed on the top surface of GDC. The manufacturing process of μ-SOFC structure combines 6 steps, including different thin film deposition techniques, meanwhile, in most cases, other technological routes typically involve 8–10 manufacturing steps [4]. The author also overviewed the achievements obtained by other authors. The summarized results are displayed in Table 1 and Fig. 9.
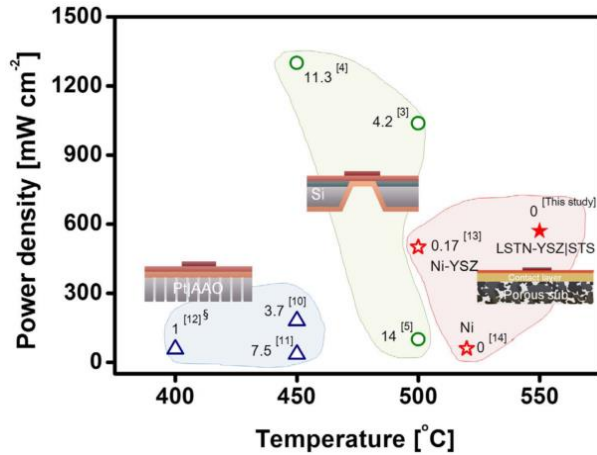
Fig. 9. The situated dependence of power density of μ-SOFC manufactured using different geometries on the operation temperature [126]

Regarding the overviewed literature (see Fig. 9), it is evident that the highest power density in the range of 600–900 [mW/cm^2] can be obtained only from the μ-SOFCs membrane structure, manufactured using bulk micromachining of silicon techniques. Moreover, the operation temperature is lower when compared to the membrane structure obtained by Kim et al. [126].

Table 1. The developers of μ-SOFC in planar cell design and the corresponding manufacturing details and properties [126]. Note: (L&E) lithography and etching, (CM) compression-molded, (sP) screen printing, (SP) sputtering, (PLD) pulsed laser deposition, (ALD) atomic layer deposition

Group	Substrate (process/thickness)	Anode (process/thickness)	Electrolyte (process/thickness)	Cathode (process/thickness)	Active area [mm^2]	Open-circuit voltage [V]	Power density [mWcm^{-2}]	T [°C]	Degradation rate
Kerman et al. [10] (Harvard Univ.)	Si wafer (L&E/-)	Pt (SP/80 nm)	YSZ (SP/100 nm)	Pt (SP/80 nm)	0.03	0.97	037	500	50%/12 h (at 400 °C)
Tsuchiya et al. [103]	Si wafer (L&E/-)	Pt (SP/30 nm)	YSZ (SP/54 nm)	LSCF (SP/47 nm)	25 (Ni grid)	0.75	55	510	14%/1h (at 500 °C)
An et al. [104] (Stanford Univ.)	Si wafer (L&E/-)	Pt (SP/80 nm)	YSZ/YDC (ALD/60 nm)	Pt (SP/80 nm)	0.002	1.05	300	450	34%/3h (at 450 °C)
Ha et al. [127] (Seoul Univ.)	AAO (-/100 μm)	Pt (SP/≤3 80 nm)	YSZ (ALD;SP/3 90 nm)	Pt (SP/200 nm)	4	1.1	80	450	11%/3h (at 450 °C)
Ji et al. [128]	AAO (-/100 μm)	Pt (SP/25	YSZ/GDC (ALD,SP/4	Pt (SP/200	1	1.07	5	450	30%/4h (at

		0 nm)	60 nm)	nm)					450 °C)
Kwon et al. [129] (K.I.S.T.)	AAO (-/600 nm)	Pt (SP/80 nm)	YSZ/Al₂O₃/YSZ (ALD,PLD /900 nm)	Pt (SP/80 nm)	0.01	1.0	0 (at 0.8 V)	400	17%/17 h (at 400 °C)
Noh et al. [130]	Ni-YSZ (CM;sP/1 mm)	Ni-YSZ (PLD/2-3 μm)	YSZ/GDC (PLD/600 nm)	LSC-GDC/LSC (PLD/5 μm)	100	1.1	88	500	17%/100h (at 600 °C)
Chen et al. [72] (Houston Univ.)	Ni foil (L$E/6 μm)	Ni-YSZ (PLD/6 μm)	YSZ (PLD/2 μm)	LSC (PLD/6 μm)	-	0.8	10	570	0%/6h (at 520 °C)
Huang et al. [19]	Si wafer (L&E/-)	Pt (SP/80 nm)	YSZ (SP/50 nm)	Pt (SP/80 nm)	0.05	0.8	30	350	-
Kim et al. [126]	LSTN-YSZ(40 μm)/STS 434 L 380 μm (TC)	Ni-YSZ (PLD/6 00 nm)	YSZ (PLD/2 μm)	LSC (PLD/7 00 nm)	3	1.0	60	550	0%/13h (at 550 °C)

Another important literary aspect is the evaluation of electrolyte/electrode interfaces in the three-layered membrane structure. Kundracik et al. [131] showed a remarkable influence of Pt-YSZ interfaces on the value of ohmic resistance of YSZ thin films (thickness varied in the range of 240–330 nm). Fig. 10 illustrates YSZ thin film at an incomplete electrical contact with respect to thickness.

(a)   (b)
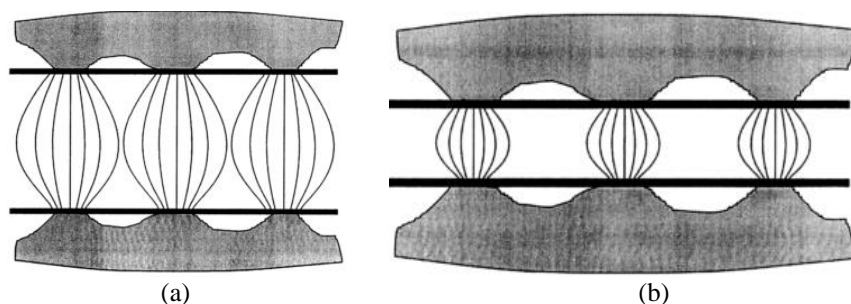
Fig. 10. The schematic displacement of an effective current density in YSZ at an incomplete electrical contact: (a) current field is only lightly deformed at the thicker film and (b) current field is discontinuous in the case of the low thickness of the film [131]

The manufactured three-layered PEN structure can be schematically represented as demonstrated in Fig. 10 as well. It is evident that the enhanced operation and performance of the membrane can be obtained by optimizing the interface contact between the negative electrode, electrolyte and the positive electrode. Therefore, the surface morphology of thin films as well as the behaviour at operating temperatures of the PEN structure has to be evaluated.

According to the overviewed literature and μ-SOFC (PEN) operation aspects, the manufacturing route of PEN three-layered membrane structure was designed and implemented in this dissertation.

2. Experimental techniques and methods

The following Chapter gives the description and experimental details of the technological and analytical methods and equipment; it also describes thin film deposition procedures used for the electrolyte and anode/cathode electrode formation, followed by the steps necessary to fabricate a miniaturized μ-SOFC. The electrolyte and anode/cathode electrodes were deposited by using the electron beam evaporation technique and magnetron sputtering, respectively.

Techniques/methods which required special attention are introduced before the corresponding experimental details.

2.1. Technological methods and equipment

2.1.1. Materials

Deionised water (H_2O), 99.8% acetone (C_3H_6O) (Reachem Slovakia s.r.o.), 25 % ammonium hydroxide (NH_4OH) (Reachem Slovakia s.r.o.), 30 % hydrogen peroxide (H_2O_2) (Reachem Slovakia s.r.o.), argon gas (Aga Sia, purity 99.996%), oxygen gas (Aga Sia, 99.996%), ≥99% *N,N*-Dimethylformamide (Sigma-Aldrich), nitrogen (N_2) gas (Aga Sia, 96%) were used to prepare the surface of substrates.

Al etchant (Al-12S, Sunchem AB) was used to remove the auxiliary Al layer after the Bosch process.

In order to determine the dependence of thin film thickness on the process time of the e-beam evaporation (thickness vs time) and chemical composition of thin films, commercial yttria-stabilized zirconia powder (denoted as 8YSZ-45, Tosoh, ball-shaped granules with 45 μm in diameter), containing 8 mol% of Y_2O_3 and gadolinium-doped ceria powder (denoted as GDC20-N, Fuel cell materials, with a crystallite sizes of 5–10 nm), containing 20 mol% of $GdO_{1.5}$ ceramic powder were used as targets. The information regarding the commercial and synthesized ceramics by CP synthesis and incipient wetness impregnation (see Subchapters 2.1.1.1. and 2.1.1.2.) used in this work is summarized in Table 3.

Table 2. The summary of ceramic powder used in this research

Notation	Content of impurities	The molar concentration of impurities	Base	Chemical formula	Origin of ceramics
8YSZ-45	$x_Y = 0.15$	8 mol% of Y_2O_3	zirconia	$(Y_2O_3)_{0.08}(ZrO_2)_{0.92}$	comm.*
GDC20-N	$x_{Gd} = 0.20$	20 mol% $GdO_{1.5}$	ceria	$Gd_{0.2}Ce_{0.8}O_{2-\delta}$	comm.*
5-YSZ	$x_Y = 0.10$	5 mol% of Y_2O_3	zirconia	$Y_{0.10}Zr_{0.90}O_{2-\delta}$	CP synth.
8-YSZ	$x_Y = 0.15$	8 mol% of Y_2O_3	zirconia	$Y_{0.15}Zr_{0.85}O_{2-\delta}$	CP synth.
10-YSZ	$x_Y = 0.18$	10 mol% of Y_2O_3	zirconia	$Y_{0.18}Zr_{0.82}O_{2-\delta}$	CP synth.
10-GDC	$x_{Gd} = 0.18$	10 mol% of Gd_2O_3	ceria	$Gd_{0.18}Ce_{0.82}O_{2-\delta}$	CP synth.
12-GDC	$x_{Gd} = 0.21$	12 mol% of Gd_2O_3	ceria	$Gd_{0.21}Ce_{0.79}O_{2-\delta}$	CP synth.
15-GDC	$x_{Gd} = 0.26$	15 mol% of Gd_2O_3	ceria	$Gd_{0.26}Ce_{0.74}O_{2-\delta}$	CP synth.
18-GDC	$x_{Gd} = 0.31$	18 mol% of Gd_2O_3	ceria	$Gd_{0.31}Ce_{0.69}O_{2-\delta}$	CP synth.
20-GDC	$x_{Gd} = 0.33$	20 mol% of Gd_2O_3	ceria	$Gd_{0.33}Ce_{0.67}O_{2-\delta}$	CP synth.
CeO_2-YSZ	-	15 mol% of CeO_2; 8 mol% of Y_2O_3	zirconia	$Ce_{0.13}Y_{0.12}Zr_{0.75}O_{2-\delta}$	IWI synth.

* comm. is commercial powder.

2.1.1.1. Co-precipitation synthesis method and experimental details

For the preparation of various molar concentration of yttria-stabilized zirconia (YSZ) and gadolinia-doped ceria (GDC) ceramic powder, the sol-gel synthesis technique, so-called, co-precipitation (CP) method was used. Zirconium (IV) acetate hydroxide ($Zr(CH_3COO)_x \cdot (OH)_y$, Sigma-Aldrich, 99.9%), yttrium (III) acetate tetrahydrate ($Y(CH_3COO)_3 \cdot 4H_2O$, Alfa Aesar, 99.5%), as well as cerium (III) acetate hydrate ($Ce(CH_3COO)_3 \cdot xH_2O$, Sigma-Aldrich, 99.99%) and gadolinium (III) acetate hydrate ($Gd(CH_3COO)_3 \cdot xH_2O$, Alfa Aesar, 99.9%), were used as initial materials for the synthesis of YSZ and GDC electrolyte, respectively. Oxalic acid dihydrate ($C_2H_2O_4 \cdot 2H_2O$, Sigma-Aldrich, ≥99%) was used in the synthesis as well. For the synthesis, stoichiometric amounts of $Zr(CH_3COO)_x \cdot (OH)_y$ and $Y(CH_3COO)_3 \cdot 4H_2O$ ($Ce(CH_3COO)_3 \cdot xH_2O$ and $Gd(CH_3COO)_3 \cdot xH_2O$ in the case of GDC synthesis) were dissolved in diluted acetic acid (CH_3COOH, Sigma-Aldrich, ≥99 %). The obtained solution of Y and Zr (Gd and Ce in a case of GDC synthesis) salts was slowly poured into an aqueous solution of oxalic acid under active stirring at 50°C for 30 min. As a result, the formation of white opaque colloidal solution occurred. A concentrated ammonia solution (NH_4OH, 25%) was then added drop-wise to the reaction mixture up to pH 9–10 to promote sedimentation. The precipitate was filtered, washed with distilled water and acetone and then dried for 24 h at 100°C in air. Finally, the dry powder was ground in an agate mortar and then annealed in a furnace at different temperatures for 5 h (5°C/min) in air. The scheme of the process is demonstrated in Fig. 11.
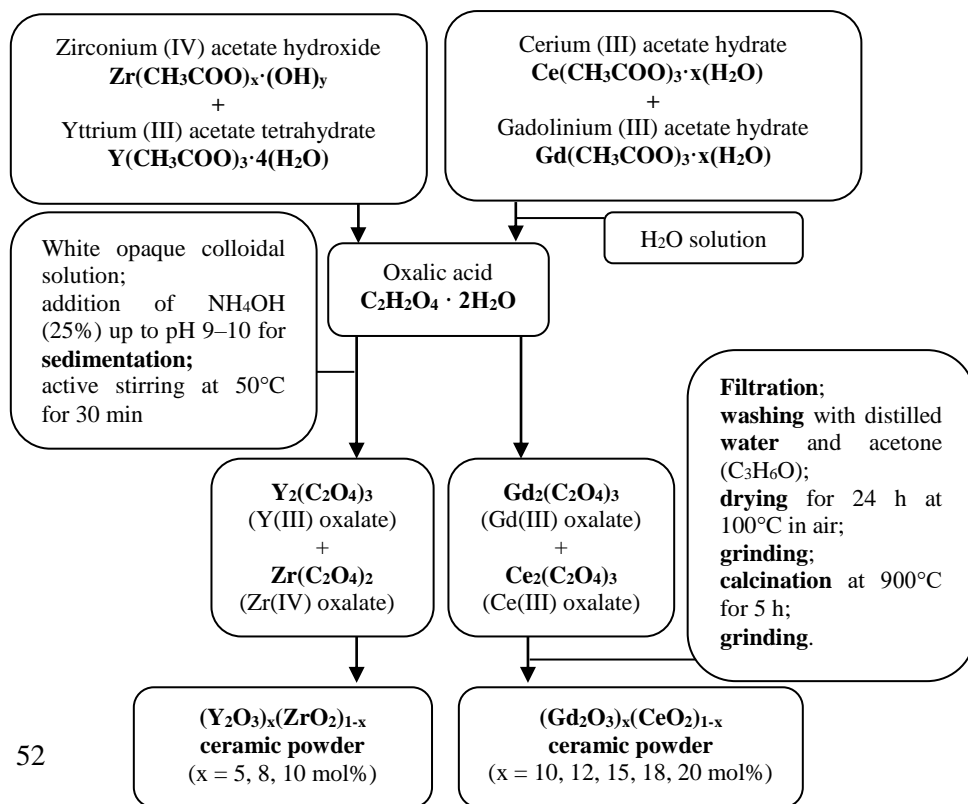
Fig. 11. A scheme of the co-precipitation (CP) synthesis method for the preparation of YSZ and GDC ceramic powder

2.1.1.2. Incipient wetness impregnation method

The incipient wetness impregnation (IWI) method was applied for the preparation of YSZ ceramic powder doped with 15 mol% ceria (denoted as CeO_2-YSZ). The cerium precursor (cerium (III) nitrate, $Ce(NO_3)_3 \cdot 6H_2O$, Sigma-Aldrich, 99.999%) dissolved in an aqueous solution and zirconia-stabilized 8 mol% yttria (8YSZ, Sigma-Aldrich, S_{BET} = 89 m^2/g) were used as initial materials. Three impregnation-drying cycles were carried out. After each impregnation cycle, the mixture was allowed to dry in an oven at 105°C for 24 h. The obtained powder was ground in an agate mortar, and sieved through a 0.075 mm mesh. Finally, the metal precursor was decomposed by the calcination in air at 500°C for 1 h. The scheme of the IWI synthesis method is illustrated in Fig. 12.

$Ce(NO_3)_3$ → Impregnation, drying and calcination for 1 h at 500°C in air → CeO_2 YSZ → **CeO_2-YSZ** ($Ce_{0.13}Y_{0.12}Zr_{0.75}O_{2-\delta}$)

YSZ
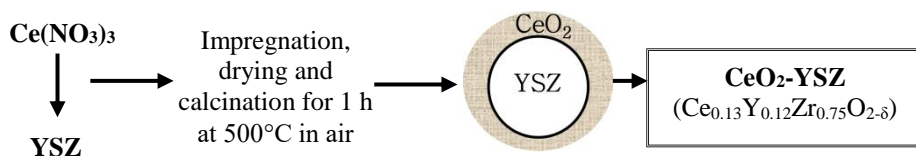
Fig. 12. The scheme of the incipient wetness impregnation (IWI) procedure

2.1.2. Substrates

A commercial silicon (Si) wafer with a thickness of 500 µm (single-side polished, (100), p-type, Sigma-Aldrich); silicon oxide/silicon (SiO_2/Si) wafer (double-side polished, (100), p-type, Sigma-Aldrich) with a SiO_2 thickness of 1 µm; and low stress silicon nitride/silicon (Si_3N_4/Si) wafer with a Si_3N_4 thickness of 500 nm (double-side polished, thickness of Si is 350 µm, University Wafer) were used in this study. A double-side polished α-Al_2O_3 substrate (BK-100-1, Kineshmo, Russia) and electrochemically formed nickel foil (Institute of Materials Science) with a thickness of 40 µm were used as well. The substrates and their applications are summarized in Table 3.

Table 3. A summary of the substrates used in this study

Substrate	Characteristics	Application
Si wafer	single-side polished, (100), p-type, thickness of 500 µm, Sigma-Aldrich	Characterization of electrolyte and electrode thin films.
α-Al_2O_3 plate	double-side polished, thickness of 1 mm, BK-100-1, Kineshmo, Russia	Formation of electrolyte thin film samples for impedance measurements.
Ni foil	electrochemically formed, thickness of	Preparation of CeO_2-YSZ thin

	40 µm, Institute of Materials Science	films.
SiO$_2$/Si wafer	double-side polished, (100), p-type, thickness of Si is 500 µm, thickness of SiO$_2$ is 1 µm, Sigma-Aldrich	Formation of electrolyte thin film samples for impedance measurements; formation and characterization of the PEN three-layered membrane structure.
Si$_3$N$_4$/Si wafer	double-side polished, (100), p-type, thickness of Si is 350 µm, thickness of Si$_3$N$_4$ is 500 nm, University Wafer	Manufacturing of the PEN three-layered membrane structure test samples.

Different substrates were used to achieve several goals: for the characterization of thin film properties and manufacturing of µ-SOFC multilayer membrane structure. In order to characterize the properties of thin films (morphological, structural and electrical properties), Si(100) and SiO$_2$/Si substrates were cut into (1×3) cm^2 pieces, while Al$_2$O$_3$ was cut into (2×2) cm^2 pieces. For the manufacturing of µ-SOFC multilayer membrane structure, Si wafers with a silicon nitride film were incised according to the mark size, prepared by UV lithography using laser cutting. The photomask is illustrated in Fig. 14, Subchapter 2.1.4.1.

2.1.2.1. Substrate surface preparation

In order to avoid such contaminants as organic and inorganic residues, debris etc. and improve the quality, substrates were cleaned. Surface preparation methods involved washing with deionised water and drying under compressed air; RCA-1 cleaning solution (6 parts DI H$_2$O, 4 parts 27% NH$_4$OH, 1 part 30% H$_2$O$_2$) was prepared and heated on a hot plate until it reached boiling point; afterwards, the substrates were immersed into this hot solution for 60 min with continued heating and stirring. Then, the substrates were rinsed 3 times with deionised water and dried under compressed air. Oxygen plasma processing of the substrates was the final step of surface preparation (Subchapter 2.1.2.2).

2.1.2.2. Plasma treatment equipment and experimental details

A plasma treatment is commonly used to clean surfaces from organic contaminants via chemical and physical mechanisms. This process is conventionally performed in the evacuated chamber filled with gas such as oxygen, argon, nitrogen, ammonia, fluorine, acetylene as well as combinations of them, creating the glow discharge plasma [132][133]. Radio frequency (RF), microwaves, and alternating (AC) or direct current (DC) can be used to excite the gas in the reaction chamber. Electrons, ions, radicals, metastables etc., are generated in the plasma resulting in energy transfer from the plasma to the solid during the process. Their interaction with a solid surface (substrate surface) causes surface modification, for instance, etching, deposition, oxidation, surface functionalization, crosslinking etc., and depends on the substrate material exposed to the plasma treatment, the selection of gas or combination of gases, processing time and exposure energies [133]. The surface of the substrate material is modified from several nanometers to ~10 µm in depth. Therefore, current industrial practices call for plasma treatment only as the last step in the surface preparation process aimed to achieve a clean surface. Plasma

treatment can be used to tailor surface adhesion, wetting properties, to introduce functional groups (in a case of polymers), to control the surface roughness, etc.

In this work, the plasma processing where the substrates were exposed to powered RF O_2 plasma in the camera of the Plasma-600-T (JSC Kvartz) device at 133 Pa pressure (RF = 13.56 MHz, P = 0.3 W/cm^2, t = 5 ÷ 10 min), was used to prepare the surface before the formation of thin films (electrolyte, platinum electrodes); and to clean the etched surface after direct Ar$^+$ ion beam etching of platinum and electrolyte thin film.

2.1.3. Thin film preparation methods

2.1.3.1. Electron beam evaporation technique and experimental details

The UVN-71P3 e-beam evaporation system was used for the deposition of electrolyte thin films (YSZ, GDC) (thickness varied from 500 nm to 800 nm). As a source material for e-beam evaporation of electrolyte, commercial YSZ ceramic powder containing 8 mol% of Y_2O_3 (denoted as 8YSZ-45) and synthesized by co-precipitation synthesis method YSZ and GDC ceramic powder containing: 5, 8 and 10 mol% of Y_2O_3, denoted as 5-YSZ, 8-YSZ and 10-YSZ, respectively; also, 10, 12, 15, 18 and 20 mol% of Gd_2O_3, denoted as 10-GDC, 12-GDC, 15-GDC, 18-GDC and 20-GDC, respectively, were used. The powder was pressed into pellets of 13 mm in diameter and annealed at 1000°C (in the case of GDC, the annealing temperature varied in the range of 500–900°C) temperature in air. The evaporation of the YSZ (or GDC) electrolyte was performed at the pressure of 0.7 Pa, and the e-gun power was 10 kW. The distance between the electron gun and the substrate was fixed at 250 mm. During the evaporation process, the temperature of the substrate was kept constant at around 200°C and the thickness of the thin film was controlled by a quartz microbalance sensor. The evaporation rate was ~1.2 nm/s and ~2 nm/s for the YSZ and GDC, respectively. The substrate was heated with infrared (IR) lamp heaters installed in the vacuum chamber. The temperature was controlled with "K" type thermocouple probe contacting the substrate.

Table 4. The main parameters of e-beam evaporation process

Base pressure in chamber: 10^{-3} Pa
Deposition pressure: 0.7 Pa
Gun power: 10 kW
The maximum emission current: 500 mA
Deflection of electrons: 180°
Electron beam diameter: 1 mm
Temperature of the substrate: 200°C
Growth rate: ~1.2 nm/s (for YSZ) and ~2 nm/s (for GDC)
Thickness monitoring: quartz crystal deposition controller

2.1.3.2. Magnetron sputtering deposition technique and experimental details

Sputtering is a PVD process used for the deposition of materials onto a substrate, by ejecting atoms from target materials and condensing the ejected atoms onto a substrate in a high vacuum environment. In the sputtering process, the target

(or cathode) material is bombarded by energetic ions generated in glow discharge plasma, placed in front of the target. The energetic bombardment process causes the removal of atomised material from a solid (target), which may subsequently condense on the substrate as a thin film. Secondary electrons are also emitted from the target surface as a result of ion bombardment, which plays an important role in maintaining the plasma [134].

Reactive sputtering can be determined as the sputtering of elemental targets in the presence of chemically reactive gases (the sputtering gas is often an inert gas, for instance, argon) which mass reacts with both the ejected target material and the target surface.

In the process of magnetron sputtering, permanent magnets behind the cathode are arranged in order to create a region of magnetic field directly above the target (see Fig. 13). One magnetic pole is positioned at the central axis of the target and the second pole is formed around the outer edge of the target material. The magnetic field traps the energetic electrons and effectively increases the ionization efficiency resulting in the formation of dense plasma in the target region [135]. A negative voltage of typically -300 V or more [134] is applied to the target as well as the substrate ion current density of <1 mA/cm^2 is generated during the process.

In order to sputter conducting target materials, a direct current (DC) power supply is generally used. For insulating or semiconducting targets, a radio frequency (RF; usually 13.56 MHz) power supply is required.

Magnetron sputtering has the following advantages: appropriate control on the chemical composition, high deposition rates and low substrate heating during the deposition process; it is a very popular technique in the search for new material properties, for the deposition of a vast range of compound and alloy thin films including oxides, nitrides, carbides, fluorides or arsenides [136]. Consequently, magnetron sputtering makes an important impact on the areas of application, including hard, wear-resistant coatings, low friction coatings, corrosion-resistant coatings, decorative coatings and coatings with specific optical or electrical properties, etc.
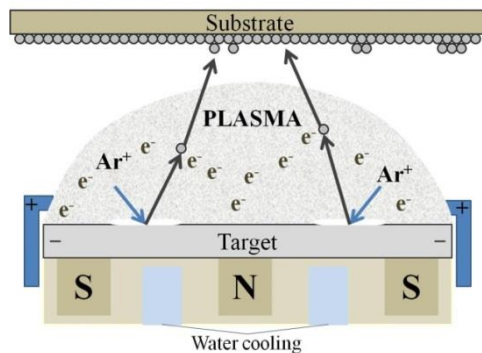
Fig. 13. A schematic of magnetron sputtering deposition process

In this work, a DC magnetron sputtering source ("Kurt J. Lesker" company) which was integrated in a "Leybold Heraeus-A-700-QE" device vacuum system was

used for the deposition of platinum electrodes and titanium adhesive layer films. Pt electrodes with a thickness of 200 nm were deposited on SiO_2/Si, $Ti/SiO_2/Si$, Si_3N_4/Si, $Ti/Si_3N_4/Si$, $YSZ(GDC)/Pt/Ti/SiO_2/Si$ and $YSZ(GDC)/Pt/Ti/Si_3N_4/Si$ substrates.

A turbomolecular pump was used to evacuate the main chamber to a base pressure of 2×10^{-4} Pa. Argon (purity 99.996%) was used as the sputtering gas. Argon pressure in the chamber during deposition mainly was 0.065 Pa. In order to measure the influence of magnetron sputtering deposition conditions and thermal treatment on the properties of Pt thin films, argon pressure in the chamber varied systematically as follows: 4.9 Pa, 0.13 Pa, 0.6 Pa, and 0.065 Pa (further discussed in Subchapter 3.3): first (1st), second (2nd), third (3rd) and fourth (4th) sample series, respectively.

The Pt target (purity 99.99%, Lesker) (and the Ti target (purity 99.6%, Lesker)) with a diameter of 5.08 cm was placed at a distance of 16 cm from the substrate and tilted at a 30-degree angle with respect to the substrate. The substrate holder was rotated during the deposition process in order to obtain a homogeneous distribution of the film thickness. The substrates were heated to 150°C during the Pt electrode (or Ti adhesive layer) deposition process. Substrate was heated with infrared (IR) lamp heaters installed in the vacuum chamber. The temperature was controlled with "K" type thermocouple probe contacting the substrate. The magnetron voltage was 510 V, and the current was 0.4 A. The growth rate was determined by a quartz microbalance sensor.

2.1.4. The formation of μ-SOFC membrane structure and the micropatterning of platinum electrodes

2.1.4.1. UV lithography

In general, the lithography process is conventionally used for the fabrication of micro- and nano-structures on a surface [137]. This process uses light or other techniques to transfer the required pattern from the mask to a light- (photolithography) or other rays-sensitive material deposited as a thin film on the structural material, e.g. a silicon wafer. Depending on the type of rays used, there are lots of well-known types of lithography, for instance, lift-off lithography, electron beam lithography, nanoimprint lithography, X-ray lithography, focused ion beam lithography, atomic force nanolithography, extreme UV lithography, etc. [137].

This work uses UV photolithography. The basic steps of the photolithography process involve substrate cleaning, barrier layer formation, photoresist (it is an organic, light-sensitive material) application, soft baking, mask alignment, exposure and development, and hard-baking. The resolution of about 1 μm using light of 400 nm can be achieved using this type of lithography [137]. Two types of photoresist, positive and negative, can be used in the process. For the positive resist, the exposed with UV light regions present a higher solubility in the developing solutions, while the negative resist exposure to the UV light causes the negative resist to become polymerized, and more difficult to dissolve.

In the case of μ-SOFC formation, two separate tasks require accurately aligned photolithography on both sides of the double-polished silicon wafers. The first task is to fabricate a freestanding tri-layer membrane structure on the top of the substrate. The second task is to form "backside open windows" to be used as the inflow of fuel. Therefore, double sided-pattern alignment of mask for the fabrication of freestanding membrane structures was applied in this work. Before micro-patterning, the substrates were washed with alcohol and processed with oxygen plasma treatment, which helps to avoid any residues on the surface and improves the adhesion between films and the quality of the electrodes.

In order to fabricate a μ-SOFC membrane structure, the positive photoresist (ma-P 1205, Micro Resist Technology, Germany) was used. Furthermore, distances of 2, 4, 6, 8 and 10 μm between Pt electrodes, utilized in the impedance measurement of electrolyte thin films, were formed using the negative photoresist (ma-N 2400, Micro Resist Technology, Germany). The photoresist was sensitive to light radiation from 300 nm to 440 nm. The film of the resist (thickness of 500 nm) was distributed on cleaned substrate using the spin-coating process (centrifugal machine Dynapert Precima) at a rotation speed of 2500 min^{-1}. Finally, the sample was soft baked at 100°C ± 1°C for 10 min in a desiccation system (LADA). The roughness of the sample was about 5 nm. The sample with such photoresist was positioned beneath the photomask, which was fabricated from chromium and soda lime glass, and illuminated with a UV light ($\lambda = 365$ nm, the intensity of 55 mJ/cm^2) for 7 s. The photomasks used in this work are illustrated in Fig. 14.

The dimensions of one squared membrane were 2.4 × 2.4 mm.

(a)   (b)
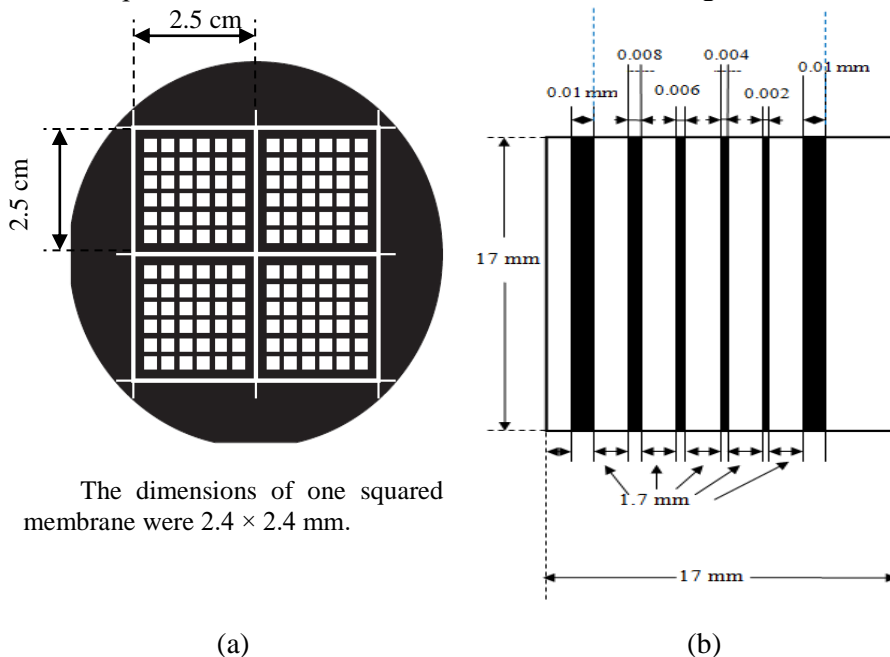
Fig. 14. The photomask: (a) used for the formation of μ-SOFC membrane structure; (b) used for the preparation of Pt electrodes employed in impedance measurements of electrolyte thin films

A schematic representation of the basic steps of UV lithography used in this work is illustrated in Fig. 15 as well.
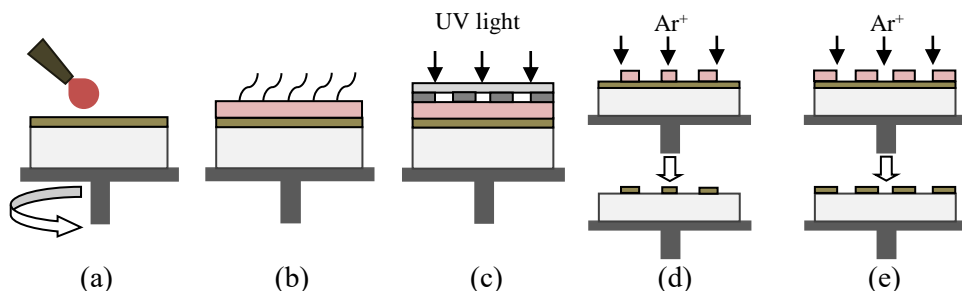
Fig. 15. The basic steps of the UV photolithography process: (a) photoresist deposited by spin-coating; (b) drying of the photoresist; (c) alignment and exposition to UV light with the mask; d) development of the *positive* photoresist followed by direct Ar$^+$ ion beam etching of the structures (in the formation of μ-SOFC); e) development of the *negative* photoresist followed by direct Ar$^+$ ion beam etching of the structures (in the formation of Pt microelectrode)

The microstructures formed on a sample surface were achieved with a combination of UV photolithography and direct Ar$^+$ ion beam etching technologies (Fig. 15). Thus, the final resist pattern is binary: parts of the substrate are covered with resist while other parts are fully uncovered (Fig. 15 (d), (e)). This binary pattern plays an important role of protection during the etching process.

The resist remover mr-Rem 660 (based on N-methylpyrrolidon (NMP)) was used to rinse the samples exposed by UV light. Washing was carried out for 3 s at room temperature ($20 \pm 5°C$). Then samples were rinsed with deionized water and dried under compressed air. In addition, all the samples were processed with oxygen plasma treatment for 3 min. Detailed information on the production of microstructures is provided in subchapter 4.1, where the design of the technological route for the production of a μ-SOFC multilayer membrane structure is presented.

2.1.4.2. Etching

In general, etching can be divided into two categories, i.e. wet etch and dry (or plasma) etch [138]. The etching process aims to create topographic features on a surface by selectively removing material through physical or chemical means [139]. In this work, dry etching processes were employed. The removal of the substrate material by dry etching requires high kinetic energy ion, electron or photon beams, while chemical dry etching involves a gas-solid chemical reaction which takes place in the presence of plasma, an electrically neutral mixture of molecules, atoms, ions, electrons, and photons [138]. Thus, chemical plasma etch occurs via the strong material selective formation of volatile compounds by radicals in the plasma, which hit the surface, while the physical etching occurs via the weak material selective sputtering of the substrate by ions accelerated by an electrical field. In summary, the reaction that takes place can be performed utilizing high kinetic energy of particle beams, chemical reaction or a combination of both.

Reactive ion etching (RIE) is an ion-assisted reactive etching method, which combines the effects of chemically active gaseous radicals and physical ion bombardment, used in the manufacturing of topographical structures in micro- and nanotechnologies to create various structures and devices. RIE allows isotropic and anisotropic material removal reactions to occur in the gas phase. This process takes place in a chemically reactive plasma generated from the gas that is pumped into the reaction chamber, e.g. Cl-based (Cl_2, BCl_3), F-based (SF_6, CF_4, C_4F_8, CHF_3) and O-based (O_2, O_3, CO_2) etc. The plasma is generated by an RF generator (13.56 MHz). The selection of gases depends on the sample material to be etched. RIE mostly employs ion-assisted processes, where ions attack the sample surface and react with it. Chemical bonds are damaged by heavy ion bombardment, and the radicals chemically react with the exposed surface atoms, producing a volatile gaseous material leaving the surface.

In this work, the etching of silicon nitride (and silicon oxide) layer was performed in the PK-24030PD (Plasma-Therm Inc.) reactor creating CF_4/O_2 plasma. The CF_4/O_2 plasma is commonly used for the RIE process of SiO_2 or Si_3N_4 layer. The process of the etching in RIE environments using fluorocarbon-based plasmas with oxygen additions is sometimes called as plasmochemical etching. Prior to the etching process, auxiliary Al layer (thickness of 300 nm) was evaporated using the e-beam evaporation technique (experimental details are described in subchapter 2.1.3.1). During the etching process, the following parameters are maintained: the frequency of discharge was 13.56 MHz; the percentage of CF_4 and O_2 gas in the CF_4/O_2 gas mixture was 80 and 20%, respectively; the discharge power density was 0.75 W/cm^2; the pressure was 65 Pa; the energy of incident ions was ~20 eV; and the etching time was 5 min.

Deep reactive ion etching (DRIE) is a modified RIE process. These methods rely on the same etching mechanisms: chemical etching and ion bombardment; however, DRIE enables the production of deeper and narrower structures with a high etch rate as compared to conventional RIE. Unlike RIE, DRIE reactors are equipped with two power sources to create alternating etch and passivation cycles [140]. High anisotropy and etching rates can be achieved using the DRIE technique, obtaining patterns with maximal aspect ratios and resolution [141].

In this work, a DRIE of silicon was prepared using the universal plasma processing system, Apex SLR (Plasma-Therm Co.) which can be configured to perform inductively coupled plasma (ICP) etching or high density plasma chemical vapour deposition. The ICP etching system employs a cylindrical coil which creates plasma. The use of multipole permanent magnets is not indispensable but the presence of them increases the plasma density and mainly creates uniform plasma. The magnetic field in the reactor is induced by applying RF voltage to the coil. Additional (RF, low frequency or DC) bias voltage to the substrate holder increases the ion bombardment on the sample surface (substrate), and enables independent control of the plasma density or the energy of the incoming ions.

Pulsed etching, also known as the Bosch process, which alternates between etching and polymerization modes to get vertical etch walls, was used to etch silicon through the silicon wafer up to the silicon nitride/silicon oxide film. The auxiliary Al

layer (thickness of 300 nm) on the back surface of the wafer was necessary, whereas pure silicon nitride layer can be attacked by the process gas plasma. DRIE conditions are defined by many parameters, such as RF power, gas-flow rate, ICP source power, chamber pressure and stage (bottom electrode) temperature that affect the etch rate, profile and uniformity of etch patterns throughout the sample [141]. After the Bosch process, the auxiliary Al layer was removed using the Al etchant (Al-12S, "Sunchem AB"). The basic parameters of the DRIE process are presented in Table 5.

Ion beam technology allows the sample surface to be etched by the use of broad beams of positively charged ions in a vacuum system [30]. In the *ion beam etching (IBE)* process, ions are directed at the sample surface to be patterned. IBE is an anisotropic etching process that precisely reproduces the mask pattern on the sample surface. The gas (e.g. Ar^+) is ionized by energetic electron bombardment in a discharge chamber during the etching process. The forming ion beam is used to sputter etch material (ions, with sufficient energy, dislodge atoms or molecules from a substrate surface) over a photoresist mask in order to obtain the desired pattern.

Table 5. Deep reactive ion etching (Bosch process) conditions

Parameter	Passivation phase	Etch phase
Cycle time (s)	7	10
Pressure (Pa)	2.4	4.7
C_4F_8 gas flow (sccm)	80	0
SF_6 gas flow (sccm)	0	130
O_2 gas flow (sccm)	0	13
ICP source power (W)	600	600
Bias power (W)	0	20
Bottom electrode chiller temperature (°C)	15	15
Etching rate (μm/min)	3.5	

In this work, the structures were etched (distance among Pt electrodes used in the impedance measurements; μ-SOFC membrane) with the USI-IONIC device. The main parameters of the device are presented in the Table 6. The bombardment in IBE was performed by Ar^+ ion beam using multi-cell cold hollow-cathode DC ion beam source (Ar^+ ion energy 300 eV, ion beam current 0.25 mA/cm^2, pressure 0.133 Pa, substrate temperature 293 K ±5 K). The etching time duration of 10 and 16 min for the formation of Pt microelectrodes on the electrolyte surface and the formation of the free standing membrane structure was carried out, respectively.

Table 6. The main parameters of the device USI-IONIC

Base vacuum in the chamber: $5×10^{-4}$ Pa
Technological pressure in the chamber: $7×10^{-2} – 4×10^{-1}$ Pa
Ion beam energy: 0–500 keV
Ion beam current density: 0.01–0.30 mA/cm^2

2.2. Analytical methods and equipment

2.2.1. Thermogravimetric analysis and experimental details

Thermogravimetry is one of the oldest thermal analytical procedures, which involves monitoring the weight loss of the sample in a given atmosphere as a function of temperature [142]. The measurements typically provide basic information regarding the thermal stability of both organic and inorganic compounds and composites. Usually, thermogravimetric analysis (TGA) includes the determination of degradation rates, moisture content, and residual solvents. The common thermogravimetric system consists of a diluent gas flowing over a sample which is placed on a sensitive balance inside a temperature-controlled chamber [143]. Environment of N_2, O_2, air, He is available during the measurements. Mass, enthalpy, and temperature (typically the difference between the sample and a suitable reference) are the properties measured during TGA, differential scanning calorimetry (DSC) or differential thermal analysis (DTA) experiment, respectively, mainly under non-isothermal conditions at a constant heating rate. TGA measures the mass change of the sample material. Different processes may cause mass changes, such as decay, decomposition, sublimation, evaporation, adsorption, desorption, oxidation, reduction etc. Meanwhile, DSC measures the heat flow associated with phase transitions or reactions, such as melting, solid phase transition, crystallization, sorption, curing etc. as a function of temperature and time. Most often, simultaneous thermal analysis is used in combination with several methods, e.g. thermogravimetric and differential scanning calorimetry (TG-DSC) analysis, performing simultaneous measurement of the same sample in a single instrument at the same conditions (atmosphere, vapour pressure of the sample, heating rate, gas flow rate, thermal contact to the sample crucible and sensor, radiation effect, etc.)

The thermal decomposition of the co-precipitated Y-Zr and Gd-Ce oxalates were analysed utilizing the TG-DSC analysis using PerkinElmer STA 6000 Simultaneous Thermal Analyzer. Dried samples of about 5–10 mg were heated from 25 to 950°C at a heating rate of 10°C/min in a dry flowing air (20 mL/min). TG-DSC measurements were performed to find out the annealing temperature needed for the co-precipitated Y-Zr and Gd-Ce oxalate powders, ensuring the removal of organic compounds, formation of oxides, and stabilization of the powder structure. The TG-DSC spectra was processed with the Pyris software. The basic specifications of STA 6000 Simultaneous Thermal Analyzer are presented in Table 7.

Table 7. The main parameters of the STA 6000 Simultaneous Thermal Analyzer

Sensor: pure platinum pan holder and reference ring
Furnace design: vertical
Balance design: top loading, single beam
Balance resolution: 0.1 µg
Balance measurement range: up to 1500 mg
Heating rate: ambient to 1000°C
Cooling rate: from 1000°C to 30°C (under 10 min)

| Temperature calibration: metal standards such as Indium and Silver |
| Temperature accuracy: < ±0.5°C |
| Calorimetric data: accuracy/precision ±2% (based on metal standards) |
| Thermocouples: PT-PT/Rh (Type R) |
| Sample pans: alumina 180 µl |

2.2.2. X-ray diffraction analysis and experimental details

X-ray diffraction analysis (XRD) is an extremely important technique in the field of materials science which allows to obtain qualitative and quantitative information on the atomic scale from crystalline compounds [144–146]. The evaluation of atom arrangement inside solid crystals is relevant when clarifying the properties of materials.

Electromagnetic radiation, with the wavelength of ~1 Å, produces the diffraction pattern followed by the interaction with crystalline solids because of the λ, which is typically in the same order of magnitude as the spacing d between planes in the crystal. The XRD technique utilizes a focussed X-ray beam that is directed at the material. Due to the interaction of X-ray with electrons of the material atom, secondary spherical waves are produced and elastically is scattered from the electrons. This way, a regular set of spherical waves is produced. Thus, destructive or constructive interference occurs in different directions concerning the superposition of waves. Destructive interference results in the destruction of waves. Meanwhile, diffraction peaks generated by constructive interference of the waves in a few specific directions, can be determined by Bragg's law presented by the equation:

$$n\,\lambda \; = \; 2d\,\sin\,\theta; \tag{15}$$

where n is any integer, λ is the wavelength of the X-ray beam, d is the spacing between diffracting planes, θ is the incident angle. Hence, according to Eq. (15), the angle of diffraction is dependent on the spacing of the molecules (d-spacing) [144]. The conversion of diffraction peaks to d-spacings allows to identify the material. Furthermore, broadening of the obtained diffraction peaks occurs due to small domain sizes in nanocrystalline solids; therefore, it is used to evaluate the crystallite sizes. Thus, XRD data after processing reveals some information about the crystalline structure, defects, stresses, etc. of the sample [146].

In this research, XRD analysis with parallel beam geometry was carried out. This geometry, compared to conventional Bragg-Brentano geometry, helps to avoid certain constraints, such as cost of very precise alignment requirements, difficult preparation of the sample, fixed source-to-sample and sample-to-detector distance, unacceptable sample displacement errors due to mis-positioning, limitations because of the roughness or partial transparency of the sample, etc. [147].

The crystallographic nature of the synthesized ceramic powder and thin films of µ-SOFC construction element was determined using the D8 Discover X-ray diffractometer (Bruker AXS GmbH) with $Cu\ K_\alpha$ ($\lambda = 1.5418$ Å) radiation. A parallel beam geometry with 60 mm Göbel mirror (i.e. X-ray mirror on a high precision parabolic surface) was used. This configuration allows to transform the divergent

incident X-ray beam from a line focus of the X-ray tube, producing a parallel X-ray beam that is free of K_β radiation. The Soller slit with an axial divergence of 2.5° was utilized in the primary side. Diffraction patterns were recorded using a fast-counting LynxEye (0D mode) Silicon Strip detector with an opening angle of 2.475° and a slit opening of 6 mm. The XRD measurements were performed using generator voltage and a current of 40 kV and 40 mA, respectively. The samples were scanned (coupled $2\theta\text{-}\theta$ scans) over the range of 5–135° with a step size of 0.02°, time per step of 0.2 s and auto-repeat function enabled. Also, the grazing incidence measurement of thin films was utilized using a grazing incident angle that varied from 1 to 5°. The resultant diffractograms were processed with the Diffrac.EVA software. Phase identification was executed by matching XRD patterns with the powder diffraction files (PDF) database of International Centre for Diffraction Data (ICDD).

Conventionally, the $\sin^2\psi$ method is a widely used technique for the evaluation of stresses due to lattice deformation measured by XRD analysis [145,148,149]. In this method, the position of a particular ($h\ k\ l$) reflection at different sample tilt angles (ψ) are measured from a coupled θ–2θ scan, and the lattice strain perpendicular to the $\{h\ k\ l\}$ planes at different ψ is calculated from the measured peak position [149]. In general, the orientation of the sample can be described by two Euler angles, ϕ and ψ. The ϕ angle is the rotation angle of the sample about its surface normal, while the ψ angle is the angle between the normal to the surface and the normal to the diffracting lattice planes [150]. However, assuming that there is no shear stress, the rotation angle ϕ is 0°. According to the results of measurements, the corresponding interplanar spacing $d_{\phi\psi}$ is calculated with the Bragg law.

Theoretically, stress analysis can be performed using the rational strain definition according to this relation [151,152]:

$$\varepsilon_{\phi\psi} = ln\left(\frac{a_{hkl}}{a_0}\right) = ln\left(\frac{d_{hkl}}{d_0}\right) = ln\left(\frac{sin\theta}{sin\theta_0}\right); \qquad (16)$$

where $a_{hkl} = d_{hkl}\sqrt{h^2 + k^2 + l^2}$ and a_0 represent the strain-free lattice parameter, d_0 is an interplanar distance, and $\varepsilon_{\phi\psi}$ is the strain in (ϕ, ψ) direction. Moreover, the strain ($\varepsilon_{\phi\psi}$) can be expressed by using other Cartesian strain tensor components, ε_{ij} as follows [151]:

$$\varepsilon_{\phi\psi} = \left(\varepsilon_\phi - \varepsilon_{33} + \varepsilon_{12}sin2\phi\right)sin^2\psi + \left(\varepsilon_{13}cos\phi + \varepsilon_{23}sin\phi\right)sin2\psi + \varepsilon_{33}. \qquad (17)$$

Combining equations (16) and (17) within the linear elasticity framework, and assuming in-plane isotropic stresses, the relation can be written as [151]:

$$ln\left(\frac{1}{sin\theta_{hkl}}\right) = \frac{1}{2}S_2\sigma sin^2\psi + 2S_1\sigma + ln\left(\frac{1}{sin\theta_0}\right); \qquad (18)$$

where σ is the amplitude of the residual stresses, the S_2 and S_1 are elasticity constants that can be expressed as a function of the Young's modulus, E, and the Poisson ratio, v, relative to the considered $\{h\ k\ l\}$ planes by $S_2 = \frac{(1+v)}{E}$ and $S_1 = -\frac{v}{E}$.

Graphic representation of the results by plotting the $ln(1/sin\theta)$ as a function of $sin^2\psi$ curves gives a linear relation. It is possible to deduce the residual stress

amplitude from the slope of the fitted linear curve, while the stress-free lattice parameter can be extracted from the ordinate intercept [148].

In this research, residual stress of the Pt electrodes was characterized using the $\sin^2\psi$ method. The experiment was carried out measuring the (3 3 1) reflecting plane and defined for the six values of the ψ angle that varied from 0 to 50.77°. The samples were positioned using a centric Eulerian cradle sample stage. A collimator of the size of 1 mm was used to focus the X-ray beam for the stress measurements.

2.2.3. Atomic force microscopy and experimental details

Atomic force microscopy (AFM) is a very high-resolution type of scanning probe microscopy technology. The AFM system has a variety of possible imaging modes, such as contact mode, non-contact mode and tapping mode. This surface analysis technique is intended for the measurement and analysis of surface micro- and sub-microrelief, objects of the micro- and nanometer range with high resolution [153,154].

The operation of AFM is based on the interaction of a sharp probe (with a radius from 5 to 20 nm) attached to the free end of a smooth cantilever with a sample surface that is brought in contact with the probe. The local attractive (the probe is attracted towards the sample) or repulsive (the probe is repulsed from the sample) molecular force is detected. The force between the cantilever probe and the sample surface is converted into the bending (deflection) of the cantilever, which is detected by a laser focussed on the back of the cantilever. The laser is reflected by the cantilever onto a photodetector, which is usually a photodiode with quadrupole-electrode geometry. The movement of the laser spot on the photodetector gives a measurement of the movement of the probe.

A detailed characterisation of the surface morphology of the thin films can be carried out finding such roughness parameters, as mean height (Z_{mean}), average roughness (R_a), root mean square roughness (R_q), valley depth, peak height, peak-valley height, skewness (R_{sk}), kurtosis (R_{ku}) etc. The R_q is the average of the measured height deviations taken within the evaluation area and measured from the mean linear surface. The skewness (R_{sk}) of a profile is used to measure the symmetry of the profile within the evaluation area. The negative R_{sk} value indicates a predominance of valleys, while a positive value indicates a surface dominated by peaks. Kurtosis describes the randomness of heights, as well as the sharpness of the surface. For a Gaussian-like surface, R_{ku} has a value of 3; the farther R_{ku} is from 3, the less random and more repetitive the surface is [155]. In addition, force-distance curves may be used for the derivation of the surface adhesion forces and object stiffness coefficient.

Generally, the AFM technique can be used in wide-range applications, including nanotechnologies, thin-film technologies, microelectronics, micro- and nano-tribology, optics, testing systems of the precision mechanics, magnetic recording, vacuum engineering, biology, and colloid science studies, etc. [156].

AFM experiments in this work were performed in air at room temperature using the NT-206 (Microtestmachines Co.) atomic force microscope and the SurfaceXplorer SPM-data processing software. A V-shaped silicon cantilever

(spring constant of 3 N/m, tip curvature radius 10.0 nm, cone angle 20°) operating in the contact image mode with $12\,\mu m \times 12\,\mu m$ field of view was used in all measurements. The surface morphology and roughness parameters were evaluated in terms of AFM surface topography images: root mean square roughness (R_q), skewness (R_{sk}), mean height (Z_{mean}) and kurtosis (R_{ku}) of platinum and electrolyte thin films were. The main parameters of the device are given in Table 8.

Table 8. The main parameters of the atomic force microscope (NT-206)

Scan field area: up to $50 \times 40\,\mu m$
Maximum range of measured heights: $\sim 2\,\mu m$
Lateral resolution (plane XY): 1–5 nm (depending on sample hardness)
Vertical resolution (direction Z): 0.1–0.5 nm (depending on sample hardness)
Scanning matrix: up to 1024×1024 points
Scan rate: 40–250 points/s in X-Y plane
Minimum scanning step: 0.3 nm
Sample size: up to $30 \times 30 \times 8$ mm
High voltage amplifier output: ±190 V

2.2.4. Scanning electron microscopy, energy dispersive X-ray spectroscopy and experimental details

In this work, scanning electron microscopy (SEM) was used to evaluate the microstructure of pressed ceramics annealed at high temperatures, as well as the surface microstructure and cross-section of thin films (structure, agglomerates, thickness, trends of growth etc.).

The operation of the SEM is based on scanning an electron beam (with the energy ranging from 0.2 keV to ~40 keV) across the sample producing various signals that reveal information about the sample, like surface topography, microstructure or chemical composition [157].

The electrons which hit the surface, interact elastically or inelastically with the atoms of the sample. The incident electrons are back-scattered from the sample surface or are scatter-diffused into the sample material. Due to the excitation of the atomic surface-species, secondary electrons, back-scattered electrons, X-rays, light, sample current and transmitted electrons are produced as well. Thus, various signals are generated, and the most commonly used ones are those from secondary electrons (SE) and backscattered electrons (BSE). SE's which are generated in a depth of several nanometers below the sample surface, contain information about the features of the sample's surface and are collected by the secondary electron detectors [158]. The imaging of the SE's is a standard mode of operation in all SEM and can produce very high-resolution images of the sample surface, revealing surface details down to a nanometer. BSE's provide important information about the composition, surface topography, crystallinity and magnetism of the sample [159]. In contrast with the SE signal, the BSE signal represents not only the local topography of the sample, but also the information about the local atomic composition of it. [157]. SEM analysis can be performed in high or low vacuum as well as in wet conditions.

In order to obtain the chemical composition of the sample, an attachment of energy dispersive X-ray spectrometer (EDS) detector in SEM can be used. EDS

makes use of the X-ray spectrum produced by inelastic collisions of the incident electrons by electrons in discrete shells of atoms in the sample. Typically, all elements from the atomic number 4 (Be) to 92 (U) can be detected; however, not all instruments are equipped for light elements (Z < 10). Samples can be analysed in different modes, such as: spot analysis, line scans or elemental mapping.

In this work, the microstructure of thin films and ceramics was examined by SEM on Raith e-LiNE plus ultra-high resolution Scanning Electron Microscope, equipped with an in-lens detector and a conventional secondary electron detector, and Energy Dispersive X-Ray Spectrometer Bruker Quantax 200, equipped with 5th generation Si-Drift Detector with <129 eV energy resolution, without special sample preparation. Also, a high resolution scanning electron microscope FEI Quanta 200 FEG (accelerating voltage varied from 0.2 to 30 kV; resolution – 1.2 nm) was used. Etched surfaces (structures) were observed using Raith e-LiNE (accelerating voltage – 10 kV; resolution – 1 nm) SEM. The porosity of Pt thin films (electrodes) was estimated using the ImageJ 1.45 image processing technique with the addition of Pore analysis program.

2.2.5. X-ray photoelectron spectroscopy and experimental details

X-ray photoelectron spectroscopy (XPS), also known as electron spectroscopy for chemical analysis (ESCA), is currently the most widely used surface analysis technique which is based on the photoemission effect [160]. XPS provides quantitative and chemical state information from the surface of the material in the depth range of 1–10 nm. All surface elements (excluding hydrogen and helium) can be identified and quantified. The surface can be analysed with a relative accuracy of 5% using elemental sensitivity factors, and with a detection limit of about 0.1% atomic concentration.

The sample surface is irradiated with a low energy X-ray, which excites the electrons of the sample atoms (the core level electrons of the surface atoms absorb the X-ray photon energy) and if their binding energy is lower than the X-ray energy, they will be emitted from the atom with a certain kinetic energy as photoelectrons. The number of these photoelectrons which escaped from the top surface of the sample is detected and analysed. Their kinetic energy is registered and simple calculations provide information about the binding energy for electrons in the core shell of atoms. The peak in a photoelectron spectrum, recorded by counting the ejected electrons over a range of electron kinetic energy, reveals the information about the elemental identity, chemical state, and the amount of detected element.

It is well known that corrosion rates, catalytic activity, adhesive properties, wettability, contact potential and failure mechanisms are the factors which are governed by the surface chemistry [160]. The XPS technique provides data regarding thin film surfaces and structures, which is important for many industrial or research application such as nanomaterials and electronic devices, surface treatments, thin film technologies, bio-active surfaces, etc., where the properties of the surface play a crucial role.

The atomic composition of the as-deposited and annealed Pt/Ti thin films and electrolyte thin films was studied using the XPS analysis technique. For the surface

analysis, the Thermo Scientific ESCALAB 250Xi spectrometer with a monochromatized AlK$_\alpha$ radiation (hv = 1486.6 eV) was used. The base pressure in the analytical chamber during spectra acquisition was higher than 2×10^{-7} Pa. X-ray spot size for the spectra acquisitions was 0.3 mm. The 40 eV pass energy was used for the spectra acquisition. Energy scale of the system was calibrated according to Au 4f7/2, Ag 3d5/2 and Cu 2p3/2 peaks position. The calculations of atomic concentration were performed using an original ESCALAB 250Xi Avantage software. Thin films were analysed without surface cleaning procedure.

2.2.6. Resistivity measurements using four-point probe method. Experimental details

Due to its low demand on sample preparation and high accuracy, the four-point probe method is a simple method used for studying the electrical properties of solids and thin films in material science and semiconductor industries [161]. Because of the fact that μ-SOFC works sufficiently at high temperatures (>500°C), electrodes have to maintain the relatively high electrical conductivity, even after exposition at operating temperatures [8]. Thus, the assessment of these characteristics is required. Generally, electrical resistivity measures how a strongly investigated material opposes the current flow. The electrical resistivity of thin conducting films influences the operating frequency of the device, current, and Joule heating of the device, which in turn can cause electromigration [105,107]. The SI unit of resistivity is [Ω·m]; also, [Ω·cm] unit is available. The electrical resistivity of the sample, e.g. Pt electrode thin film, can be evaluated using the four-point probe method by flowing a current though two outer probes and measuring the voltage through the two inner probes (see Fig. 16).
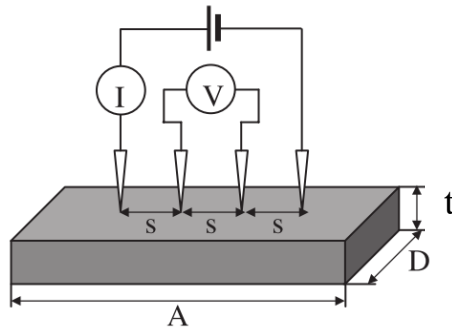
Fig. 16. A schematic of the four-point probe method [162]

The output in such a system is in units of ohm (resistance, R); therefore, if the probe spacing (s) is known, resistivity (ρ) can be calculated using the following equation:

$$\rho = 2\pi s R. \tag{19}$$

According to the measurement of sheet resistivity, Eq. (19) has to be changed as follows [162]:

$$\rho = \frac{\pi}{\ln(2)} t \frac{E}{I} \qquad (20)$$

where E is the voltage (V), and I is the current (A), as well as $\frac{\pi}{\ln(2)} = 4.532$. Consequently, the sheet resistivity for a thin sheet can be expressed as:

$$\rho = 4.532t\left(\frac{E}{I}\right) = 4.532tR, \qquad (21)$$

where t is the film/wafer thickness. Eq. (21) can be utilized when the film/wafer thickness is less than half of the probe spacing ($t < s/2$), while for thicker films Eq. (21) becomes:

$$\rho = \frac{E}{I} \frac{\pi t}{\ln\left(\frac{\sinh\left(\frac{t}{s}\right)}{\sinh\left(\frac{t}{2s}\right)}\right)}. \qquad (22)$$

Expression (22) is independent of the probe spacing (s).

In this work, the resistivity of the µ-SOFC electrodes, i.e. Pt thin films (with adhesive layer of Ti), was measured using this method. The four-point probe was placed in contact with the surface of the Pt/Ti film and a fixed current of 11 mA was applied across the outer two probes. The distance between the adjacent probes was 2 mm. The voltage drop was measured across the two inner probes. Five sets of measurements were made for each thin film. The average value of resistivity for each Pt/Ti thin film was determined according to the calculations described above.

2.2.7. Impedance spectroscopy

Impedance spectroscopy (IS), sometimes known as AC (alternating current) impedance, is a powerful tool for characterising materials. The utility of IS relies on the capability to exclude the dielectric and electrical properties of individual contributions of components under investigation [163].

Generally, electrical resistance (R) of the sample can be determined using the Ohm's law, which defines R in terms of the ratio between voltage, E, and current, I as follows:

$$R = \frac{E}{I}. \qquad (23)$$

However, Eq. (23) is suitable only for the ideal resistor. In ceramic materials with prevailing ionic conductivity, impedance measurements reveal more detailed information. Therefore, the impedance, which is a measure of the ability of a circuit to resist the flow of electrical current, is the most commonly used, instead of the term of resistance. Impedance measurements contain information about the physical characteristics of an electrochemical system, for instance, electrode reaction rates; therefore, IS is a widely used tool of analysis in electrochemistry for fuel cells, batteries, corrosion studies, etc. [164].

Impedance measurement is usually carried out by applying an alternating signal (sinusoidal potential excitation) to the system to be investigated followed by measuring the alternating current signal through the cell [164]. The current signal

can be evaluated as a sum of sinusoidal functions. The alternating signal, expressed as a function of time, can be written as:

$$E_t = E_0 \sin(\omega t); \qquad (24)$$

where E_t – the voltage at time t, E_0 – amplitude of the signal, ω – angular frequency ($\omega = 2\pi f$). Then, the response signal, I_t, can be expressed as:

$$I_t = I_0 \sin(\omega t + \phi); \qquad (25)$$

where I_0 is an amplitude of the current and ϕ is a phase shift. The phase between the voltage and current is shifted due to pseudo linearity of the system, i.e. the current response to a sinusoidal potential will be a sinusoid at the same frequency but shifted in phase.

Thus, the impedance of the system can be expressed by applying the Ohm's law:

$$Z = \frac{E_t}{I_t} = \frac{E_0 \sin(\omega t)}{I_0 \sin(\omega t + \phi)} = Z_0 \frac{\sin(\omega t)}{\sin(\omega t + \phi)}. \qquad (26)$$

In Eq. 26, impedance is expressed in terms of magnitude, Z_0, and a phase shift, ϕ. In order to simplify the later expression (Eq. 26) complex numbers are used as follows:

$$Z = Z' + j\omega Z'' \qquad (27)$$

where $|Z| = E_t/I_t$ and $\tan\phi = Z''/Z'$; j is the complex number.

The system's response is usually analysed by applying the equivalent circuit method [38]. Each process of an electrochemical system is represented by passive electrical circuit elements, such as resistors (R), capacitors (C), and inductors (L). The impedance for these elements can be expressed as follows: $Z_{resistor} = R$; $Z_{capacitor} = 1/j\omega C$; $Z_{inductor} = j\omega L$. In the most cases, the equivalent circuit has two serial (R parallel with C) elements: one represents the bulk and the other is related to the grain boundary of the material.

Electrochemical impedance data, revealing the information of resistance and processes occurring in the material, are often evaluated by plotting the imaginary impedance component (Z'') against the real impedance component (Z') at each excitation frequency, called the Nyquist plot [163]. Fig. 17 represents the typical impedance spectrum for ionic conductivity measurements in solids. RC elements illustrate two different processes, as ionic conductivity of grains and grain boundaries [38]. It should be noted that the frequency in the Nyquist plot does not appear explicitly; however, it is known that it decreases from left to right.
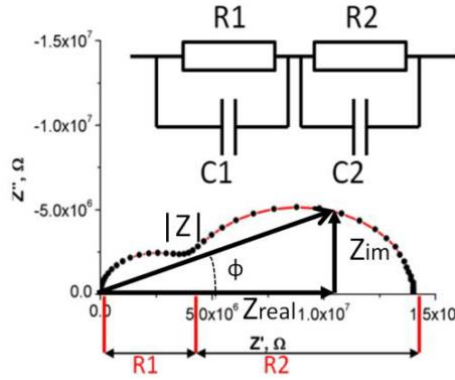
Fig. 17. An example of a Nyquist graph of two RC elements connected in series $(R_1 = 4\ \text{M}\Omega,\ R_2 = 10\ \text{M}\Omega)$ [38]

Mostly, in real electrochemical systems the semicircles from the impedance spectra are depressed and cannot be fitted with such ideal capacitance elements. This can be caused by the distribution of physical properties (e.g. structure resistivity, non-uniform current, dielectric constant, a large amount of surface defects, surface roughness). Therefore, a constant phase element (*CPE*) is used instead of pure capacitance. Then the impedance of CPE can be expressed as:

$$Z_{CPE} = \frac{1}{(j\omega)^{\alpha}Y_0};$$ (28)

where Y_0 is the capacitance (C), α is a fitting parameter, generally 0.9–1.0 ($\alpha = 1$ for an ideal capacitor).

By knowing the resistance (R) value estimated from fitted impedance spectra, the conductivity of a system can be defined by:

$$\sigma = \frac{h}{R \cdot S};$$ (29)

where h is the distance between electrodes and S is the area of the electrodes. The electrodes have to be parallel and congruent in order to avoid non-uniform electrical potential distribution in a sample. The area of electrodes (S) is expressed as $S = \pi d^2/4$ (where d defines the diameter of the electrode) for circular microelectrodes of thin films and circular electrodes of a pellet.

Fig. 18 demonstrates a schematic illustration of the samples prepared for impedance measurements. It should be noted that electrolyte thin films were formed not only on SiO_2/Si substrate, but on Al_2O_3 substrates as well.

(a)
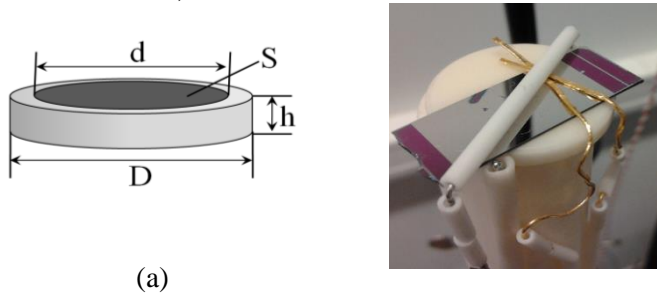
Fig. 18. (a) is a pressed pellet of electrolyte ceramic powder (*d* is a diameter of Pt electrode patterned on both sides of the sample); (b) the fastening of the sample into a sample holder of the Novocontrol Technologies impedance analyser for the measurement

Impedance measurements of GDC (YSZ) ceramics were carried out using an impedance analyser Alpha-AK (Novocontrol Technologies). The synthesized and annealed at 900°C powder were pressed into cylindrical pellets of 13 mm in diameter and approximately 1.5 mm in thickness using a hardened steel die under uniaxial compression (200 MPa) at room temperature. The pellets were annealed for 5 h in air at 1200°C once more with the heating rate of 5°C/min, followed by furnace cooling. The density of the annealed pellets was measured by weight-volume method using the theoretical density of 7.235 g/cm³ [165]. The parallel faces of the sintered pellets were polished using 2 μm polishing paper and cleaned with ethanol in an ultrasonic bath for 5 min, in order to remove any polishing particles, before the application of platinum electrodes. Platinum paste (cond. paste Lot. No. 13032810, Mateck) was coated on both parallel faces of pellets and was left to dry at 300°C for 2 h. Then the ionic conductivity of the pressed pellets was measured in the temperature range of 200 – 800°C, from 1 Hz to 1 MHz frequencies. Fitting and simulations of the impedance spectra were accomplished with *Zview2* software, which is based on the equivalent circuit method.

The plots of σ vs. $1000/T$ were illustrated and the activation energies for conductivity of bulk and grain boundaries (as well as total conductivity) were estimated. The activation energy for conductivity was obtained using an Arrhenius plot and calculated according to the following equation:

$$\sigma_{b,gb} = \sigma_0 exp\frac{-\Delta E_{b,gb}}{kT};$$ (30)

where σ_0 is the pre-exponential factor, k is the Boltzmann's constant ($0.86 \cdot 10^{-4}$ eV K^{-1}), T is the temperature; the activation energies of bulk and grain boundary conductivities, $\Delta E_{b,gb}$, respectively.

In addition, impedance measurements of thin films were performed using an impedance analyser Alpha-A (Novocontrol Technologies, Germany) and Agilent E5062A network analyser. The equipment and experimental details were reported in [166], [167] and [76], respectively.

3. Experimental results and discussion

This Chapter presents the obtained results and discussion. The development of μ-SOFC which operates at reduced temperatures, i.e. up to 600°C, requires high quality, significant ionic conductivity and corresponding density electrolyte thin films. For this purpose, the electron beam evaporation technique (EB-PVD) was applied in this study. The shortcomings of EB-PVD technique related to the deviation of chemical composition in thin films compared to the target material were overcome by applying synthesized materials of variable chemical composition. Easily performed co-precipitation (CP) synthesis and impregnation techniques were

tailored for the synthesis of metal oxide ceramic powder used as a target in the evaporation process. The properties of synthesized electrolyte materials and evaporated thin films were carefully studied. It was noticed that the characterization of ionic conductivity properties of electrolyte thin films by impedance spectroscopy requires more accurate preparation of the samples and properly selected measurement configuration.

In order to extend the lifetime of the μ-SOFC element, appropriate attention was devoted to researching the behaviour of Pt electrode thin films at μ-SOFC operating temperatures in the range of 500–800°C with respect to their porosity, microstructure, electrical properties, etc. The electrodes (positive/negative electrodes) were formed by varying the argon gas pressure in the chamber during the magnetron sputtering process and applying additional thermal processing.

The final step was the design and implementation of μ-SOFC manufacturing process using thin film deposition and microelectromechanical system (MEMS) processing techniques.

3.1. The deposition calibration of EB-PVD technique for the formation of μ-SOFC electrolyte thin films

In this research the e-beam evaporation (EB-PVD) technique was used for the preparation of μ-SOFC electrolyte thin film. The optimal evaporation conditions were determined in order to find the relation between the evaporation time and the thickness of the film. Commercial 8YSZ-45 and GDC20-N ceramic powder with a following composition: yttria-stabilized zirconia containing 8 mol% of Y_2O_3; and 20 mol% $GdO_{1.5}$ doped ceria (which corresponds to ~11.08 mol% of Gd_2O_3) were used as reference materials, clarifying the growth rate of the film and the chemical composition of the evaporated YSZ and GDC thin films. The powder was pressed into pellets of 13 mm in diameter and used as a target in the evaporation process. The evaporation of the films was repeated three times with the same process conditions. The illustrated values (points) in graphs are given as an average of all experiments.

The graphical dependence of the evaporation time vs. the thickness of thin film is represented in Fig. 19. The graphic illustration shows that the film has a linear dependence as a function of evaporation time. The obtained average growth rate was 1.2 and 2 nm/s for YSZ and GDC thin films, respectively.
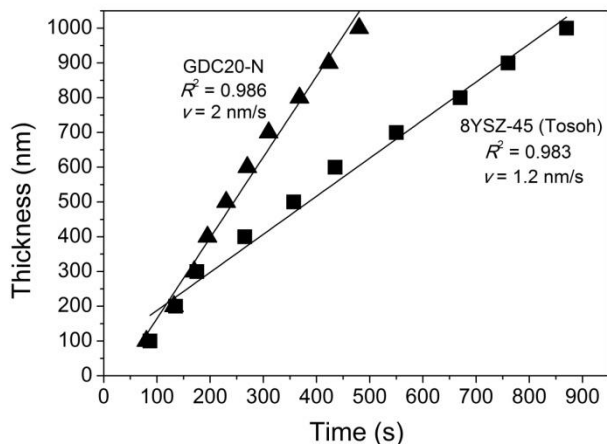
Fig. 19. The growth rate (v) of YSZ and GDC thin films during the EB-PVD process

The electrolyte of μ-SOFC has to maintain important requirements, such as high density and good ionic conductivity [5,16,17,47,93]. These requirements can be achieved by controlling the concentration of impurities in the sample, e.g., mol% of yttria and gadolinia in YSZ and GDC thin films [44], respectively, and by selecting an appropriate method for the deposition of thin film. The optimal chemical composition of elements in the films has to be ensured.

Since the choice of thin film fabrication technique may influence the chemical composition of the film, this research aimed to ascertain this dependence on the thickness of the film (at the same time and evaporation time) using the EP-PVD technique. The chemical composition of the evaporated films according to the thickness of the film was estimated by the EDX measurement.

In order to determine the mole percent of Y_2O_3 via ZrO_2 in YSZ, and Gd_2O_3 via CeO_2 in GDC thin films, we used postulate as follows [17]: first, the sum of mole percent of Y_2O_3 and ZrO_2 as well as Gd_2O_3 and CeO_2 should be one. Second, the portion between mole percent of Y_2O_3 and ZrO_2 as well as Gd_2O_3 and CeO_2 should be same as the portion between half of Y and Zr also Gd and Ce atomic concentration, respectively.

The important observations of the dependence of Y_2O_3 content (mol%) on the thickness of 8YSZ-45 (Tosoh) and molar Gd_2O_3 content on the thickness of GDC20-N thin films are illustrated in Fig. 20 (a) and (b), respectively.

74
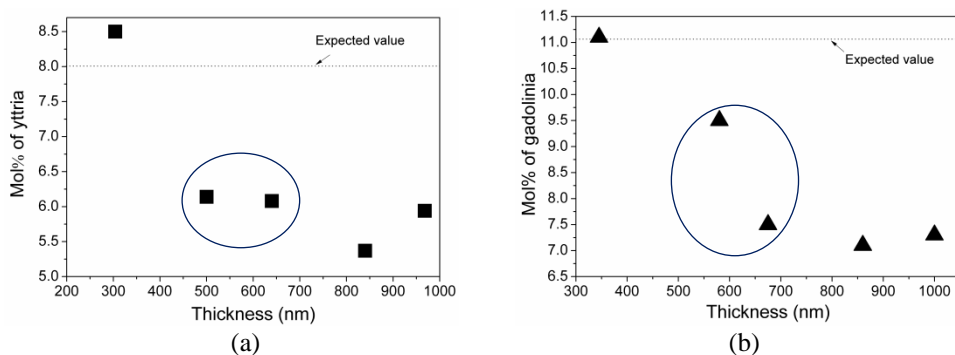
Fig. 20. The molar content of yttria (a) and gadolinia (b) in evaporated YSZ and GDC thin films as a function of thickness

It is evident that the chemical composition of a thin film depends on the thickness (thereby, evaporation time). It was proven that the initial material (which usually is a multinary compound) with the required composition cannot ensure the preferred chemical composition of thin films.

Fig. 20 (a) shows that the molar concentration of Y_2O_3 in the films may differ from the original chemical composition of the ceramics by up to 33%, i.e. ~ 5.4 mol%. The molar concentration of Y_2O_3 in the YSZ films was found to be in the range of 8.5–5.4 mol%. The closest content of Y_2O_3 (8.5 mol%) to the composition of the initial material was obtained for the thin film with a thickness of 300 nm. Meanwhile, the lowest molar content of Y_2O_3, 5.4 mol%, was observed for the thin film with a thickness of ~840 nm; and the value of 6 mol% was obtained by increasing the thickness of the film up to 970 nm.

A similar deviation of the chemical composition was observed in GDC thin films when compared to the YSZ results. The value of 11.1 mol% was found for the film with a thickness of 340 nm. It should be noted that the obtained value corresponds to the initial chemical composition of the target. However, for the production of the μ-SOFC electrolyte, thin films with the thickness of 500–650 nm are usually deposited, thus the change of dopant concentration in this range is the most important. Fig. 20 (b) reveals that in the thickness range of 550–670 nm, the molar content of Gd_2O_3 drastically decreases from 9.5 to 7.5 mol%.

These observations can be related to different evaporation temperatures and rates of Y_2O_3 and ZrO_2 as well as Gd_2O_3 and CeO_2. The evaporation temperatures of yttria and zirconia are 2300 and 2400°C, respectively, while gadolinia and ceria evaporates at 2046 and 1825°C temperature, respectively, with a vacuum pressure of 10^{-2} mbar in the system. In the beginning of evaporation, the concentration of the more volatile element in the vapour is higher; however, by increasing the amount of evaporated material, the less volatile element starts to evaporate more intensively [96]. Certainly, the deviation of chemical composition in the films may be influenced by the low percentage of dopant in the target material.

Thus, in order to guarantee a required elemental composition in the evaporated electrolyte thin films (thickness of ~600 nm), co-precipitation (CP) synthesis method was employed for the synthesis of the target material in this research. The

aim was to synthesize the initial ceramics with the required properties, such as chemical composition, microstructure, and significant ionic conductivity as well as chemical and thermal stability at high temperatures.

3.2. Synthesis and characterization of the electrolyte material and the formation of thin films

This subchapter characterizes various electrolyte materials synthesized using the co-precipitation (CP) synthesis method and incipient wetness (IW) impregnation method. The possibilities of using YSZ and GDC ceramics with different concentrations of dopants as well as CeO_2-YSZ ceramics in the fabrication of μ-SOFC are shown.

3.2.1. Synthesis, sintering and the characterization of YSZ ceramics

This section characterizes the co-precipitated YSZ ceramic powder with a variation in molar contents of Y_2O_3 (5, 8 and 10 mol%). The synthesis route was adjusted by changing the pH value of the solution during the CP synthesis process. The co-precipitated powder was compared to commercial ones. Finally, targets used in the EB-PVD process were produced and thin films were fabricated and analysed.

3.2.1.1. Thermal analysis of the precipitated YSZ ceramic powder

A comparative study on the synthesis of yttria-stabilized zirconia using different synthesis routes is demonstrated in [168].

Thermal decomposition behaviour of the precipitated Y–Zr–oxalate which corresponds to the final composition of $(Y_2O_3)_{0.08}(ZrO_2)_{0.92}$ was investigated by employing simultaneous TG-DSC measurements. The TG-DSC curves of the precipitated Y–Zr oxalate are shown in Fig. 21.
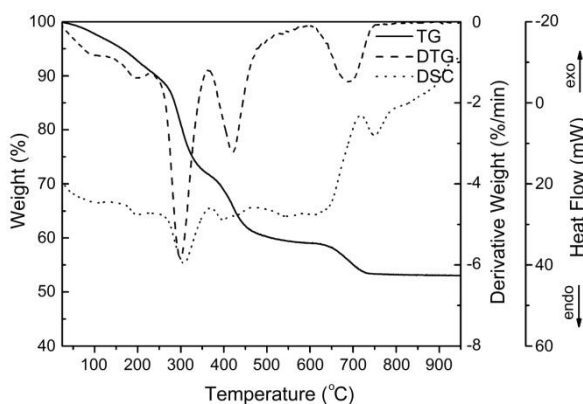
Fig. 21. TG–DSC curves of Y–Zr oxalate precipitate

The thermal decomposition of the Y–Zr oxalate precipitate passes through five stages. Two endothermic peaks in the DSC curve in the range of temperatures 25–230°C are due to the removal of adsorbed and hydrated water. The weight loss of ~19% in temperature interval 230–362°C is attributed to the decomposition of zirconyl oxalate ($ZrOC_2O_4$) to form intermediate carbonate species ($ZrOCO_3$). This

76

is in good agreement with the results published by Drozdz-Ciesla et al. [169]. The fourth weight change in the temperature range 360–490°C is attributed to simultaneous decomposition of the residual $ZrOCO_3$ and $Y_2(C_2O_4)_3$. As a result, amorphous zirconium oxide (ZrO_2), various carbonato-oxalates and oxycarbonates are formed [170,171]. The weak exothermic signal in DSC curve which peaked at 470°C can be ascribed to the amorphous zirconia crystallization stage [172]. The final weight loss of ~6% in the temperature range 600–760°C indicates decomposition of the thermally stable $Y_2O_2CO_3$. The exothermic peak above 600°C in the DSC curve is attributed to amorphous-crystalline phase transition in Y_2O_3. Such exothermic peaks were observed in nearly all rare earth metal oxalates studied by Wendlandt et al. [173]. In conclusion, the TG analysis of the precipitated Y–Zr oxalate reveals that two separate phases are formed in different temperature ranges.

3.2.1.2. Structural and morphological properties of YSZ ceramics

The phase crystallinity and purity of all samples were characterized by means of XRD analysis. The representative XRD patterns of YSZ specimens obtained using the CP method and annealed at 800°C for 5 h in air are shown in Fig. 22.
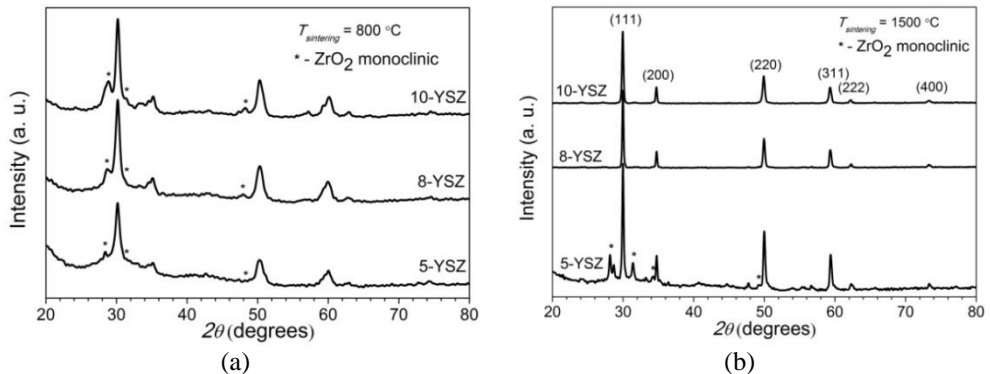
Fig. 22. XRD patterns of 5, 8, and 10-YSZ powder prepared using the CP synthesis route and annealed at (a) 800 and (b) 1500°C, respectively

The formation of two phases attributed to tetragonal zirconia (ICSD#00-078-1808) and monoclinic zirconia (ICSD#00-086 1451) was observed in all samples despite their chemical composition. XRD analysis of the powder revealed that the single-phase cubic zirconia with fluorite-type crystal structure was not obtained at 800°C. Therefore, the samples were annealed at elevated temperatures. It was found that the temperature of 1500°C is necessary to obtain single-phase cubic zirconia of 8 and 10-YSZ (Fig. 22). However, in the 5-YSZ sample, the mixture of cubic and monoclinic zirconia was observed after the same thermal treatment. The narrow reflection peaks of samples annealed at 1500°C suggest a higher degree of crystallinity in comparison with those which were annealed at 800°C.

Based on the obtained XRD results, it is possible to conclude that the phase formation mechanism in the precipitated powder is similar to the traditional solid-

state reaction synthesis route, where much higher temperatures are necessary to obtain the single-phase compound.

The morphology of synthesized YSZ powder samples was examined using scanning electron microscopy (SEM). The SEM micrographs of 8-YSZ sample synthesized by CP method and annealed at 1500°C are shown in Fig. 23 (a). The SEM images clearly demonstrate that powder consists of irregular-shape agglomerates (10–30 µm) covered by smaller particles.

Fig. 23 (b) represents the SEM images of 8-YSZ pellet sintered at 1500°C for 2 h. It is evident that the pressed pellet (Fig. 23 (b)) is composed of smaller (0.2–0.5 µm) and much larger (1–2 µm) grains. The latter tend to aggregate each other to form island-like structures. Numerous interspaces and cracks are observed on the surface, which is suggestive of the poor quality of the ceramic sample.
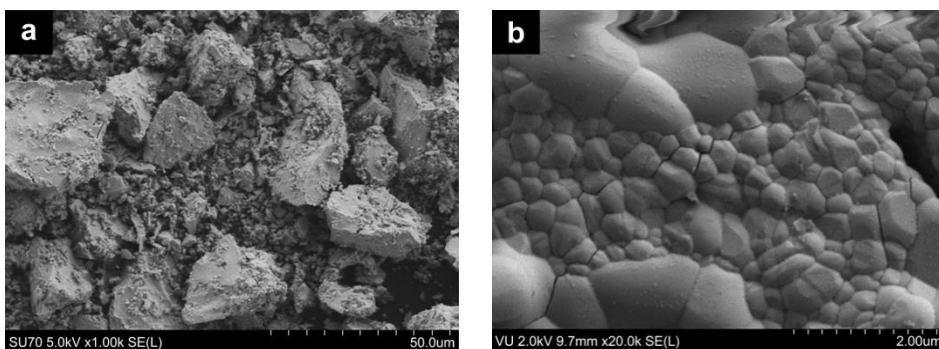
Fig. 23. SEM micrographs of 8-YSZ powder (a) and the pellet pressed from this powder (b) synthesized by a CP synthesis route and sintered at 1500°C

3.2.1.3. Electrical properties

A single large deformed semicircle can be observed in the Nyquist plot for the ceramics sintered from the CP powder (Fig. 24).
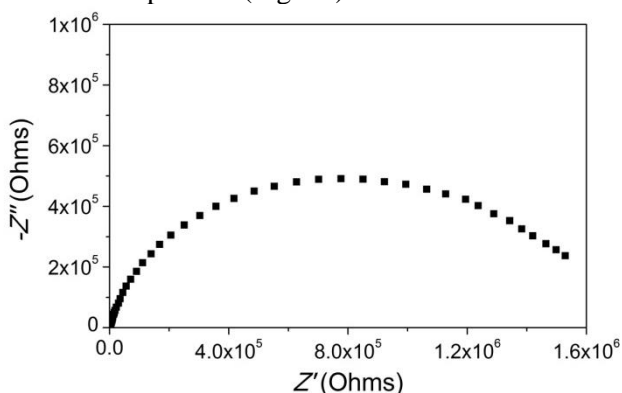
Fig. 24. Nyquist plot of the synthesized 8-YSZ ceramics measured at 500 K

Numerous cracks and a large variety of ceramic grain sizes contribute to the grain boundary resistivity arc. In this case, the poorly conductive ceramics grain

boundaries govern the entire spectrum and the bulk conductivities could not be extracted from the impedance data.

Temperature dependences of the grain boundary conductivities are shown in Fig. 25.
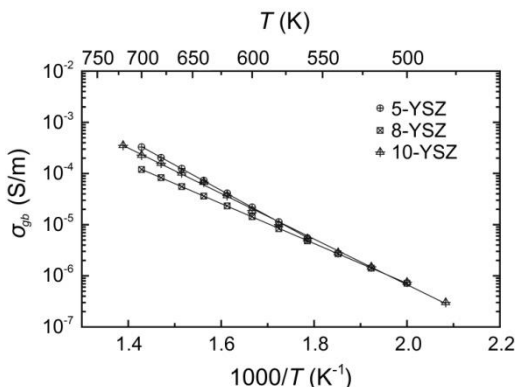
Fig. 25. Temperature dependences of grain boundary conductivities of 5, 8 and 10-YSZ ceramics. Solid lines are the fits in accordance with Arrhenius law

Ceramics synthesized by CP synthesis route and sintered at 1500°C for 2 h revealed relatively low conductivity compared to other studies [69]. The low grain boundary conductivity can be a result of low density of the sintered ceramics. Not only the quality of the ceramics, indicated by σ_{gb}, but also the amount of phase which stabilizes the Y_2O_3 affects the grain boundary conductivity of the ceramics. Activation energies of 5, 8 and 10-YSZ ceramics determined from Arrhenius plots were 1.00, 0.78 and 0.89 eV, respectively. The obtained values are comparable with the values found by other authors [15,174].

3.2.1.4. The influence of pH value of the solution on the properties of YSZ ceramics

Due to the poor quality and uneven distribution of grains of YSZ ceramics, it was aimed to synthesize powder with a homogenous distribution of grains by changing the parameters of the CP synthesis route. As it was discussed in the literature review (subchapter 1.2.1.1), there are many parameters that may be changed in order to reach this goal [69]. On the basis of a review article [69], the morphology of the powder may be affected by changing the pH value of the solution. According to studies carried out by S.K. Tadokoro [175], an attempt to synthesize ceramic powder with improved properties required further μ-SOFC applications by diminishing the pH value of the solution. The pH scale with values of 9, 8, 7, 6.5 and 6 were used in the CP synthesis route. A number of studies has been carried out and it has been observed that the improved properties of electrolyte ceramics were obtained as the pH value of the solution was 6.5. Thus, in this subchapter, the results of a newly synthesized 8-YSZ ceramic powder with the required properties are presented and compared to the properties of commercial powders (8YSZ-45, Tosoh).

The XRD diffraction patterns of the commercial 8YSZ-45 and the precipitated 8YSZ ceramic powder are presented in Fig. 26. Both of these powders are almost identical, although the sintering temperature of the synthesized powder was relatively low (900°C). Moreover, the XRD data clearly indicate the formation of a single cubic-phase structure. The XRD analysis revealed that the powder were precipitated with nano-sized crystallites, i.e. in the range of 6–20 nm, while the commercially available 8YSZ-45 powder was found to have crystallites of 11–31 nm range.
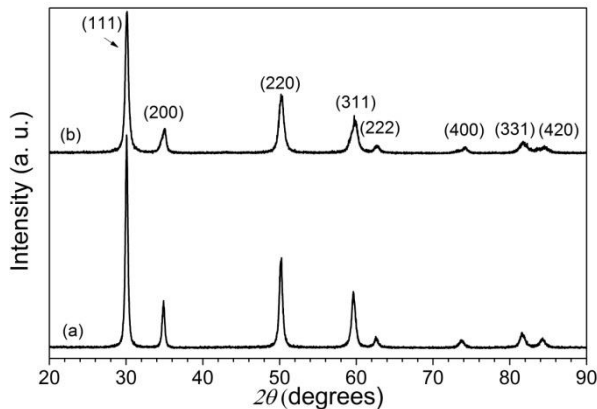
Fig. 26. XRD patterns of (a) 8YSZ-45 and (b) 8-YSZ ceramic powder prepared by CP synthesis route with the reduced pH value (to 6.5) of the solution and sintered at 900°C for 4 h

SEM micrographs of 8YSZ-45 and 8YSZ powder sintered at 900°C for 4 h are illustrated in Fig. 27 (a) and (b), respectively.
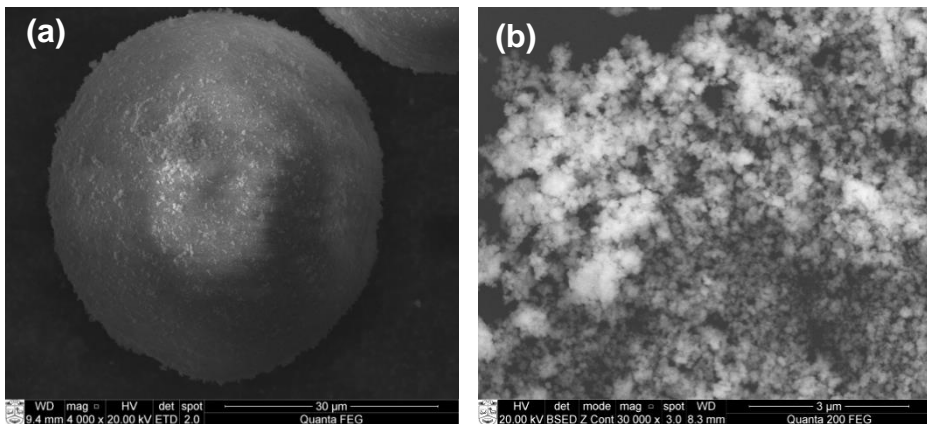
Fig. 27. SEM images of (a) commercially available 8YSZ-45 (Tosoh) and (b) synthesized 8-YSZ ceramic powder sintered at 900°C for 4 h

Fig. 27 (b) shows that the 8-YSZ powder composed of small and fairly uniform particles which form a cloud-like structure after calcination at 900°C for 4 h. The abundance of large particles almost disappears in comparison with the results

obtained when the pH value of the solution was 9 (Fig. 23), while 8YSZ-45 powder reveal ball-shaped particles (Fig. 27 (a)).

SEM results of the cross-section of ceramic pellets pressed from 8YSZ-45 and the synthesized 8-YSZ ceramic powder followed by annealing at 1500°C for 5 h are shown in Fig. 28.
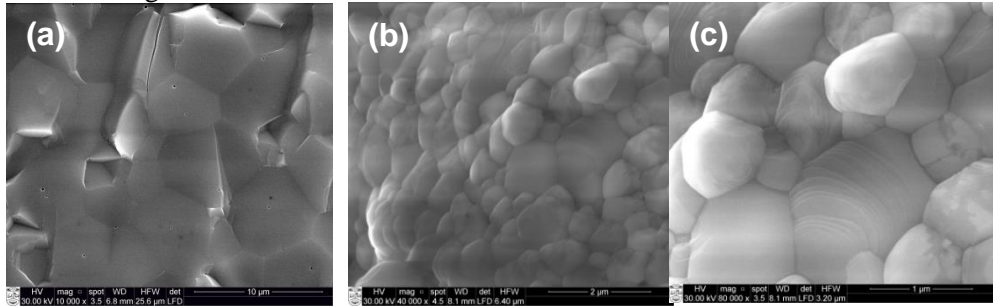
Fig. 28. Cross-sectional views of (a) 8YSZ-45 ceramics, (b) and (c) precipitated 8-YSZ ceramics at different magnifications after annealing at 1500°C for 5 h

Fig. 28 (b) and (c) displays that 8-YSZ ceramics sintered at 1500°C forms a dense microstructure and homogeneous distribution of grains with an average size of 600 nm, as well as a significant growth of grains at high temperature, corresponding to a smaller grain boundary volume. Meanwhile, the average grain size of 8YSZ-45 ceramics cannot be distinguished due to the merge of grains at high temperature. It is known that reduced grain size is an important in order to improve the ionic conductivity of electrolytes, because the grain boundary resistance makes a large contribution to the total ohmic loss at lower operating temperatures [69]. Therefore, the synthesis routes of ultra-fine and nano-sized oxide powder used for μ-SOFC application are of substantial interest [176].

Electrical properties of 8YSZ-45 and 8-YSZ ceramics were also compared. The impedance measurements were performed at a testing temperature range from 200 to 550°C in order to investigate the contribution of the bulk and grain boundary to the total conductivity of the electrolyte, avoiding the overgrowth of grains at elevated temperatures. Fig. 29 shows typical impedance spectra for 8YSZ-45 and the synthesized 8-YSZ ceramics with Pt electrodes measured at 400°C in air.

The first semicircle at high frequencies is related to the intragranular (bulk) properties of cubic stabilized zirconia, and the other, at low frequencies, is related to the blocking of charge carriers caused by the insulating phase within grain boundaries [177]. As can be seen from Fig. 29, grain boundaries influence the ionic conductivity of the synthesized ceramics much more than bulk properties compared to 8YSZ-45. The results obtained by IS measurements correlate well with the microstructure of pellets (Fig. 28).
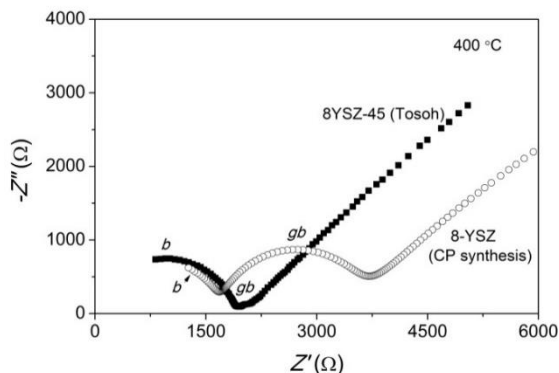
Fig. 29. Nyquist plots of the commercially available (8YSZ-45) and the synthesized (8-YSZ) ceramics measured at 400°C

Fig. 30 shows typical Arrhenius plots and actual ionic conductivity of the commercial and synthesized YSZ electrolytes in the temperature range of 200–550°C, obtained from the total resistance values of the impedance spectra.
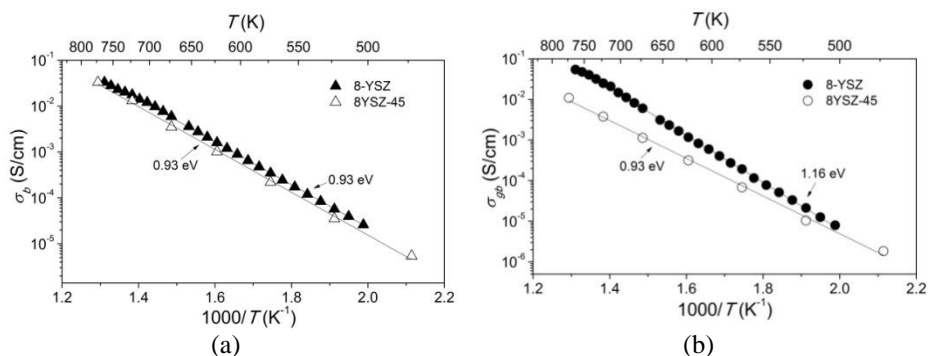

Fig. 30. Temperature dependences of bulk and grain boundary conductivities of 8YSZ-45 and 8-YSZ ceramics. Solid lines are the fits in accordance with Arrhenius law

Fig. 30 shows temperature dependences of 8YSZ-45 and 8YSZ bulk and grain boundary conductivities in the Arrhenius representation. The activation energies of 8-YSZ (co-precipitation) and 8YSZ-45 (Tosoh) ceramics bulk conductivities are the same and equal to 0.93 eV, while, the activation energies of grain boundary conductivity were 1.16 and 0.93 eV, respectively. The measured bulk and grain boundary ionic conductivities of the co-precipitated 8-YSZ were obtained similar or higher than that of 8YSZ-45 (Tosoh) (Fig. 30). It has been found that bulk conductivity is predominantly related to the relative density and is insensitive to the grain size of the electrolyte. Moreover, the grain boundary conductivity is strongly related to both the relative density and grain sizes of the electrolyte. Also the impurity level, which could have been introduced to the electrolyte during the powder synthesis and ceramic sintering processes, has a significant effect on the grain-boundary conductivity.

Summarizing the results, a properly selected pH value of the solution during the CP synthesis route allows to synthesize higher quality YSZ ceramic powder, which has the improved properties necessary for the enhanced operation of the μ-SOFC. It should be noted that 5-YSZ and 10-YSZ ceramic powder were synthesized with a reduced pH value of the solution as well, and the obtained characteristics were very similar to the 8-YSZ ceramic powder.

3.2.2. Formation and characterization of YSZ thin films using the electron beam evaporation technique

Considering the results obtained in subchapter 3.2.1., thin films were deposited using co-precipitated 10-YSZ ceramics as a target in EB-PVD process. SEM micrographs of 8YSZ-45 (Tosoh) and 10-YSZ thin films deposited using the EB-PVD are represented in Fig. 31 and Fig. 32, respectively.
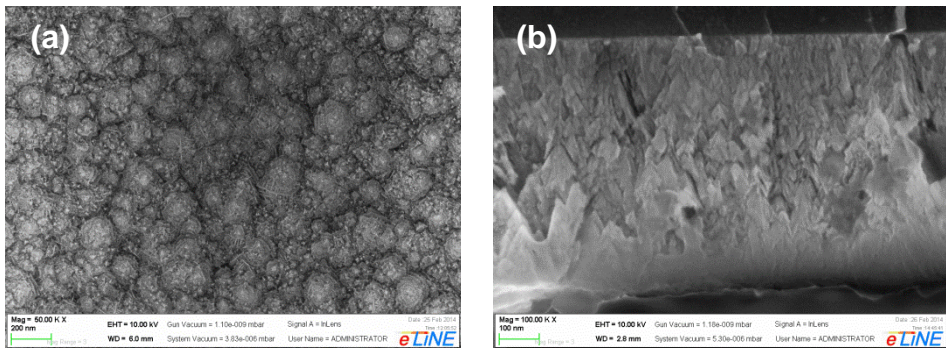
Fig. 31. SEM micrographs of (a) the top view and (b) the cross-section of 8YSZ-45 thin film (thickness of 650 nm)
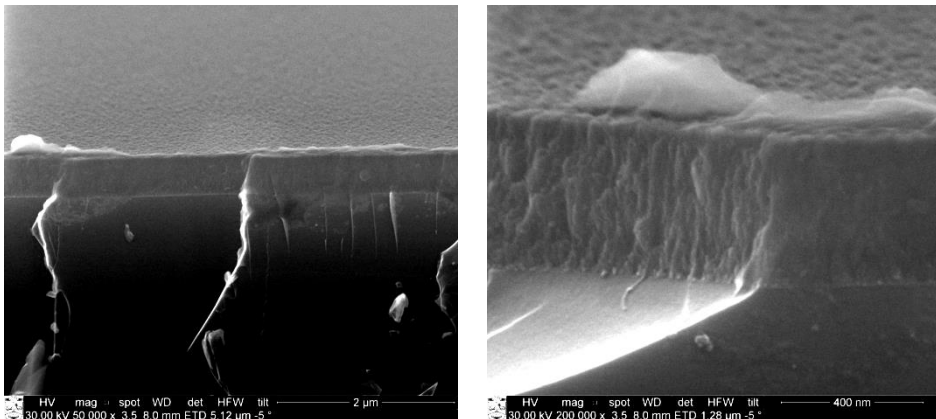
Fig. 32. SEM micrographs of the cross-section of 10-YSZ thin film (thickness of 450 nm) at different magnifications and breaking angles

As it can be seen from Fig. 31 and 32, both 8YSZ-45 and 10-YSZ thin films grow having a columnar structure with an average column width of about 140 nm.

SEM micrographs illustrate that smooth, dense and uniform 10-YSZ thin films with homogeneous distribution of columns are formed.

According to Beckel et al. [47], the evaporation technique is difficult and scarcely used for the formation of electrolyte thin films due to challenges related to the evaporation of complex materials. As a result, up to now, only a few efforts have been devoted to YSZ as well as GDC electrolyte thin film deposition by EB-PVD technique [39,79,90,131,178,179]. However, the authors showed that the properties of evaporated thin films are, in turn, related to the selection of deposition parameters, substrate temperature, etc. and can be easily controlled. 10-YSZ and 8YSZ-45 thin film microstructure observations correlate well with the results obtained by Huang et al. [79], Wu et al. [178], Hartmanova et al. [39], Kundracik [131], etc. Wu et al. [178] indicated the effects of Y_2O_3 content on the growth and structural characteristics of YSZ thin films. The effects of substrate temperatures on the growth characteristics were investigated by Huang et al. [79] and Laukaitis et al [90]. The authors found that even though the substrate was unheated, the orientation peaks of YSZ thin films were formed. In addition, they observed that the strain of YSZ thin films reaches a minimum at 200°C [79]. A comparison of the deposition methods, thin film growth mechanisms (columnar structure) also heat and air conduction mechanisms through the columns were explained by Bernard et al. [180].

XRD patterns of thin films evaporated using commercially available 8YSZ-45 and co-precipitated 10-YSZ targets in EB-PVD process are shown in Fig. 33, which indicates that all diffraction lines of 8YSZ-45 and 10-YSZ thin films correspond to single cubic phase structure. No tetragonal or monoclinic YSZ phases were detected.
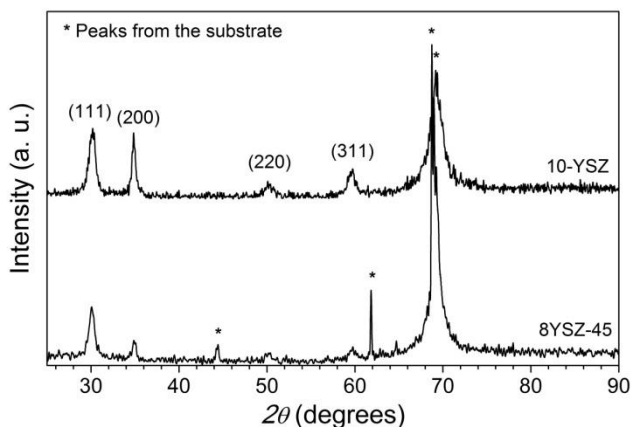
Fig. 33. XRD patterns of 8YSZ-45 and 10-YSZ thin films

In summary, the EB-PVD process is suitable for the formation of dense and high-quality electrolyte thin films using targets of the ceramics synthesized by CP synthesis route with a reduced pH value of the solution. Furthermore, this allows to reduce the sintering temperature of the precursor to 900°C.

3.2.3. Synthesis, sintering and characterization of GDC ceramics

In this section, the co-precipitated GDC ceramic powder with a variation of the molar contents of Gd_2O_3 (from 10 to 20 mol%) is characterized and further used as a target in the EB-PVD process.

3.2.3.1. Thermal analysis of the synthesized GDC ceramic powder

In order to describe the behaviour of the co-precipitated GDC powder at various sintering temperatures, the TG-DTA analysis was performed. Fig. 34 presents TG-DTA plots of as-prepared 10 mol% Gd_2O_3-doped CeO_2 (10-GDC) powder synthesized via the CP synthesis method. The measurements were carried out for all samples and presented the same trends, therefore only 10-GDC results are illustrated.

The thermal decomposition mechanism of 10-GDC powder can be divided into three distinct steps resulting in 44.4% weight loss of the initial compound. The first weight loss (11.6%) starts in the temperature range of 50–200°C in the TG curve which could be attributed to the removal of moisture contained in the sample and the combustion of acetate and oxalate groups. The second step of weight loss of about 2.9% indicates the decomposition of residual organic compounds in the precursor powder between 340°C and 420°C temperatures. The third and the most prominent weight change (~29.6%) is due to the burning of residual carbon and decomposition of inorganic residues in the temperature interval of 420–720°C. Finally, the steady weight loss (~1%) in higher than 700°C temperature is associated with the exclusion of oxygen during the final phase of the crystallization process.
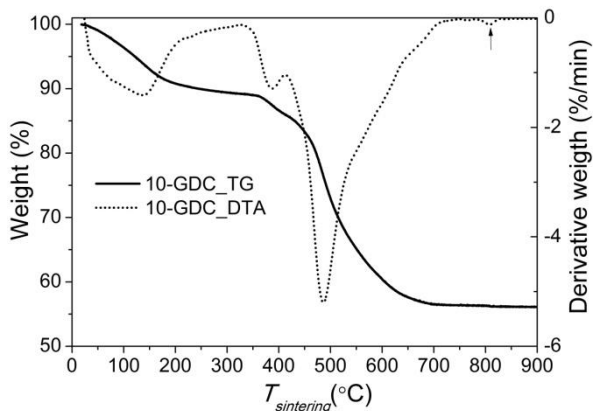
Fig. 34. TG-DTA curves of thermal decomposition of as-prepared 10-GDC powder

According to the obtained results, the mass of the synthesized ceramic powder does not change when temperature exceeds 800°C, which indicates that oxides were completely formed and the material became thermally stable. Moreover, Hsieh et al. [49] reveals that the weight loss of the as-dried precursor obtained by co-precipitation synthesis appears to remain almost constant at relatively low temperatures, i.e. 450°C, which indicates that beyond this temperature, a single phase of $Ce_{0.8}Gd_{0.2}O_{1.9}$ is present, without any impurities, such as hydrate and nitrate

materials. However, Tok et al. [50] mention that the decomposition of the synthesized precursors mainly occurs via three distinct stages and is completed at about 700°C. The differences between the results may be due to diverse parameters of the synthesis, process conditions, etc.

Variation of impurity concentration in the synthesized GDC powder does not have a significant impact on the TG-DTA analysis. Overall, the stabilization of the synthesized GDC ceramic powder structure occurs when the sintering temperature reaches 810°C.

3.2.3.2. Morphological, structural, elemental and compaction analysis of GDC powder

The morphology of the synthesized GDC ceramic powder annealed at 800°C and 900°C temperatures with different molar content of Gd_2O_3, which was investigated using scanning electron microscopy (SEM). The SEM images (Fig. 35) display that GDC powder sintered at 800°C for 2 h formed a sponge-like structure with extremely low-tapped density (Fig. 35 (a)–(c)), while agglomerates (coarse rod-band structure) appears when the sintering temperature reaches 900°C (Fig. 35 (d)–(h)). Zha et al. [181] determined the coarse structure of the GDC powder synthesized using an oxalic acid co-precipitation synthesis and sintering at 750°C for 1 h. However, a foamed structure was observed for the powder synthesized via glycine-nitrate combustion process with the sintering at 600°C for 2 h. The authors mentioned that foamed structures can be used for the preparation of anode/cathode electrodes after additional processing, i.e. metallic-ion impregnation.

Fig. 35 (d)–(h) shows that mainly rods which consist of smaller irregular-shape particles (this is inherent for the co-precipitation synthesis method) were formed. These agglomerates (~400 nm in width) have angular form with fragments and protrusions. Hence, the sample pressed of such as-synthesized and not shredded powder has a relatively low density. Therefore, further powder manufacturing is needed. The structure and properties of the obtained sediment during synthesis process depend on numerous deposition conditions; however, the particles aggregate in any case but the shape, size, density and endurance of aggregates can be different. An aggregate size is almost independent of the annealing temperature; however, the size of aggregates depends on the oxalate precipitation temperature and duration of milling.

XRD patterns of co-precipitated GDC ceramic powder with various molar content of Gd_2O_3 sintered at 900°C are presented in Fig. 36, while Fig. 37 illustrates the behaviour of 10-GDC ceramic powder in the temperature range of 700–1300°C.
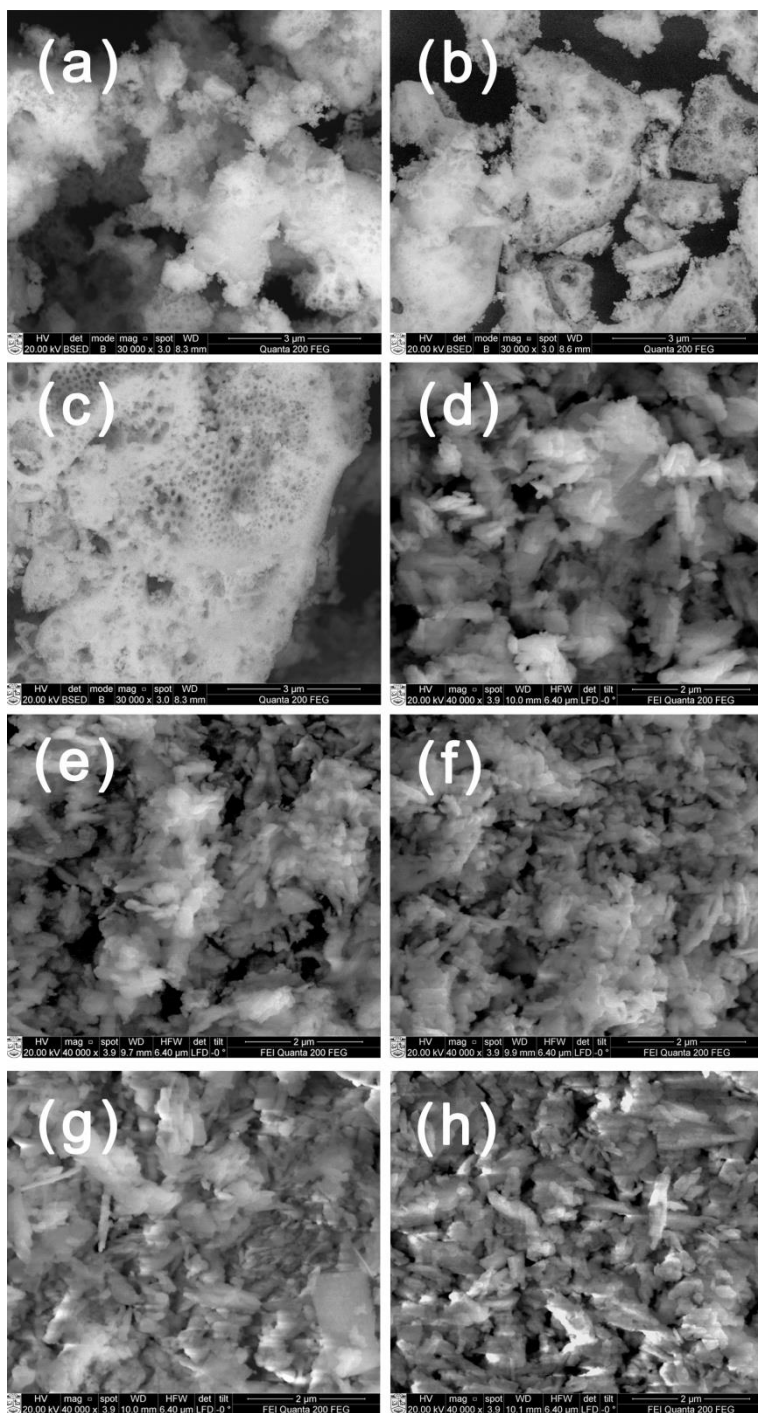
Fig. 35. The SEM micrographs of 10-GDC (a), 15-GDC (b) and 20-GDC (c) ceramic powder sintered at 800°C for 2 h; (d) is 10-GDC, (e) is 12-GDC, (f) is 15-GDC, (g) is 18 GDC and (h) is 20-GDC ceramic powder sintered at 900°C for 2 h
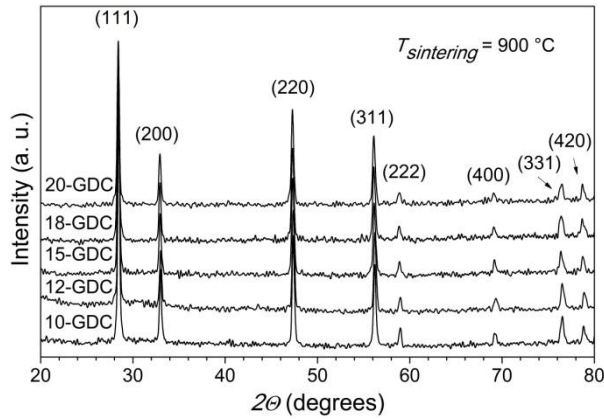
Fig. 36. XRD patterns of 10-GDC, 12-GDC, 15-GDC, 18-GDC and 20-GDC ceramic powder sintered at 900°C
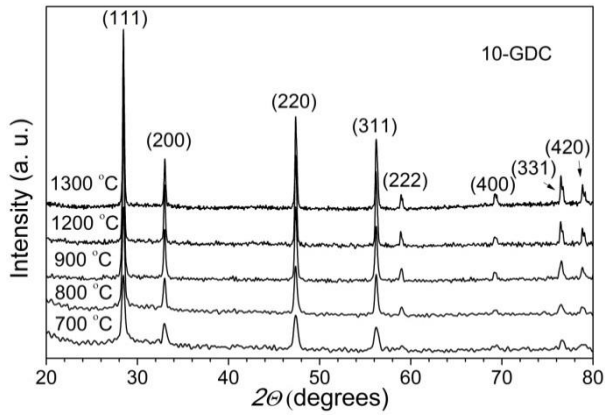
Fig. 37. XRD patterns of 10-GDC ceramic powder sintered in the temperature range of 700–1300°C

All positions of diffraction peaks of GDC powder sintered in the temperature range of 700–1300°C (e.g. 10-GDC, Fig. 37) match the standard XRD data (PDF-4 database: 011-7336, 006-3415, 013-6571). It can be stated that GDC ceramic powder with variable amounts of Gd_2O_3 have a cubic fluorite-type crystalline lattice (spatial symmetry group Fm$\bar{3}$m) with dominating (1 1 1) crystallographic plane. The crystalline structure of $Ce_xGd_{1-x}O_{2-x/2}$ remains the same when $0 < x < 0.5$ [51][182].

Important changes in precursor material can be described by the changes in lattice parameter. Thus, the crystalline lattice parameters of GDC ceramic powder with various molar contents of Gd_2O_3 were calculated according to the equation: $a = d\sqrt{h^2 + k^2 + l^2}$, where d is an interplanar distance; h, k, l are indices of crystallographic plane (in calculations (1 1 1)). The obtained results are demonstrated in Fig. 38.
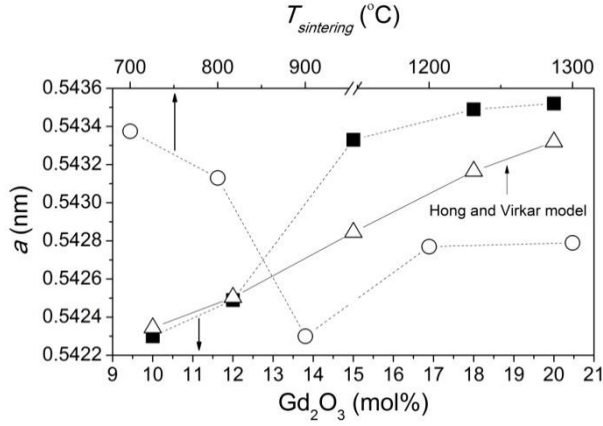
Fig. 38. The dependence of GDC lattice parameter on the Gd$_2$O$_3$ molar content (filled symbols; $T_{sintering}$ = 900°C) and sintering temperature (transparent circles; the sample of 10-GDC); empty triangles indicate Hong and Virkar's model [183]

It was found that the changes in the GDC lattice parameter depend on the amount of inserted Gd$_2$O$_3$ and the \sintering temperature (see Fig. 38). It is known that additives, such as Gd^{3+}, Sm^{3+}, Y^{3+}, etc. with the main oxide (CeO$_2$) create a solid solution [55,165]. Radii of ions and cations of the main oxide and the embedded additive never match by size. Therefore, after the formation of solid solutions, changes in lattice parameters can be observed. Stoichiometric CeO$_2$ crystallizes in the face-centered cubic fluorite-type structure with a lattice parameter of 0.5411 nm, expanding upon doping with gadolinium [63,184]. Due to the fact that the ionic radius of the inserted gadolinium cation Gd^{3+} is larger than the ionic radius of the matrix cation Ce^{4+}, i.e. r_{Gd}^{3+} = 0.1053 nm and r_{Ce}^{4+} = 0.097 nm [165], respectively, the lattice constant a increases with increasing the molar content of Gd$_2$O$_3$ in the ceramic powder. In addition, the growth of the lattice parameter with gadolinia addition is a proof to the incorporation of gadolinium ions in the lattice.

For the calculation of the theoretical lattice parameter of MO$_{1.5}$-CeO$_2$ solid solutions, Hong and Virkar [183] derived an expression:

$$a = \frac{4}{\sqrt{3}}\{x_d r_d + (1 - x_d)r_{Ce} + (1 - 0.25x_d)r_O + (0.25x_d r_{Vo})\}k; \tag{31}$$

where a is the lattice parameter in nm, x_d is the fraction of dopant, r_d is the ionic radius of dopant, r_{Ce} is the radius of the cerium ion, r_O is the ionic radius of oxygen, r_{VO} is the oxygen vacancy, and k is the multiplication factor equal to 5.411/5.427 = 0.9971.

The dependence of an experimentally obtained lattice parameter on the molar content of Gd$_2$O$_3$ was compared with the values of Hong and Virkar's model (Fig. 38). The obtained dependency fits well with the model only at low molar content of Gd$_2$O$_3$, i.e. up to 12 mol%. Further values correlate well with the dependence obtained by Hennings and Reimert [183]. The authors determined the existence of segregated gadolinia phase for the samples with x_{Gd} > 0.3, and explained this

observation as a growth of the cubic gadolinium phase as a thin layer on top of the ceria lattice [183].

Fig. 38 indicates that after annealing the electrolyte powder in the temperature range of 700–900°C, the lattice parameter, a, decreases, while when the annealing temperature increases up to 900°C, a starts to increase. This can be related to incomplete formation of oxides and insufficient sintering temperature. Overall, according to the TG-DTA, SEM and XRD results, 900°C temperature was chosen in order to ensure the full formation of cubic fluorite-type crystalline lattice.

The crystallite sizes of the sintered GDC ceramic powder were calculated with the Scherer equation [45]. According to the obtained results, crystallite sizes of various concentration GDC powder annealed at the same temperature were nearly identical and equal to the average of 31, 39 and 41 nm after sintering at 900, 1200 and 1300°C temperature, respectively. Li et al. [165] mention that doping with both Gd^{3+} and Sm^{3+} effectively suppresses the grain growth of the CeO_2 ceramic during the sintering. However, crystallite sizes increase with the increasing sintering temperature. The sintering of the ceramics is greatly dependent on the diffusion processes that combine distinct powdered grains into one cohesive material. As a result of crystallite size increase, the well-defined peak intensity increases and the broadening decreases, which shows a higher degree of crystallinity in the material.

Elemental analysis and compaction of the sintered GDC powder were also assessed. The molar contents of gadolinia in GDC ceramic powder were measured by ICP-OES and SEM/EDX analysis (Table 9). Results indicate that the chemical composition of materials is fully controlled by the composition of the synthesis solution. Moreover, the properties of ceramics may be influenced by the compaction of the powder during the sintering process. Therefore, such analysis was performed. The results are summarized in Table 9.

Table 9. A summary of the elemental analysis results and some physical properties of the GDC powder sintered at 900°C

Notation	Gd content in GDC	Gd content in GDC from ICP-OES	Gd content in GDC from EDS	S_{BET} (m²/g)	D (nm)	d_{th} (g/cm³)	D_{BET} (nm)	ϕ
10-GDC	0.180	0.181	0.161	11.8	32.6	7.235	70.28	0.464
12-GDC	0.210	0.205	0.197	11.5	30.1	7.238	72.08	0.418
15-GDC	0.260	0.256	0.251	10.18	32.7	7.244	81.37	0.402
18-GDC	0.310	0.304	0.284	9.23	30.0	7.249	89.67	0.335
20-GDC	0.330	0.327	0.314	7.66	31.1	7.251	108.02	0.288

The elemental analysis of the synthesized powder was estimated using two different methods in order to achieve more reliable results. As can be seen from Table 9, the values of Gd content in GDC ceramic powder are lower on average by about 5.5% using EDX analysis as compared to ICP-OES.

Bulk surface area of powder calcined at 900°C was measured by Brunauer-Emmett-Teller (BET) surface area analysis (Sorptometer KELVIN 1042), after

properly degassing the powder samples at 200°C for 2 h. The BET surface area and the equivalent particle size can be correlated by the following equation [165]:

$$D_{BET} = \frac{6 \times 10^3}{d_{th} S_{BET}};$$ (32)

where D_{BET} (nm) is the average particle size, S_{BET} the specific surface area expressed in m^2/g, and d_{th} is the theoretical density of the solid solution oxide (g/cm^3); it was calculated according to the following equation considering that Gd^{3+} cations occupy the Ce^{4+} sites to form a solid solution of Ce$_{1-x}$Gd$_x$O$_{2-x/2}$:

$$d_{th} = \frac{4[(1-x)M_{Ce} + xM_{Gd} + (2-x/2)M_O]}{a^3 N_A};$$ (33)

where x is the dopant concentration (0.18, 0.21, 0.26, 0.31 and 0.33 in this work), N_A is the Avogadro constant, M is the atomic weight, and a is the lattice constant of the solid solution.

In addition, a factor $\phi = S_{BET}/S_{XRD}$ was defined to probe the aggregation extent of the particles, where S_{BET} is the specific surface area determined via BET analysis and S_{XRD} is calculated according to Eq. (33) using the average crystallite size determined via XRD [165].

The obtained results are in a good agreement with the observations from the SEM analysis (Fig. 35) of co-precipitated powder. The obtained value of the ϕ factor for 10-GDC powder, 0.464, is comparable to the value of 0.55 obtained by Ji-Guang Li et al. [165]. The authors also mentioned that if the factor ϕ is lower than 1, the crystallites of synthesized powder are hard-aggregated, i.e. each particle is not a single crystallite, because BET detects particles while XRD detects crystallites. Moreover, they showed that the ϕ factor decreases with the increase of annealing temperature of GDC powder. According to our results, it is evident that ϕ factor decreases with the increase of the molar content of Gd$_2$O$_3$ in GDC ceramic powder (Table 9).

3.2.3.3. Electrical properties of GDC ceramics

In order to characterize the ionic conductivity of GDC ceramics, the density of pellets as well as the distribution of grains were evaluated. Fig. 39 represents the SEM images of 10-GDC and 20-GDC pellets sintered at 1200°C temperature for 5 h.
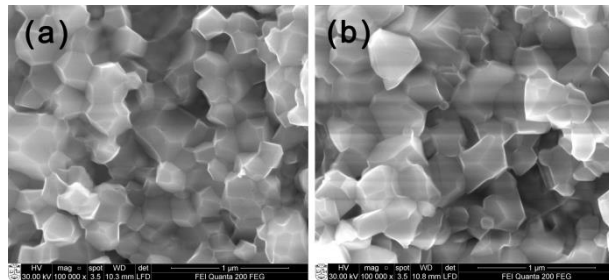
Fig. 39. A cross-sectional view of 10-GDC (a) and 20-GDC (b) ceramics sintered at 1200°C

The obtained SEM images clearly show that the average grain sizes of 10-GDC and 20-GDC ceramics sintered at the same temperature (1200°C) were about 222 and 317 nm, respectively (Fig. 39). The same tendency was observed for the other concentrations of GDC ceramics. The rate and degree of sintering depends on the sintering temperature and time, dispersivity of the particles as well as the diffusion coefficient. Moreover, the sintering rate is inversely proportional to the particle diameter. Also, the diffusion coefficient is directly proportional to the amount of crystalline lattice defects. It should be noted that the sintering quality of ceramics is the most important factor for the analysis of ionic conductivity using impedance spectroscopy. The density of the measured ceramics has to be over 96% of theoretical density. The porosity of the system can be decreased from 30–50% to a few percent when fine-dispersive powders are sintered and individual grains grow together.

The task of estimating the density of GDC ceramics from SEM images has proven to be rather difficult, whereas the cross-section surface of the pellet was not further processed in this study, i.e. special methods have not been applied for the polishing. Visible cavities were mainly due to the surface roughness after breaking the samples. However, the established density of the synthesized GDC ceramics used in the IS measurements were in the range of 93–95%. Meanhile Arabaci [66] reported that $Ce_{0.9}Gd_{0.1}O_{1.95}$ powder prepared with the Pechini method and sintered at 1200 and 1400°C for 6 h presented 87 and 98% of theoretical density, respectively.

IS measurements were carried out for GDC ceramics with various contents of Gd_2O_3, i.e. 10, 12, 15, 18, 20 mol% of Gd_2O_3, with patterned Pt electrodes in the temperature range of 200–800°C. Such temperatures were chosen, as it is intended to investigate the solid oxide fuel ceramics (electrolytes) with a relatively low operating temperature of ~600°C. The possibility to separate different processes in the electrolyte is feasible after measuring complex resistance over a wide frequency range of the electric field. Fig. 40 depicts typical impedance spectra for different concentration GDC ceramics measured at 400°C temperature.

The capacitance is related to different processes taking place in ionic ceramics. The high-frequency semicircle in the impedance spectra is attributed to the oxygen ion relaxation in grains, the medium-frequency semicircle is the ionic migration in grain boundaries and the low-frequency semicircle is the electrode polarization (frequencies increase from right to left in spectra). Therefore, the capacitance was calculated according to the formula: $C = \tau/R = 1/\omega \cdot R = 1/2\pi f \cdot R$, where τ is relaxation time, which is inversely proportional to the angular frequency, ω, f is frequency at the top of semicircle, R is real part impedance.
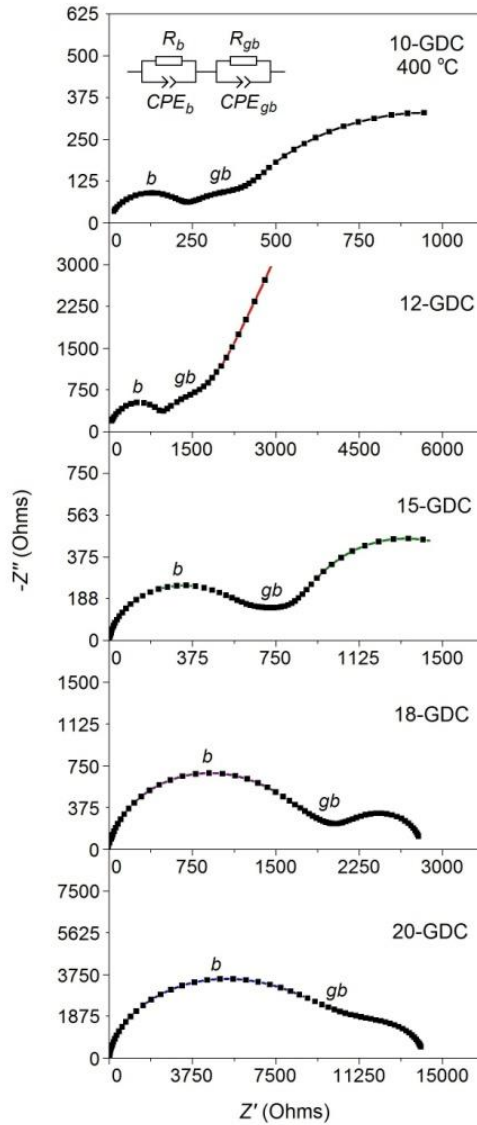
Fig. 40. Nyquist plots of different concentration GDC pellets with Pt electrodes measured at 400°C

Pe'rez-Coll found that for GDC ceramics the capacitance associated with a semicircle of higher frequencies is equal to 1.1 pF and this semicircle characterizes the properties of ceramics bulk; the semicircle in lower frequencies corresponds to the capacitance of 10 nF which is typical for grain boundaries [185]. The value of capacitance associated with electrode polarization is usually several orders of magnitude greater. The experimentally determined values of capacities, which are close to the theoretical ones, are presented in Table 10.

93

Table 10. The capacitance values related to the bulk and grain boundary semicircles of GDC ceramics

	C_b (F)	C_{gb} (F)
10-GDC	$5.0 \cdot 10^{-12}$	$5.4 \cdot 10^{-10}$
12-GDC	$2.6 \cdot 10^{-12}$	$3.4 \cdot 10^{-10}$
15-GDC	$6.1 \cdot 10^{-12}$	$6.2 \cdot 10^{-10}$
18-GDC	$5.6 \cdot 10^{-12}$	$7.3 \cdot 10^{-10}$
20-GDC	$6.1 \cdot 10^{-12}$	$3.8 \cdot 10^{-10}$
The literature values [185]	$1.1 \cdot 10^{-12}$	$1.0 \cdot 10^{-10}$

Fig. 40 shows that the semicircle determined by grain boundaries resistance is relatively higher for the GDC ceramics with low concentration of gadolinia (10-GDC), which means that the grain boundary blocking effect influences the total conductivity of the electrolyte which can be explained by the formation of space charge layers [48,97]. However, the space charge potential decreases with increasing modifying additives, thus the resistance of grain boundaries significantly decreases as a result of the increase of Gd amount (Fig. 40). When the concentration of Gd_2O_3 is close to 20 mol%, the grain boundaries resistance becomes very low and this causes difficulties in distinguishing it from the bulk resistance. Another important outcome is that the higher amount of Gd additives causes higher total resistance of GDC ceramics. It can be concluded that the conductivity of GDC ceramics highly depends on the amount of Gd_2O_3.

Temperature dependences of the bulk, grain boundary and total conductivities ($\sigma_{total} = h/R_{total} \cdot S$, where the distance between the electrodes, h; total resistance, R_{total}; electrode area of pellets, S) of GDC ceramics with different concentration of Gd_2O_3, as measured from impedance spectra, are presented in Fig. 41, (a)–(c).

All temperature dependences of the ionic conductivity follow an Arrhenius-type relation [186]. However, it can be seen that there is a break in the slopes resulting in two different activation energies in the low (200–450°C) and high (450–800°C) temperature regions. According to Anantharaman and Bauri [186], different temperature zones of conductivity in an ionic conductor can be found based on the interaction between defect species and their thermodynamics. At lower temperatures the concentration of charge carrying defects is dictated by the coulombic interaction and the thermodynamic equilibrium between oppositely charged defect species, whereas intrinsic defects dominate at higher temperatures [186]. Moreover, different temperature regimes of conductivity in GDC ceramics may be due to redox reactions occurring in the ceria lattice followed by the formation of polarons [186,187]. Hence, the breaks (Fig. 41 (a)–(c)) obtained in this research show different ionic conduction mechanisms in co-precipitated GDC ceramics. Fig. 41 (a)–(c) demonstrates that the slope changes toward lower activation energy in the high temperature region, which contradicts the results obtained by Anantharaman and Bauri [186]. It should be noted that low and high temperature ranges vary and depend on the data obtained by different authors, such as Hsieh et al. [49], who distinguished low and high temperatures in the ranges of 300–573°C and 573–800 °C, respectively, whereas Muralidharan, et al. [188] and Zha, et al. [63] mentioned breaks occurring below and above 400°C and 650°C temperatures, respectively.
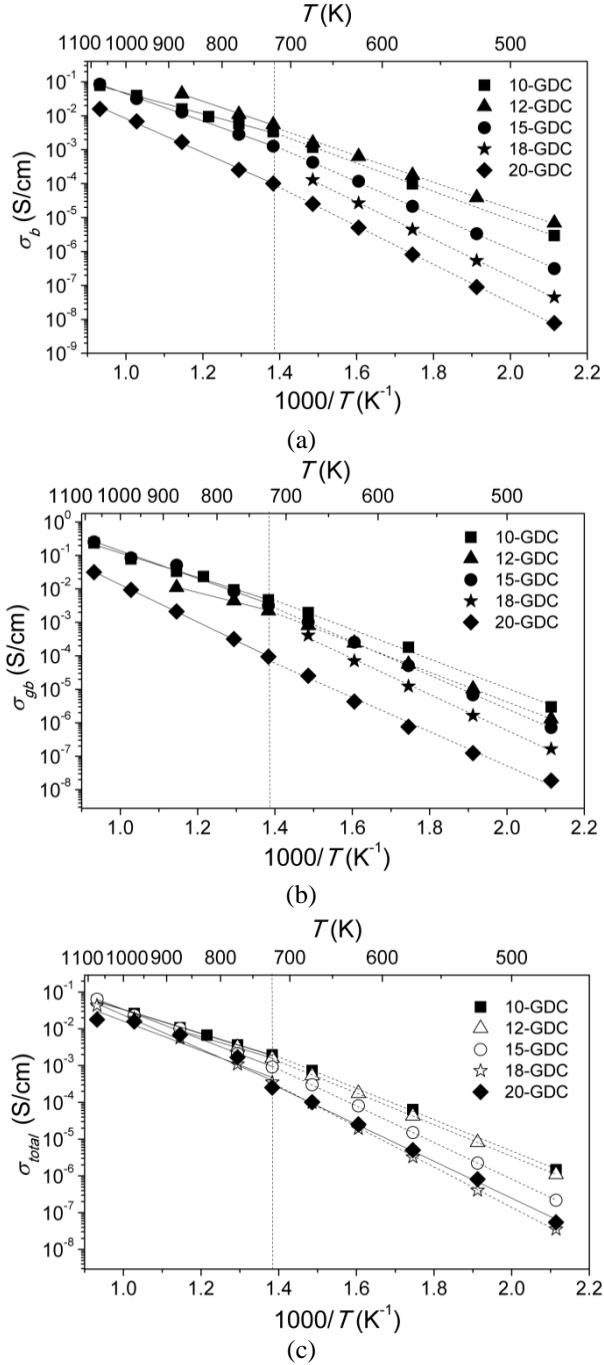
Fig. 41. Temperature dependences of (a) the bulk (*b*), (b) the grain boundary (*gb*), and (c) the total conductivities of GDC ceramics

The activation energies determined from the Arrhenius plots as a function of the Gd_2O_3 molar content in GDC ceramics are summarized in Table 11.

Table 11. The bulk (ΔE_b), grain boundary (ΔE_{gb}) and total (ΔE_{total}) activation energies of GDC ceramics at low temperature (LT) and high temperature (HT) ranges

Ceramics	ΔE_b (eV)		ΔE_{gb} (eV)		ΔE_{total} (eV)	
	LT	HT	LT	HT	LT	HT
10-GDC	0.83	0.61	0.88	0.73	0.85	0.65
12-GDC	0.78	0.77	0.89	0.58	0.86	0.63
15-GDC	0.99	0.80	1.00	0.82	0.99	0.81
18-GDC	1.10	-	1.07	-	1.09	0.93
20-GDC	1.13	1.00	1.02	1.12	1.01	0.80

It was observed that the total conductivity of an electrolyte decreases (Fig. 41) and the activation energy increases (Table 11) as the molar content of Gd_2O_3 in GDC ceramics increases. A comparable tendency was maintained in terms of bulk and grain boundary conductivities. The maximum ionic conductivity of co-precipitated ceramics, which is comparable with the results of other studies, was measured for 10-GDC ceramics at 600°C with 0.011 S/cm. Moreover, its total activation energies at LT and HT regions were one of the lowest, i.e. 0.85 and 0.65 eV. Due to a very low difference on the chemical composition, the values of conductivity and activation energy for 12-GDC ceramics were very similar to 10-GDC. Faruk Öksüzömer et al. [45] reported a 0.0211 and 0.0201 S/cm ionic conductivity at 800°C for $Gd_{0.1}Ce_{0.9}O_{1.95}$ and $Gd_{0.2}Ce_{0.8}O_{1.9}$ ceramics, respectively, synthesized via CP synthesis from acetates using triethylene glycol as a solvent and reducing agent. Also, the authors separated LT and HT regions with total activation energy values of 0.78 and 0.53 eV as well as 0.89 and 0.63 eV for $Gd_{0.1}Ce_{0.9}O_{1.95}$ and $Gd_{0.2}Ce_{0.8}O_{1.9}$, respectively. Meanwhile, Arabaci [66] obtained 0.0325 S/cm ionic conductivity at 500°C for the samples sintered at 1400°C; however the scientist used a higher activation energy, i.e. 0.89 eV.

The mismatch between the results of other authors can be caused by the purity of initial materials, different manufacturing processes, the synthesis proceeding, resulting in differences in microstructure, formation of amorphous glassy phase in grain boundaries due to impurities, etc.

3.2.4. Formation and characterization of GDC thin films by electron beam evaporation technique

The GDC ceramics obtained with the co-precipitation synthesis method was successfully applied for the evaporation of GDC electrolyte thin films on Si(100) substrate by EB-PVD technique. It was aimed to assess the molar content of Gd_2O_3 in thin films depending on the target composition. The obtained results are summarized in Table 12.

Table 12. The composition of evaporated 10, 15 and 20-GDC thin films obtained from XPS and ICP-OES measurements

Notation	Gd content in GDC powder from ICP-OES	Gd content in thin film from XPS	Gd content in thin film from ICP-OES	The molar content of Gd_2O_3 in thin film (mol%)	Decrease of the molar content of Gd_2O_3 in thin film (%)
10-GDC	0.181	0.131	0.133	6.9	31.0
15-GDC	0.256	0.199	0.212	11.3	24.7
20-GDC	0.327	0.261	0.265	14.4	28.0

The obtained results (Table 12) prove that the molar content of Gd_2O_3 in the deposited thin films decreased on average by about 28% compared to the composition of target material used in the EB-PVD process. The established decrease of the molar content of Gd_2O_3 in thin films is irrespective of the initial material composition. The co-precipitated 15-GDC ceramics used as a target in the evaporation process ensures the formation of 10-GDC thin film, which is believed to have the highest ionic conductivity [44].

The SEM micrographs of the cross-section of 10-GDC thin film at different magnifications are illustrated in Fig. 42. In comparison with YSZ thin film, GDC film reveals an isotropic microstructure.
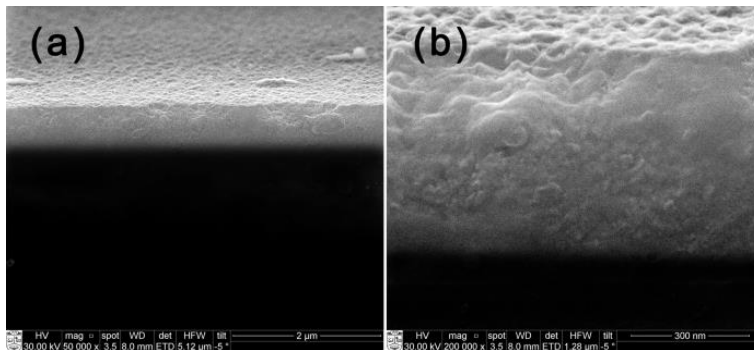
Fig. 42. A cross-sectional view of 10-GDC thin film obtained at 50000 (a) and 200000 (b) magnifications

The deposited 10, 15 and 20-GDC thin films were characterized using X-ray diffraction analysis (see Fig. 43). It is evident that GDC electrolyte thin films were highly textured in (1 1 1) crystallographic orientation and reveal a cubic-phase structure irrespective of the composition of initial material.
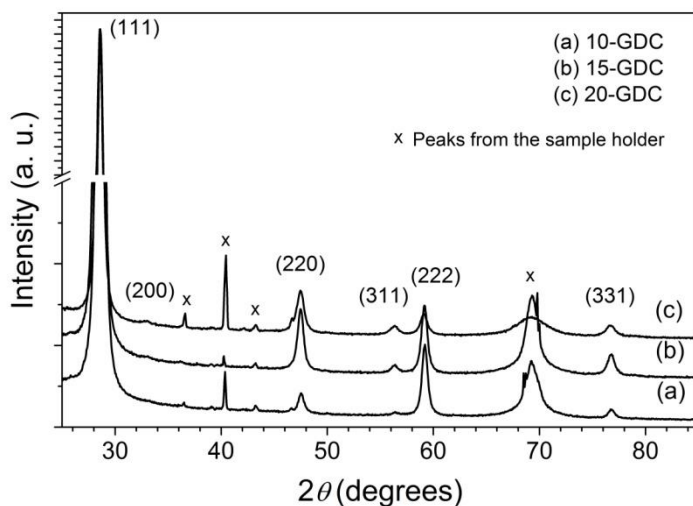
Fig. 43. X-ray diffraction patterns of evaporated 10, 15 and 20-GDC thin films

In summary, the evaporation process is complex and depends on many factors, therefore the formation of homogenous thin films with the required composition often is complicated and possible only under certain conditions or by adjusting a specific composition of the source material.

3.2.5. Formation and characterization of CeO$_2$-YSZ ceramics

3.2.5.1. Characterization of the synthesis and calcination products

The phase crystallinity and purity of the CeO$_2$-YSZ ceramics were characterized by means of XRD analysis (Fig. 44).
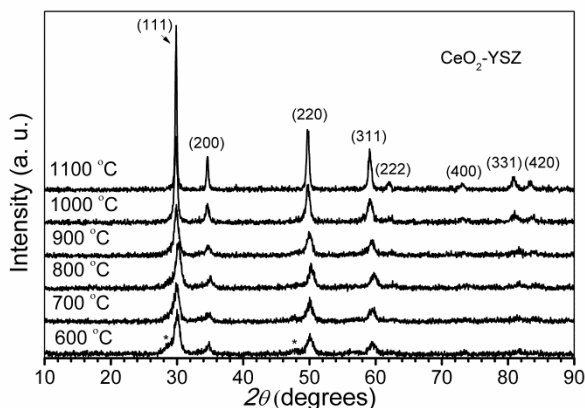
Fig. 44. XRD patterns of CeO$_2$-YSZ ceramic powder sintered in the temperature range of 600–1100°C

The representative XRD patterns of CeO$_2$-YSZ confirm the fluorite-type cubic structure with a very small degree of tetragonalization (marked with an asterisk in Fig. 44). A higher degree of crystallinity was determined with an increase of the

sintering temperature. Samples sintered at higher than 700°C exhibited only a fluorite-structure cubic phase.

3.2.5.2. The electrical properties of CeO₂-YSZ ceramics

The IS measurements of the synthesized CeO₂-YSZ ceramics were performed in order to determine the ionic conductivity contribution of the bulk and grain boundary. Fig. 45 displays an example of the comparative impedance ($\tilde{Z} = Z' - iZ''$) spectra of CeO₂-YSZ ceramics (the annealing temperatures of pellets were 1000 and 1500°C) measured by 2-electrode method. The impedance spectra shows the measurement results at 400°C under air atmosphere. Two relaxation processes were observed in the impedance spectra. Fig. 45 illustrates that CeO₂-YSZ ceramics consists of two components, i.e. bulk conductivity and conductivity of grain boundaries. The influence of external electrode/material interfaces on the measurement results was also observed, particularly for the ceramics annealed at 1500°C for 3 h.
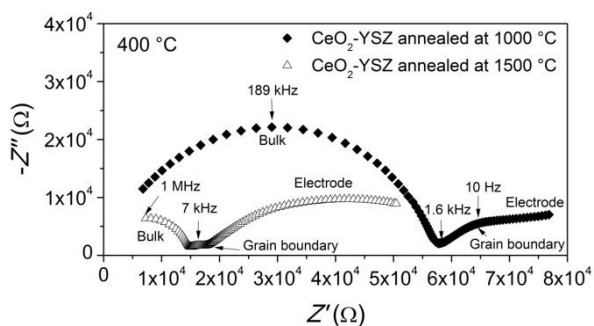
Fig. 45. Nyquist plots of impedance spectra obtained at 400°C for CeO₂-YSZ ceramics annealed at 1000 and 1500°C

It is indeed well-known that the grain boundary resistance arc of the Nyquist plot is associated with numerous cracks and wide distribution of ceramic grain sizes, therefore the quality of the obtained ceramics can be described by the values of grain boundary conductivities [40,52]. The grain boundaries, which play an important role for ionic conductivity, may have essentially different properties and completely different structure than the grain bulk. Generally, ionic conductivity depends on the concentration of defect and mobility of charge carriers, while grain boundaries may lower the mobility of the ions [52].

Conductivities of grain and grain boundary were evaluated and the results are illustrated in temperature dependences plots (Fig. 46).

As it can be seen from Fig. 46, CeO₂-YSZ ceramics possess high grain boundary conductivity despite the annealing temperature. The highest bulk (σ_b) and grain boundary (σ_{gb}) conductivity values were increased by one order of magnitude for ceramics annealed at 1500°C compared with annealing temperature of 1000°C. Moreover, the increase of grain boundary conductivity by one order of magnitude was observed regardless of the annealing temperature.
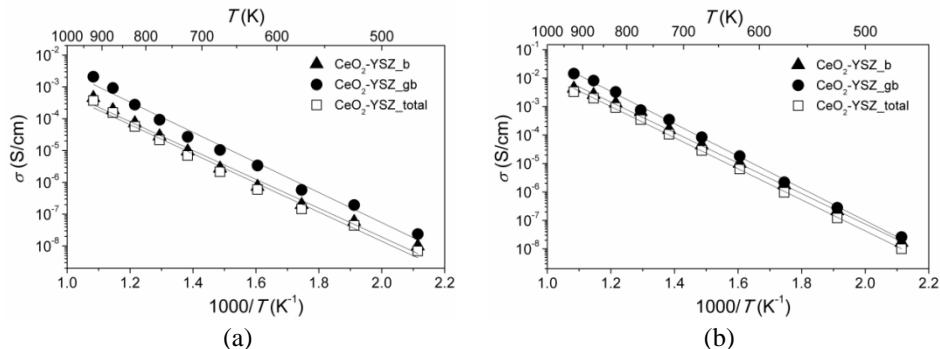
Fig. 46. Temperature dependences of the bulk (*b*), grain boundary (*gb*) and total conductivities of CeO$_2$-YSZ ceramics annealed at (a) 1000 and (b) 1500°C

The obtained conductivities correlate well with the microstructure of synthesized CeO$_2$-YSZ ceramics (see Fig. 47). According to structural analysis, the nano-sized grains of ceramics and coalescence of the grains into clusters were observed, which shows enhanced ionic conduction due to transport along the grain boundaries. It should be noted that the cross-section of the pellet surface was not polished or any other way processed. The summary of activation energies of CeO$_2$-YSZ ceramics obtained from Arrhenius plots is given in Table 13.
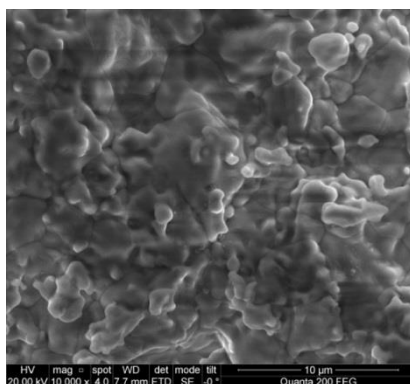
Fig. 47. A cross-sectional view of CeO$_2$-YSZ ceramics annealed at 1500°C

Table 13. Activation energies of bulk (*b*), grain boundary (*gb*) and total conductivities of CeO$_2$-YSZ ceramics annealed at 1000 and 1500°C

Temperature	CeO$_2$-YSZ ceramics		
	Activation energy		
	ΔE_b (eV)	ΔE_{gb} (eV)	ΔE_{total} (eV)
1000°C	0.91	0.95	0.92
1500°C	1.07	1.13	1.09

3.2.6. Formation and characterization of CeO_2-YSZ thin films by electron beam evaporation technique

Fig. 48 presents the GI-XRD patterns of CeO_2-YSZ thin films deposited on Ni foil, Si(100) and SiO_2/Si substrates using EB-PVD technique.
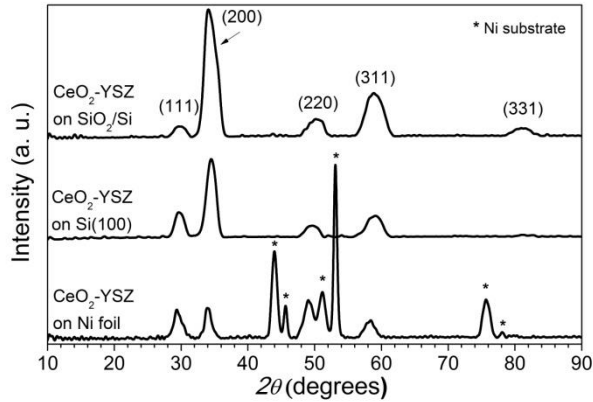
Fig. 48. GI-XRD patterns of the CeO_2-YSZ thin films formed on different substrates

Crystallographic planes with (111), (200), (220) and (311) orientations of thin films on Si(100) and Ni foil substrates were observed using a 1° grazing incident angle, while films deposited on SiO_2/Si substrate have an additional (331) crystallographic plane. It should be noted that the polycrystalline cubic structure with no peaks corresponding to tetragonal or monoclinic phases of the CeO_2-YSZ thin films was detected.

It was observed that thin a film deposited on Ni substrate produces peak shifts toward the lower angles, because of high degree of residual stresses in the foil. Among three substrates, the diffraction peak of CeO_2-YSZ on SiO_2/Si has the highest peak of (200) crystallographic orientation, while CeO_2-YSZ on Ni foil has the lowest intensity of the (200) peak.

Next to the GI-XRD measurements, a conventional θ-2θ scan was also performed for all thin films. It was found that the presence of predominant (200) crystallographic orientation in all thin films was observed regardless of the substrate used for deposition, in contrary to the results of CeO_2-YSZ ceramics annealed at 1100°C with dominating (111) crystallographic orientation. The crystallite sizes of CeO_2-YSZ thin films deposited on Ni foil, Si(100) and SiO_2/Si substrates varied in the range of 11–32 nm, 9–19 nm, 7–13 nm, respectively. The measured values of crystallite sizes were three times lower when compared with the results obtained by Saporiti [91].

It is well known that the properties of a thin film, such as density, porosity, mechanical stability, optical reflectivity, conductivity, the origin growth of the thin film, etc. are closely related to its microstructure, especially to its morphology and surface roughness [71]. Therefore, the evaluation of surface topography of thin films is an essential part of this research. Fig. 49 shows the AFM images of CeO_2-YSZ

thin films deposited on Si(100), SiO₂/Si and Ni foil substrates using the EB-PVD process.
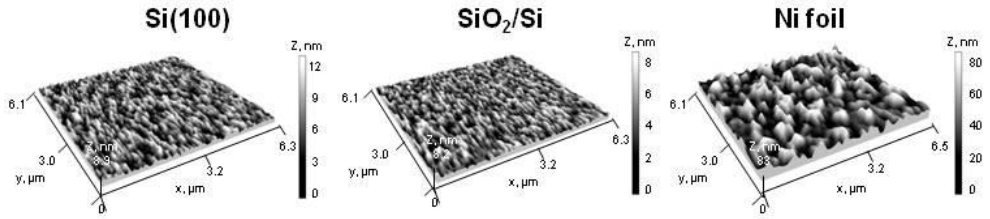
Fig. 49. AFM images of CeO₂-YSZ thin films deposited on different substrates

Table 14 presents the main roughness parameters, such as root mean square roughness, arithmetic average height, skewness, kurtosis and mean height of the evaporated CeO₂-YSZ thin films, evaluated in terms of AFM topography images. The measured value of the root mean square (R_q) surface roughness parameters of the Si(100), SiO₂/Si and Ni foil were 0.59 ± 0.02, 0.62 ± 0.02 and 7.63 ± 0.02 nm, respectively.

Table 14. Roughness parameters: root mean square (R_q), arithmetic average height (R_a), skewness (R_{sk}), kurtosis (R_{ku})) and mean height distribution (Z_{mean}) of CeO₂-YSZ thin films deposited on different substrates

Substrate	CeO₂-YSZ				
	Roughness paramater				
	R_q (nm)	R_a (nm)	R_{sk}	R_{ku}	Z_{mean} (nm)
Si(100)	1.24	0.96	-0.05	3.09	4.46
SiO₂/Si	1.07	0.81	-0.02	3.44	3.87
Nickel foil	10.51	8.29	0.61	3.50	32.03

According to AFM images, CeO₂-YSZ thin films deposited on Si(100) and SiO₂/Si substrates using the EB-PVD technique revealed a uniform and dense surface (Fig. 49), with the surface structures having a mean height of 4.46 and 3.87 nm, respectively (Table 14). Moreover, the thin films deposited on the SiO₂/Si substrate revealed the lowest R_q value of 1.07 nm. Additionally, CeO₂-YSZ thin films deposited on the aforementioned substrates exhibited a symmetrical growth of the films (R_{sk} values were close to 0).

In the case of Ni foil as a substrate, the growth of CeO₂-YSZ thin films was different. This substrate has a higher natural roughness than Si(100) or SiO₂/Si, therefore uneven structures which have a mean height of 32.03 nm were formed on its surface. R_q value of 10.51 nm was found. However, the growth mechanism of thin films on Ni foil is important due to possible applications of Ni as an electrode (anode) material for micro-SOFC [5,47]. It should be noted that the obtained thin films evaporated on all substrates, including Ni foil, were mechanically stable and adhered well to the substrate.

Fig. 50 presents an SEM cross-section image of CeO_2-YSZ thin film deposited on the SiO_2/Si substrate. The results show that the growth of the film has a tendency to develop a dense microstructure.
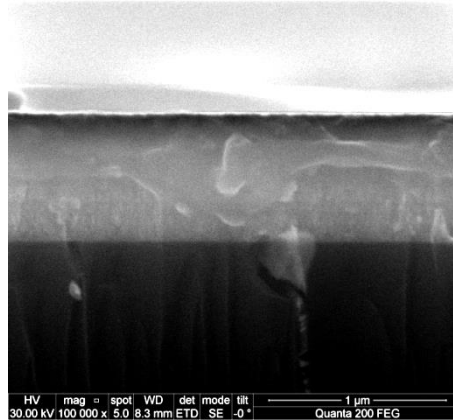
Fig. 50. The cross-section of evaporated CeO_2-YSZ thin films

3.2.7. In- and across-plane conductivity measurements of electrolyte thin films

A variety of current research activities in solid-state ionics has dealt with the ionic conductivity in nanomaterials, including thin films. A strong deviation of thin film properties can be observed compared to the bulk ones [34,86,167,189]. The evaluation of ionic conductivity of thin films is complicated due to many reasons, such as limitations of experimental equipment, preparation and mounting of the sample, insufficient contact between the sample surface with the formed electrodes and the contact electrodes, the influence of extraneous wires, the choice of the substrate material and measurement geometry, as well as the quality of the films, etc.

One of the tasks of this dissertation includes the evaluation of conductivity mechanisms in thin films. There are various equipment and measurement designs (across-plane or in-plane configurations) which can be tailored reaching this goal [76,86,88,120,167,189,190]. For better understanding, three different pieces of impedance spectroscopy equipment were used for measuring solid electrolyte thin films in this study. Investigations in the low frequency range (from 10 Hz to 10 MHz) were performed using an impedance analyser Alpha-AK and Alpha-A (Novocontrol, Germany). Also, the corresponding investigations in the high frequency range (from 300 kHz to 3 GHz) based on the coaxial waveguide technique were carried out using Agilent E5062A network analyser. Taking into account different specifications of devices, the samples were prepared on different substrates (Al_2O_3 and SiO_2/Si) with the required geometry of electrodes. Patterning of the paste and sputtering of thin films was used to prepare the Pt electrodes. The obtained results and problems encountered in measuring properties of thin films are described in the following.

In this research, the *in-plane* (see Fig. 51) configuration was used, i.e. samples were measured along the film, in order to characterise then. It should be noted that

this type of measurement reveals information not only about the material from which the thin film was formed, but also the quality of the film.
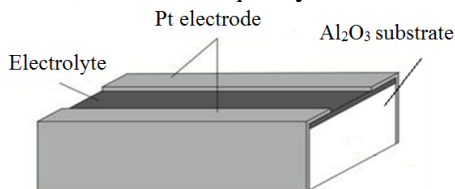
Fig. 51. The principal scheme of the solid electrolyte membrane prepared for the *in-plane* impedance measurements

In order to determine specific electrical parameters of superionic materials or membrane structures, the evaluation of geometric dimensions is very important, i.e. the ratio of the area to length. The approximate dimensions of the sample are illustrated in Fig. 52.
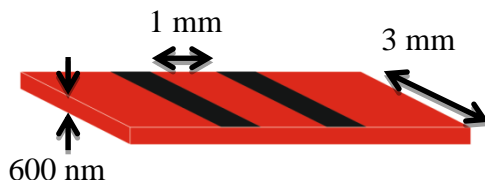
Fig. 52. A schematic overview of the sample with indicative geometrical dimensions: thickness of the film is 600 nm, width of the sample is 3 mm and length between electrodes is approximately 1 mm

The geometric factor can be simply calculated from Fig. 52 as follows: $S/l = 0.0018$ mm. The value of S/l shows that the measured absolute resistance of a thin film is very high and practically undetectable at temperatures lower than 600 K. Thus, in order to evaluate the properties of thin films, special preparation or geometry of the sample is needed. In this research, the electrical properties of electrolyte thin films were studied using different ways of sample preparation for testing.

The samples were deposited on an Al_2O_3 substrate for the IS measurements performed by Agilent E5062A network analyser. Firstly, thin films (thickness of ~600 nm) were deposited on the Al_2O_3 substrate. The samples were cut into 1.5×3 mm pieces and Pt paste was applied to form electrodes subsequently annealing them at 700°C. The distance between electrodes was smaller than 1 mm. Examples of the samples are shown in Fig. 53.
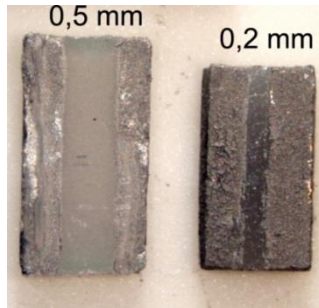
Fig. 53. Samples with YSZ electrolyte thin film prepared for IS measurement. Distances between electrodes were 0.5 and 0.2 mm, respectively

IS measurements were performed in the frequency range of 10 Hz to 3 GHz at the temperatures from 500 to 740 K. As an example, typical impedance spectra of 10-YSZ thin film under 600 K temperature is presented in Fig. 54.
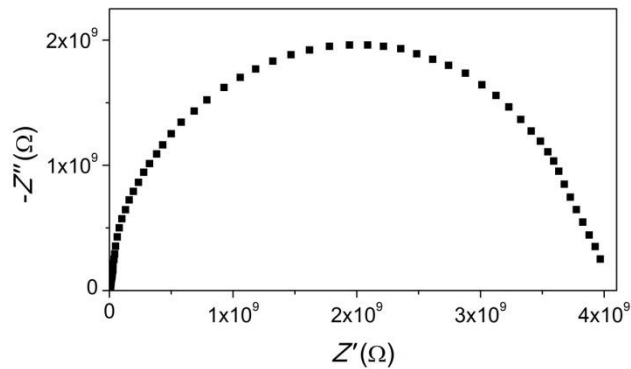
Fig. 54. A Nyquist plot of 10-YSZ thin film deposited on Al_2O_3 substrate measured at 600 K temperature (distance between electrodes was 0.2 mm)

In terms of impedance plots, only main semi-circle was observed in Fig. 54. For comparison, high quality sintered electrolyte materials (bulk samples) generally constitute two semi-circles (as a minimum). Similar results were discussed and reported in literature [75,191]. This is commonly reported for nano-scaled materials, either for nanometre grain size or very thin thin films [190,192,193]. However, Gerstl et al. [167] showed that appropriate selection of the electrode geometry allows a separation of bulk and grain boundary contributions even in very thin YSZ layers and for small grain sizes.

Due to the fact that IS measurement of thin films (when the thickness is lower than 1 µm) can be strongly influenced by the electrode geometry, in order to increase the geometric factor and to achieve the optimal conditions for impedance measurement, the distance between Pt electrodes was varied in this research. Pt electrodes were formed using the photolithography process. Firstly, YSZ electrolyte thin film (thickness of 600 nm) was formed on the substrates (on Al_2O_3 and SiO_2/Si separately); then, the Pt electrode (thickness of 200 nm) was formed on the top surface of the electrolyte thin film. Finally, the pattern was formed on the surface of Pt electrode trough the photomask (see Subchapter 2.1.4.1., Fig. 14 (b)) followed by

etching with direct Ar$^+$ ions. The distances between electrodes varied as follows: 2, 4, 6, 8 and 10 µm. It should be noted that samples were formed in parallel on both substrates. A schematic example of the produced sample on a SiO$_2$/Si substrate is demonstrated in Fig. 55. The ionic properties of thin films deposited on Al$_2$O$_3$ substrates were characterized in a wide range of frequency (from 300 kHz to 3 GHz) by cutting them into 1.5 × 3 mm pieces using laser cutting. The samples on SiO$_2$/Si were used for IS measurements (equipment of Novocontrol; in the frequency range from 10 Hz to 10 MHz) with no additional sample processing.
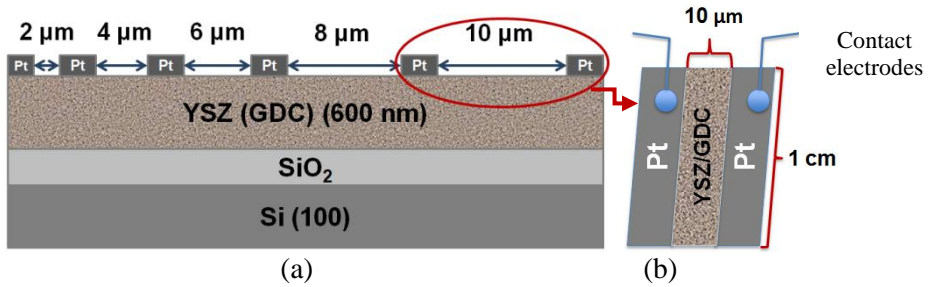
Fig. 55. A schematic representation of the sample formed on SiO$_2$/Si substrate for IS measurements performed by an impedance analyser Alpha-AK (a); (b) – top view of the sample (the scale has not been maintained)

Laser cutting was carried out from the backside of the sample without reaching the YSZ electrolyte thin film. The sample on the alumina substrate was incised to the half of its thickness in order to observe the film. Nevertheless, it was found that the laser cutting strongly affects a sputtered Pt film and the cutting-related problem is illustrated in Fig. 56.
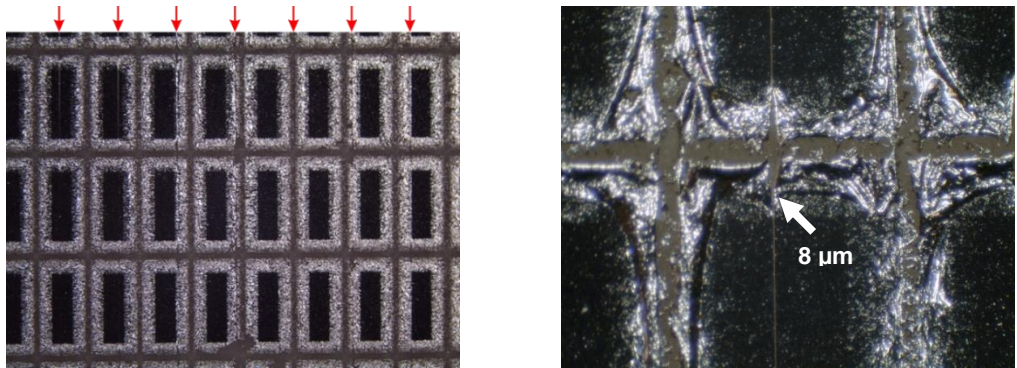
Fig. 56. The impact of laser cutting on the sample surface (prepared on Al$_2$O$_3$ substrate). Arrows in a figure indicate gaps between Pt electrodes

Fig. 56 demonstrates that the laser radiation violates not only the Pt electrode, but electrolyte film as well. This occurs due to the fact that Al$_2$O$_3$ substrate is sufficiently transparent to the wavelengths of 1064 nm, which were used during the process. It is evident that certain areas of the sample were affected and the Pt thin film was coiled up where the laser beam was in contact with the sample, i.e., cutting

areas appeared with no Pt electrode on the electrolyte surface. Moreover, the coiled up Pt electrodes may influence the short-circuiting of the electrolyte thin film.

Taking into account these observations, the Pt paste was applied as well in order to correct the electrode surface. The prepared sample is presented in Fig. 57.
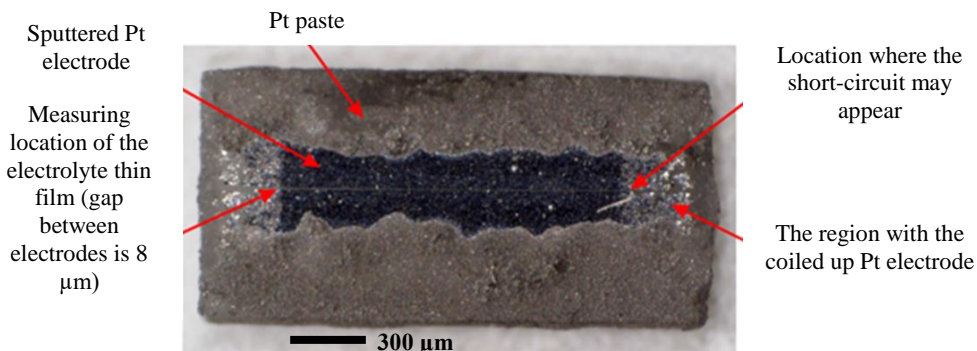
Fig. 57. 10-YSZ thin film on the Al_2O_3 substrate prepared for the IS measurements

The Nyquist impedance plots of the 8-YSZ thin film deposited on Al_2O_3 substrate, with a formed gap size of 8 µm between Pt electrodes are presented in Fig. 58.
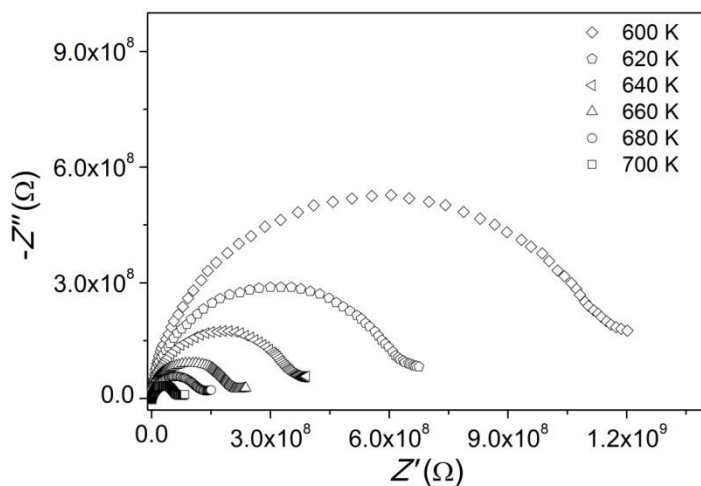
Fig. 58. Typical impedance spectra of 10-YSZ thin film measured at temperatures in the range of 600–700 K. The distance between Pt electrodes was 8 µm

Fig. 58 demonstrates the appearance of one contribution in the high-frequency response which is generated from the electrolyte thin film itself. Generally, the low-frequency response appears from electrodes. P. Briois et al. [194] investigated ionic conductivity of YSZ films and showed that the relaxation frequency associated with the high-frequency semi-circle seems to correspond to a major contribution of the bulk, particularly, if the film reveals a dense and pore-free microstructure.

According to impedance data, the temperature dependences of ionic conductivity of electrolyte thin films were determined and displayed in Fig. 59.
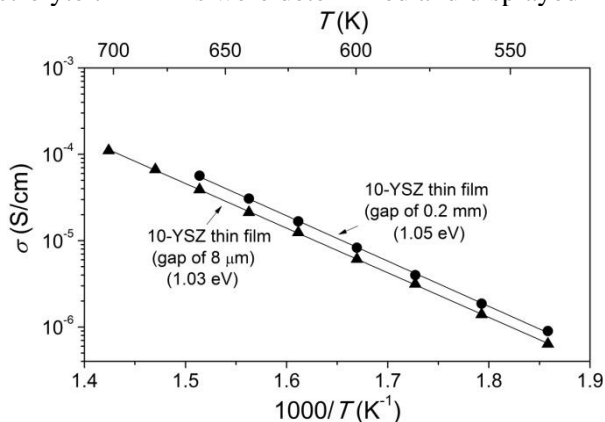
Fig. 59. Temperature dependences of ionic conductivities of 10-YSZ thin film with respect to different gaps between Pt electrodes

The ionic conductivity data for electrolyte thin films prepared using the EB-PVD method has not been widely reported yet. However, the obtained results were lower by one order of magnitude compared to other studies [83]. E. Wanzenberg, et al. [190] presented a model of Kenjo and Nakagawa which indicates that the measured conductivity is dependent on the thickness of the sample, therefore this may cause substantial differences between the results obtained by different authors.

Furthermore, as can be seen from Fig. 59, the activation energy values of the electrolyte thin film are typical for oxygen ionic conductors and practically coincide with the values of synthesized ceramics (see Fig. 30). According to the Arrhenius law which allows us to determine the activation energy by considering the slope of the curve, the activation energies of 1.03 and 1.05 eV for 10-YSZ thin film were found. The activation energy values appear to be in good agreement with the literature data of about 1.0 and 0.94 eV for YSZ thin films [86,191]. However, it should be noted that these results were obtained using different gap sizes between Pt electrodes during IS measurements, i.e. 0.2 mm and 8 μm.

As was mentioned above, the further step of this research was to achieve the optimal conditions for the impedance measurement by adjusting the distance between Pt electrodes. For this purpose, a sample with 10-YSZ thin film evaporated on a SiO_2/Si substrate (see Fig. 32) was used. Measurements were carried out using the Alpha-AK (Novocontrol Technologies) impedance analyser in the frequency range from 10 Hz to 10 MHz.

Fig. 60 illustrates the etching process of the Pt electrode on the YSZ thin film surface.
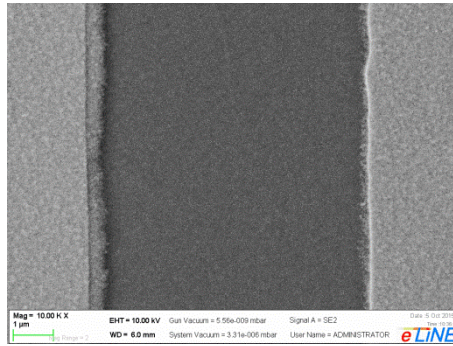
Fig. 60. 10-YSZ thin film with a gap size of 6 µm between Pt electrodes

Fig. 60 clearly shows that there are no residues of platinum on the electrolyte surface which may cause the short-circuit effect. However, minor deviations of the gap size between Pt electrodes were observed for small distances, i.e. the actual gap sizes for 2 and 4 µm were 1.5 and 3.1 µm, respectively. As expected, due to some technological limits of the Alpha-AK analyser, it was not possible to perform measurements with such small gaps between Pt electrodes.

Summarizing the obtained results, Fig. 61 depicts the impedance spectra of 10-YSZ thin film measured using 6, 8 and 10 µm gaps between Pt electrodes, respectively. It is evident that the separation of bulk and grain boundary impedance is possible using an 8 µm gap.
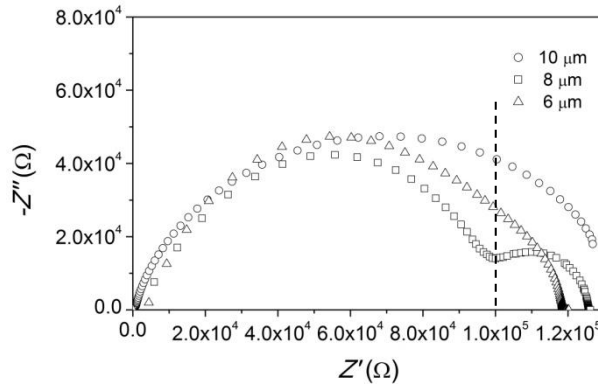
Fig. 61. The Nyquist plot of 10-YSZ thin film deposited on SiO$_2$/Si substrate measured at 650°C. The gap sizes between Pt electrodes varied from 6 to 10 µm

Fig. 62 demonstrates the geometries of electrodes prepared on the sample surface for across- and in-plane IS measurement using the Alpha-A analyser.

Fig. 62. Geometries of the electrode: (a) circular; (b) stripe electrodes

Fig. 63 displays the temperature dependences of ionic conductivities of 10-YSZ thin with respect to the measurement type.
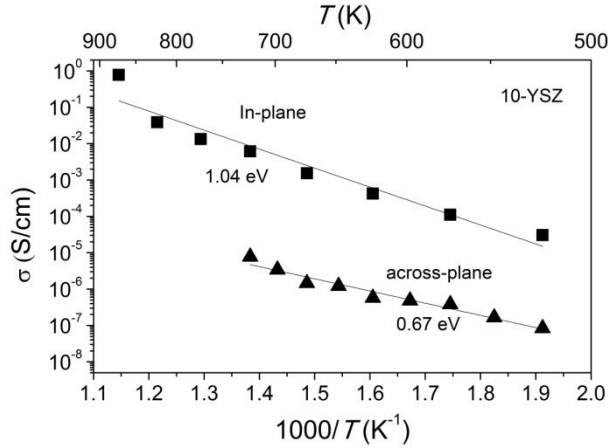
Fig. 63. Temperature dependences of ionic conductivities of 10-YSZ thin film with respect to *across-* and *in-plane* configuration

Beckel et al. [47] overviewed the relationship between the microstructure and the conductivity of the electrolyte thin film. Moreover, the idea that the amount of strain present in a thin film affects the electrical properties was discussed as well. It was assumed that the higher compressive stress in the thin film determines the higher activation energies which can be up to 1.3 eV. Thus, according to the microstructure and required growth of YSZ thin films (Fig. 32), as well as the properties obtained from IS measurements, it can be concluded that the EB-PVD is a suitable technique for the formation of high quality electrolyte thin films, although it was noticed that thin films show about 3 times lower ionic conductivity than microcrystalline samples. The decrease in ionic conductivity of an electrolyte with respect to the decrease of the film thickness was obtained in [195].

Thus, the obtained results show that both sample preparation methods can be used for IS measurements of thin films. However, in order to separate different distributions of bulk and grain boundary, the use of optimal electrode configuration is needed.

3.3. Pt thin films as electrodes for µ-SOFC: formation and properties

In this subchapter, the microstructure, porosity, stresses and resistivity of thin platinum electrodes (thickness of 200 nm) deposited on Ti/SiO₂/Si substrate are demonstrated. Pt films were formed at different working pressure of argon gas in the chamber (4.90, 0.13, 0.60, and 0.065 Pa, denoted as: first (1st), second (2nd), third (3rd) and fourth (4th) sample series, respectively) during magnetron sputter-deposition process and followed by thermal treatment (in the range of 500–800ºC).

The crystalline structure of Pt electrodes was analysed using grazing incidence X-ray diffraction. The lattice parameter and residual stresses of platinum thin films were defined using $\sin^2\psi$ method. Surface morphology and the microstructure of electrodes were investigated using AFM and SEM, respectively. The electrical properties of the Pt thin films were evaluated using the four-point probe method. Typical time intervals and substrate temperature ranges were defined to produce stable porous Pt electrodes which are applicable in the PEN structure (Pt-YSZ-Pt). It is shown that the control of argon gas pressure in the chamber during the sputtering process and the following thermal treatment are excellent tools for producing a positive/negative Pt electrode with the required mechanical stability, structural and electrical properties. The morphological changes of the Pt thin films were analysed in the temperature region which is typical for the operation of micro-solid oxide fuel cells.

3.3.1. Elemental composition of the Pt/Ti thin films' surface

Due to poor adhesion between the Pt electrode and SiO₂/Si substrate and the tendency of platinum silicide to compose at low temperatures, titanium adhesive sublayer on SiO₂/Si substrate was formed.

The atomic composition of the Pt/Ti thin films was studied using X-ray photoelectron spectroscopy (XPS). Fig. 64 demonstrates a typical wide-scan spectra of XPS analysis of as-deposited Pt thin films formed at 0.065 Pa (4th sample series) pressure and annealed at 600 and 800°C temperature for 15min.
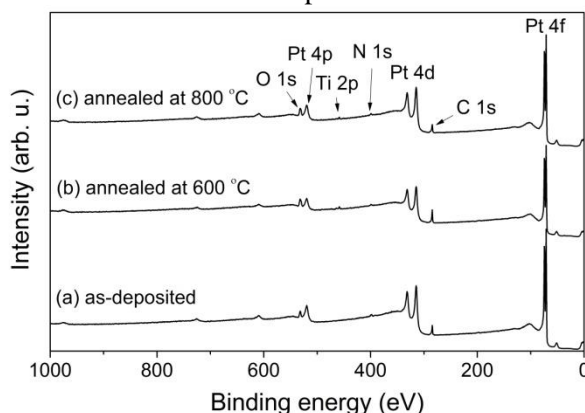
Fig. 64. Wide-scan X-ray photoelectron spectra of the as-deposited (a), annealed at 600°C (b), and at 800°C (c) temperature Pt/Ti thin films

Intensive peaks of Pt 4p, Pt 4d, Pt 4f, and C 1s core levels were observed. In addition to these peaks, weak intensity peaks of Ti 2p, O 1s, and N 1s core levels were also detected. The peak of Ti 2p core level for the as-deposited Pt/Ti thin film was not detected. A summary of the XPS results is given in Table 15.

According to the data, as-deposited Pt/Ti thin films have no Ti on the Pt surface. It is also evident that with the increase of annealing temperature, the atomic concentration of Ti on the surface of Pt increases and reaches up to 1.4 at.%.

Table 15. The elemental composition of the as-deposited and thermally treated at 600 and 800°C temperature Pt/Ti thin films (4th sample series) obtained using electron spectroscopy for chemical analysis

Peak Name	As-deposited	Annealed at 600°C	Annealed at 800°C
	Atomic %	Atomic %	Atomic %
Pt 4f	38.1	26.8	35.9
O 1s	12.7	16.6	17.0
N 1s	6.9	6.0	6.2
Ti 2p	0.0	1.2	1.4
C 1s	41.7	49.4	39.5

It is a well-known fact and numerous studies have been conducted regarding the Ti diffusion behaviour in Pt grain boundaries [110,112,113,196–198]. The authors pointed out that the composition changes of Pt/Ti films are closely related to the diffusion and oxidation of Ti during the annealing process. On the other hand, it was demonstrated that the amount of Ti/TiO$_x$ presence near/onto the Pt surface depends on the thickness of the layers, deposition temperatures, annealing environments and time, as well as the deposition method [196].

The rather low detected concentration of Ti is in agreement with [113], who demonstrated that the concentration of Ti and the concentration of TiO$_2$ hillocks on the Pt surface decreases with increasing the thickness of Pt film; therefore, the Ti sublayer thickness chosen in the current experiment corresponded to the range of thicknesses where Ti diffusion through the Pt film was not efficient even in the case of high annealing temperature [113].

3.3.2. The morphology of Pt/Ti thin films: SEM and AFM analysis

Fig. 65 presents SEM images of the Pt/Ti thin films magnetron sputter deposited at: the highest Ar pressure (4.9 Pa, 1st sample series) (Fig. 65, a) and further thermally annealed for 15 min at 600°C (Fig. 65, c), 700°C (Fig. 65, e), 800°C (Fig. 65, g); as well as at the lowest Ar pressure (0.065 Pa, 4th sample series) (Fig. 65, b) and further thermally annealed for 15 min at 600, 700, 800°C, respectively (Fig. 65, d, f, h). Fig. 65, (i) shows a cross-section of the Pt layer as deposited at 4.9 Pa, and (j) represents the cross-section of the Pt film magnetron sputtered at 0.065 Pa and thermally treated at 600°C for 15 min.
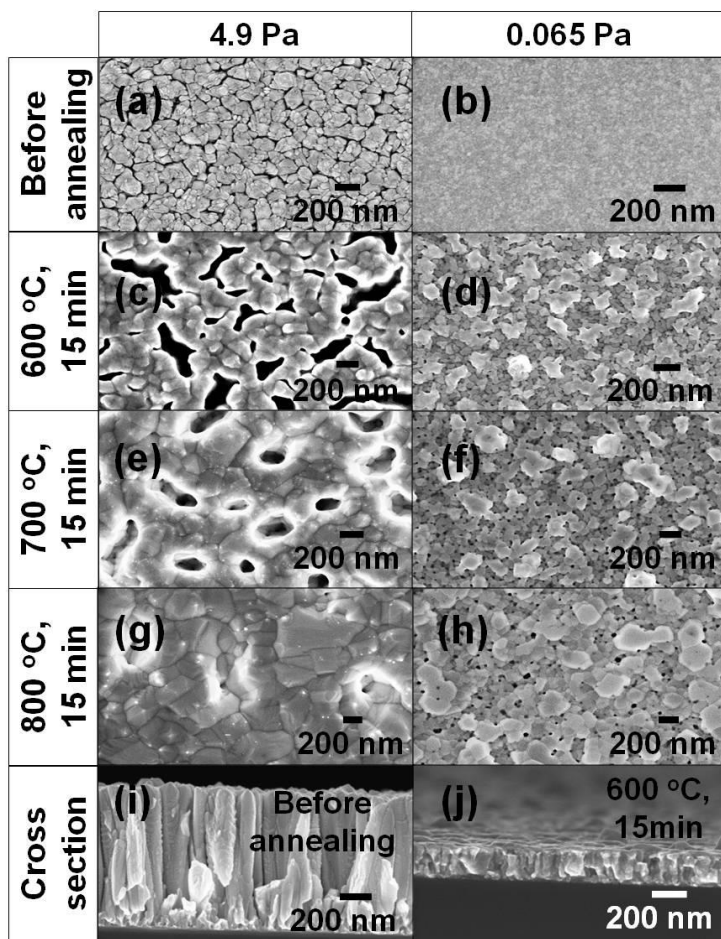
Fig. 65. SEM images of the top view and cross-section of the Pt/Ti thin films ((a), (c), (e), (g), (i): 1st sample series; (b), (d), (f), (h), (j): 4th sample series). (a) and (b) Pt/Ti films before annealing; (c), (d) after annealing at 600°C; (e) and (f) after annealing at 700°C; (g), (h) after annealing at 800°C, respectively; (i), (h) corresponds with the cross-section of Pt/Ti films before annealing and after annealing at 600°C for 15 min, respectively

The SEM results show that the increased argon pressure (4.9 Pa) in the chamber during the deposition process allows the formation of porous platinum thin films, without any thermal treatment (Fig. 65, a). This is in good agreement with other studies [5,106,108]. For the films deposited at high Ar pressure, the melting, coarsening and coalescence of grains of Pt/Ti thin films, and pore-clogging after thermal treatment were observed (Fig. 65, c, e, g).

The differences in pore size and shape depending on the argon pressure should be noted. In the case of high Ar pressure (1st sample series) the elongated pores of the Pt/Ti thin films were determined before and after annealing at 600°C temperature (Fig. 65, a, c). Coarsening of the grains was observed after annealing at 700°C temperature and the film with pores in the 150–200 nm size range was formed (Fig. 65, e). Fig. 65 (i), (j) shows that pores evolve not only on the surface, but through

the whole thickness of Pt/Ti film. Unfortunately, the structures formed at 4.9 Pa Ar pressure are not stable against thermal treatment. After 15 minutes of thermal treatment at 800°C, the pores started to close and the value of porosity reached 0.5% (Fig. 65 (g)). This was especially observed when the time of annealing increased up to 4 hours.

The deposition of platinum thin films at a low argon pressure (0.065 Pa) in the chamber during the magnetron sputtering process results in a smooth surface (Fig. 65 (b)), and only further thermal treatment results in the formation of pores (Fig. 65, d, f, h). Fig. 65 (d) shows that the pores of Pt/Ti thin films start to evolve at the annealing temperature of 600°C. Pt/Ti thin film sputtered at 0.065 Pa argon pressure after further thermal annealing at 800°C still maintains porosity (Fig. 65 (h)). The obtained results correlate with other studies [105–107]. In addition, because of the titanium sublayer, we were able to provide good adhesion between the Pt thin film and SiO₂/Si substrate. This is probably due to the fact that we avoided large voids at the interface of layers reported by other authors [108].

Fig. 66 summarizes the dependence of the main morphological parameter – root mean square roughness (R_q) (AFM measurements results) and porosity of Pt/Ti thin films magnetron sputtered on SiO₂ substrate deposited at different working pressures of Ar gas (4.9, 0.13, 0.6, 0.065 Pa) and following thermal isochronic annealing (for 15 min at 500–800°C temperatures). The porosity of the samples versus thermal treatment is shown by transparent symbols. The resultant root mean square roughness as well as porosity of the films annealed at 800°C for 4 hours are presented as well and noted as 800, 4h.
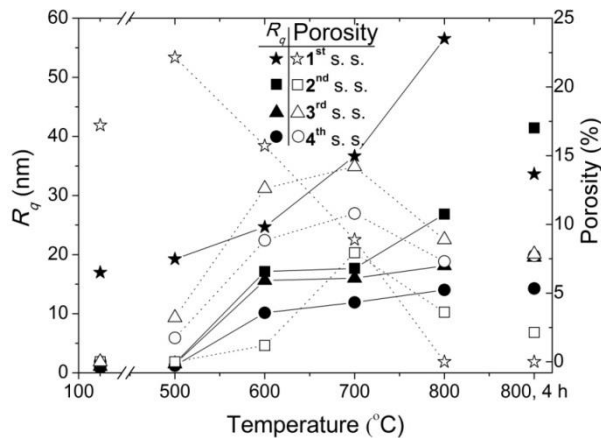
Fig. 66. The dependence of the root mean square roughness (R_q) (filled symbols) and porosity (transparent symbols) of Pt/Ti thin films magnetron sputtered on SiO₂ substrate at different working pressures of Ar gas (4.9 Pa – 1st sample series, 0.13 Pa – 2nd sample series, 0.6 Pa – 3rd sample series, 0.065 Pa – 4th sample series) and the following thermal annealing (for 15 min at 500–800°C temperatures, as well as 4 h at 800°C)

Table 16 presents other roughness parameters (skewness, kurtosis, and mean height) of Pt/Ti films as-deposited and after thermal treatment at various temperatures (500–800°C) for 15 min and 4 hours.

Table 16. Roughness parameters (skewness (R_{sk}) and kurtosis (R_{ku})) as well as mean height distribution of Pt/Ti thin films as-deposited and further thermally annealed for 15 min at 500, 600, 700, 800°C, additionally for 4 hours at 800°C, evaluated in terms of AFM surface topography images

	1st s. s.			2nd s. s.			3rd s. s.			4th s. s.		
	Parameters											
$T_{annealing}$, time	R_{sk}	R_{ku}	Z_{mean} (nm)	R_{sk}	R_{ku}	Z_{mean} (nm)	R_{sk}	R_{ku}	Z_{mean} (nm)	R_{sk}	R_{ku}	Z_{mean} (nm)
As-deposited	0.21	3.18	63.71	-0.06	3.71	5.54	-0.39	5.38	7.49	-0.14	3.63	4.40
500°C, 15 min	0.06	3.10	79.16	3.02	38.69	6.27	2.87	8.35	6.45	0.20	4.08	6.98
600°C, 15 min	-0.36	3.98	207.38	1.04	5.32	47.54	0.97	6.02	40.12	1.57	8.41	32.91
700°C, 15 min	-0.63	4.21	323.69	1.43	7.40	57.32	1.12	5.12	43.82	0.84	4.99	37.90
800°C, 15 min	-0.79	4.13	302.31	0.78	3.45	68.78	0.85	5.04	62.98	1.01	5.86	42.90
800°C, 4 h	0.08	3.04	114.47	0.00	2.73	147.94	1.43	7.23	59.02	1.29	6.72	59.23

It is known that the roughness parameters can determine the mechanical properties of the films. For instance, if the surface is too rough, heavy abrasive wear will appear, which can ultimately lead to adhesion or scuffing [26]. On the other hand, for very smooth surfaces, strong adhesive force and adhesive wear can occur under very small loads. It is notable that the roughness parameters (Fig. 66, Table 16) correlate well with the SEM images of the Pt/Ti films. Changes in the porosity and roughness parameters of Pt/Ti thin films during thermal annealing, including long time annealing (for 4 hours at 800°C), were discovered.

The lowest root mean square roughness (R_q) of 0.84 nm was observed for platinum thin films formed at 0.065 Pa argon pressure (4th sample series) before annealing, with the surface structures having a mean height of 4.40 nm (Fig. 66, Table 16). The highest R_q value of 56.53 nm of platinum films sputtered at 4.9 Pa argon pressure was established after annealing at 800°C temperature for 15 min, having a mean height of 302.31 nm (Fig. 66, Table 16).

Zero skewness (R_{sk}) was observed for Pt/Ti thin films sputtered at 0.13 Pa argon pressure (2nd sample series) after annealing at 800°C for 4 hours (Table 16). This shows a symmetrical height distribution, while positive and negative skewness describe surfaces with high peak sand filled valleys, and with deep scratches and lack of peaks, respectively [199]. The largest asymmetry of the surface elements was observed for Pt/Ti films sputtered at 4.9 Pa argon pressure (1st sample series) after annealing at 800°C for 15 min in air, with R_{sk} value of -0.79, which indicates a predominance of valleys. In addition, negative R_{sk} values were found for the 2nd, 3rd and 4th sample series before annealing, as well as 4th sample series annealed from 600 to 800°C temperature for 15 min (Table 16). Probably, because of the surface coalescence and coarsening after 4 hours annealing at 800°C (1st sample series) positive R_{sk} value was observed.

The roughness parameter kurtosis (R_{ku}) is also used to describe the sharpness of the probability density of the profile [199]. The lowest R_{ku} value (2.47) was found for Pt/Ti films sputtered at 0.13 Pa argon pressure (2nd sample series) annealed at

800°C for 4 h (Table 16). R_{ku} parameter value of more than 3 for all other films was determined, which corresponds to bumpy surface topography.

Summarizing the surface morphology changes of the Pt films deposited on Ti sublayer, it is possible to conclude that Ar pressure during the deposition and further thermal treatment are efficient technological tools in the production of porous films. It should be noted that in contrary to [112], as was discussed in subchapter 3.3.1., the high concentration of Ti on the film that usually contributes to the hillock formation on the platinum surface was not observed.

3.3.3. XRD analysis of Pt/Ti thin films

Fig. 67 shows the grazing incidence XRD patterns of the Pt/Ti thin films as-deposited on a SiO_2/Si substrate at different argon gas pressure in the chamber (1st-4th sample series).
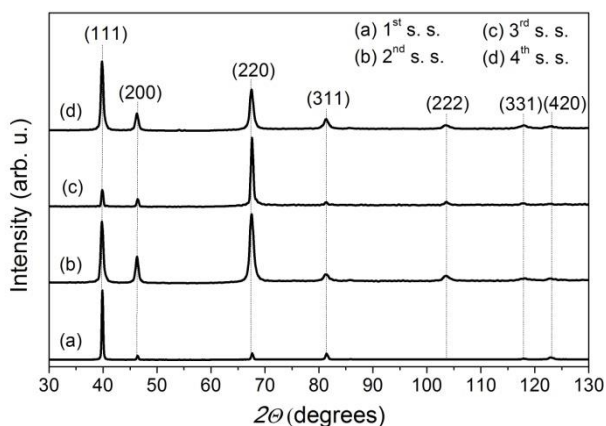
Fig. 67. Normalized intensity GI-XRD patterns of the platinum thin films as-deposited at different argon pressure in the chamber ((a): 4.9 Pa, (b): 0.13 Pa, (c): 0.6 Pa, (d): 0.065 Pa) during magnetron sputtering process

Fig. 68 illustrates the influence of thermal annealing and presents grazing incidence XRD patterns of the platinum thin films deposited at low argon gas pressure (0.065 Pa) before thermal treatment and after annealing at 600 and 800°C temperature for 15 min in air. All diffraction profiles were compared with the standard pattern taken from the PDF-4 database (04-001-0112).
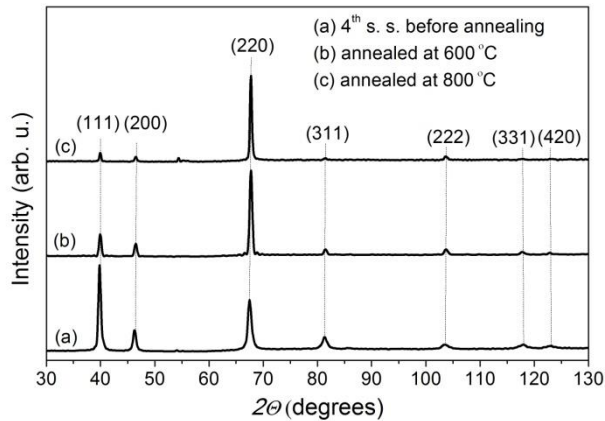
Fig. 68. Normalized intensity GI-XRD patterns of the platinum thin films as-deposited at 0.065 Pa argon pressure and thermally treated at 600 and 800°C temperature for 15 min

X-ray diffraction measurements of conventional θ-2θ scan were also performed for all samples (1st–4th sample series). It was found that Pt/Ti thin films were highly textured and have a dominating (1 1 1) crystalline orientation. However, contrary to the results obtained in [112], we did not observe any peaks of Ti. In order to maximize the diffraction volume of the thin film surface region, XRD measurements using grazing incidence angle of 1.5º were carried out, however, the presence of titanium has also not been established.

XRD patterns obtained using grazing incidence angle of 1.5º show the presence of (1 1 1), (2 0 0), (2 2 0), (3 1 1), (2 2 2), (3 3 1), and (4 2 0) crystallite orientations (Fig. 67). According to Fig. 68, it is evident that mainly crystallites are oriented in (1 1 1) or (2 2 0) or a mixture of (1 1 1) and (2 2 0) crystalline planes are detected. The trend of crystallite orientation of the Pt/Ti films deposited at different argon gas pressure in the chamber is not clearly defined. However, it is visible that the sputtered platinum of the 1st sample series (curve (a)) has the crystallites oriented in (1 1 1) plane, while the 3rd sample series (curve (c)) – in (2 2 0) plane.

According to Fig. 68, after the thermal treatment at higher than 600°C temperature for 15 min in air, the crystallographic orientation of crystallites becomes (2 2 0). Other researchers [106,108,114] reported textured Pt films with dominating orientation of (1 1 1)/(2 2 2) or (2 0 0) planes after annealing at high temperatures. According to [110], the Pt surface energy minimization favours grain with (1 1 1) texture. According to our results, this is valid for high argon pressure magnetron-deposited samples. While, the strain-energy-minimization in thin films can be achieved by creating certain magnetron sputtering process conditions, e.g. Ar gas pressure in the chamber, for the growth of (2 2 0) oriented grains [110].

The crystallite sizes of Pt/Ti thin films defined from the Sherrer equation [200] before the thermal treatment varied in the range of 18.3–31.6 nm, 10.5–16 nm, 16.7–24.1 nm, 10.7–17.7 nm for the first (1st), second (2nd), third (3rd) and fourth (4th) sample series, respectively. The crystallite size increased with the increase of annealing temperature, as it was demonstrated in [110]. For example, the crystallite size of Pt/Ti thin films, deposited at 0.065 Pa Ar gas pressure, used for the

preparation of PEN structure, after thermal treatment at 600°C changed from 17.1 to 41 nm.

3.3.4. Stress analysis of the Pt/Ti thin films

The classical X-ray stress analysis, the so-called $sin^2\psi$ method [201], which consists of measuring a particular high-angle lattice plane (hkl) in various specimen orientation, was used in the current research. The (3 3 1) plane for the different platinum sample series has been investigated for XRD stress measurements. Fig. 69 shows $ln(1/sin\theta)$ vs. $sin^2\psi$ plots of platinum thin film formed at different argon pressure in the chamber during the magnetron sputtering process.
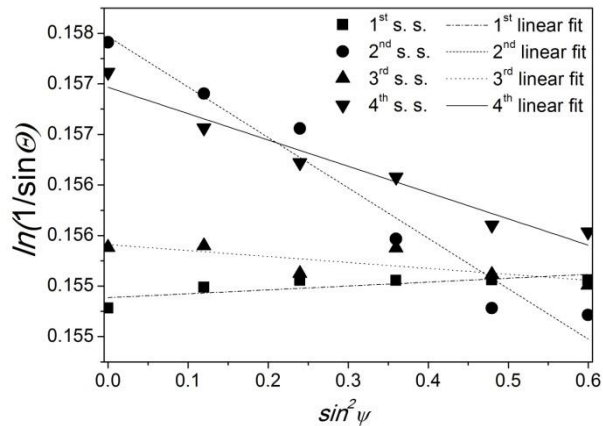
Fig. 69. The $ln(1/sin\theta)$ vs. $sin^2\psi$ plots of the platinum thin films as-deposited at 4.9 Pa ((1st) sample series), 0.13 Pa ((2nd) sample series), 0.6 Pa ((3rd) sample series), 0.065 Pa ((4th) sample series) argon pressure

The $ln(1/sin\theta)$-$sin^2\psi$ plots are presented for longitudinal directions of angle $\phi = 0°$ (with the assumption of no shear stress), where ϕ is the rotation angle of the specimen about its surface normal. From the linear straight-line fittings of $ln(1/sin\theta)$-$sin^2\psi$ curves, the stress-free lattice parameter, a_0, and residual stress, σ_R, were defined for the Pt/Ti thin films. The following elastic constant values of bulk platinum have been chosen: $E = 192.7$ GPa and $v = 0.39$ [112]. The defined values of the Pt lattice parameter were $a_0 = 0.3920$ nm, $a_0 = 0.3940$ nm, $a_0 = 0.3925$ nm, and $a_0 = 0.3933$ nm for the 1st, 2nd, 3rd and 4th sample series, respectively, while the value of Pt bulk was $a_{bulk} = 0.39239$ nm.

The nature of the residual stress of 2nd, 3rd and 4th sample series was found to be compressive. The tensile stress ($\sigma_R = 46$ MPa) was dominating for the 1st sample series. The compressive stress varied from -606 MPa up to -317 MPa for the 2nd and 4th sample series. For the 3rd sample series, where argon gas pressure in the chamber during magnetron sputtering process was 0.6 Pa, we have defined minimal residual stress value that reached only -168 MPa.

After annealing at high temperature, the compressive stress was changed to tensile stress and varied from 441 MPa to 408 MPa for 600 and 800°C annealing temperatures, respectively.

It should be noted that residual stress in the films was minimized. The values of residual stresses in the Pt/Ti thin films deposited by magnetron sputtering and further thermal treatment were found to be more than 1.5 times lower as compared with the results obtained by other researchers [112,202].

With regards to sign and residual stress levels in the Pt/Ti film, it should be noted that for many magnetron-deposited films there is a transition pressure, below which the coatings are in compression, while above this pressure, the coatings are in tension [203]. Compressive stress dominating at low gas pressure is usually attributed to the elastic energy in the coating due to ion bombardment during the deposition. In the region of high pressure, the stress becomes tensile because of reduced particle bombardment and shrinkage of coating during crystallization. Our results illustrate these effects and confirm the understanding of the processes taking place during magnetron sputtering deposition of Pt films. Having one more component of the stress, thermal stress, one can expect different sign as well as magnitude of the stress in the films as they reported in [110,114].

3.3.5. Resistivity of the Pt/Ti thin films

Fig. 70 shows bulk resistivity of the platinum thin films sputtered at 4.9, 0.13, 0.6, and 0.065 Pa Ar pressure versus thermal treatment (15 min at 500–800°C). The resistivity of the as-deposited films is presented (initial points in Fig. 70) as well as the resistivity of the films annealed for 4 hours at 800°C temperature is shown too (noted as 800, 4h).
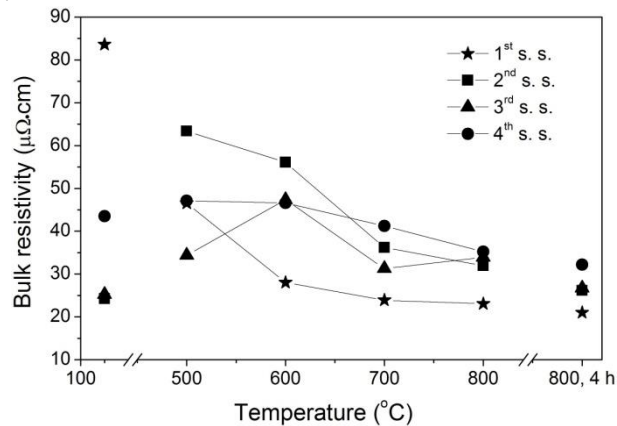
Fig. 70. The dependence of bulk resistivity of platinum thin films on annealing temperature (500–800°C)

The variation of resistivity with the gas pressure (the point before the axis break) correlate well with the tendencies in residual stress as was discussed in Chapter 3.3.4. It is notable that the electrical properties, i.e. bulk resistivity of the layers, exhibit different behaviour during the following thermal treatment. Pt/Ti films as-deposited at high Ar gas pressure show high bulk resistivity (85 μΩ·cm) and further decrease with the annealing temperature (down to 25 μΩ·cm), while Pt/Ti films deposited at low argon pressure, after initial increase in resistivity with annealing demonstrate almost identical resistivity after annealing at high (800°C)

temperatures (Fig. 70). Thus, the films deposited at high Ar gas pressure and demonstrating tensile stress exhibit the highest bulk resistivity because of the reduced ion bombardment and increased Ar atom concentration in the film. The comparable trend of decreasing the bulk resistivity of Pt/Ti thin films with increasing the annealing temperature was observed and reported in [105].

According to the obtained results, it can be concluded that porous and stable at high temperatures Pt/Ti thin films can be produced by applying low argon pressure during magnetron sputtering and further thermal annealing. Therefore, for the formation of PEN structure platinum electrodes, 0.065 Pa argon gas pressure in the chamber during magnetron sputtering process as well as further thermal treatment at 600°C for 15 min were selected.
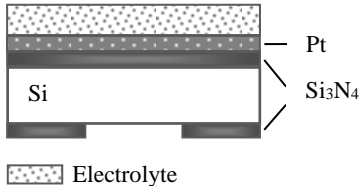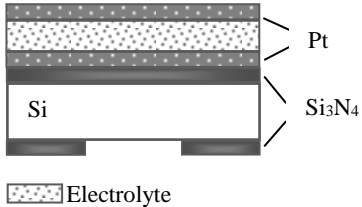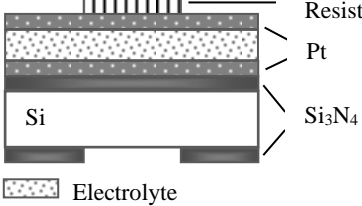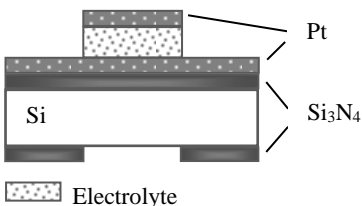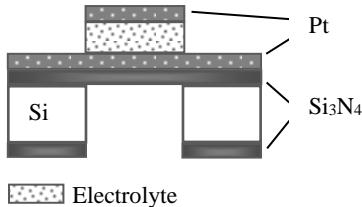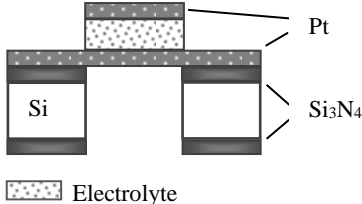
In conclusion, it was demonstrated that the formation of a positive/negative Pt electrode with appropriate properties (porosity, mechanical stability, resistivity) is possible through controlling both deposition conditions (Ar gas pressure in the chamber) during magnetron sputtering process and additional thermal treatment. It was found that correctly chosen formation conditions (argon gas pressure in the chamber) allow minimizing the residual stress in the Pt films down to a magnitude on the order of megapascals. It was observed that the adhesive Ti layer is necessary for the mechanical stability of a Pt electrode and the formation of the PEN three-layered structure.

3.4. The design of technological route and manufacturing of µ-SOFC free-standing membrane

One of the tasks of this dissertation was related to the development of the technological route for the production of µ-SOFC multi-layered membrane structure by using thin film deposition and microelectromechanical system (MEMS) processing techniques. The design of a technological route for the production of micro-solid oxide fuel cell multi-layered membrane structure was improved and implemented. The visualization of technology and manufacturing stages are presented in Table 17.

Table 17. The schematic technological route used for the fabrication of µ-SOFC multi-layered membrane structure

No.	Technological step	Material/Process
1	Si	Double-side polished single crystal Si <100> substrate (n type)
2	Si — Si_3N_4	Chemical vapour deposition (LPCVD) of low-stress Si_3N_4 (it is possible to use SiO_2 instead of Si_3N_4)
3	Si — Si_3N_4	Back-side photolithography and silicon nitride CF_4/O_2 plasma etching

4	Si, Pt, Si₃N₄ diagram	Dc magnetron sputtering of platinum thin film anode
5	Si, Pt, Si₃N₄, Electrolyte diagram	Electron beam evaporation technique for the formation of electrolyte thin film
6	Si, Pt, Si₃N₄, Electrolyte diagram	DC magnetron sputtering of platinum thin film cathode
7	Resist, Pt, Si, Si₃N₄, Electrolyte diagram	Mask alignment and positive photoresist (ma-P 1205) patterning on platinum cathode top surface followed by soft-baking.
8	Si, Pt, Si₃N₄, Electrolyte diagram	Direct Ar^+ ion beam etching of platinum and electrolyte thin film
9	Si, Pt, Si₃N₄, Electrolyte diagram	Back-side high aspect ratio deep reactive ion etching (DRIE)
10	Si, Pt, Si₃N₄, Electrolyte diagram	Silicon nitride CF_4/O_2 plasma etching and release of free-standing membrane

The manufacturing process involved back-side photolithography, magnetron sputtering of platinum thin films, electron beam evaporation of YSZ or GDC

electrolyte, direct Ar^+ ion beam etching of platinum and YSZ or GDC electrolyte thin films, deep reactive ion etching of silicon, and the release of free-standing membrane structure. Test samples of the μ-SOFC three-layered structure, sometimes called PEN (Positive electrode-Electrolyte-Negative electrode) membrane structures, were fabricated.

It should be emphasized that two different technological routes were tested in this research. The initial technological route which is presented in [28] differs from the one given in the Table 17 by steps 5–8. These steps involved: mask alignment and photoresist patterning on the top surface of the Pt anode and, most importantly, the photoresist lift-off process of electrolyte and cathode (Pt) thin films. The suggested technological route for the lift-off process was refused. After several experiments it was observed that during the deposition of thin film on a large area, even if the substrate was not heated up, the photoresist was baked to the film surface in a random place due to hot plasma of electrolyte material reaching the substrate, while the baking temperature of the photoresist is about 125°C. The proposed alternative to the lift-off process was a direct Ar^+ ion beam etching of platinum and the electrolyte thin film.

3.5. The formation of a three-layered structure and prototyping of the μ-SOFC

Three electrode (PEN) structures were produced after determining the basic parameters of preparation of platinum electrodes: argon gas pressure in the chamber and additional thermal annealing. There are several reports [4,10] about producing a PEN structure, but there is insufficient information about the electrolyte growing behaviour on different Pt/Ti thin films' surface and after additional thermal treatment.

In order to characterize the morphology behaviour of the films growing on a dense or porous platinum surface, PEN structures were formed and thermally treated in different ways. Fig. 71 illustrates the $Pt/YSZ/Pt/Ti/SiO_2/Si$ sandwich structure that was formed without any thermal treatment (Fig. 71 (a)).

Afterwards, the whole structure was annealed at optimal conditions (600°C for 15 min) obtaining porous platinum (Fig. 71 (b)). Another three layer structure was prepared in a different technological route. Yttria-stabilized zirconia electrolyte was formed on the $Pt/Ti/SiO_2/Si$ structure, annealed at 600°C for 15 min, and negative Pt electrode was sputtered after the formation of YSZ thin layer (Fig. 71 (c)); then, the entire structure of $Pt/YSZ/Pt/Ti/SiO_2/Si$ was annealed at 600°C for 15 min once more (Fig. 71 (d)).

122
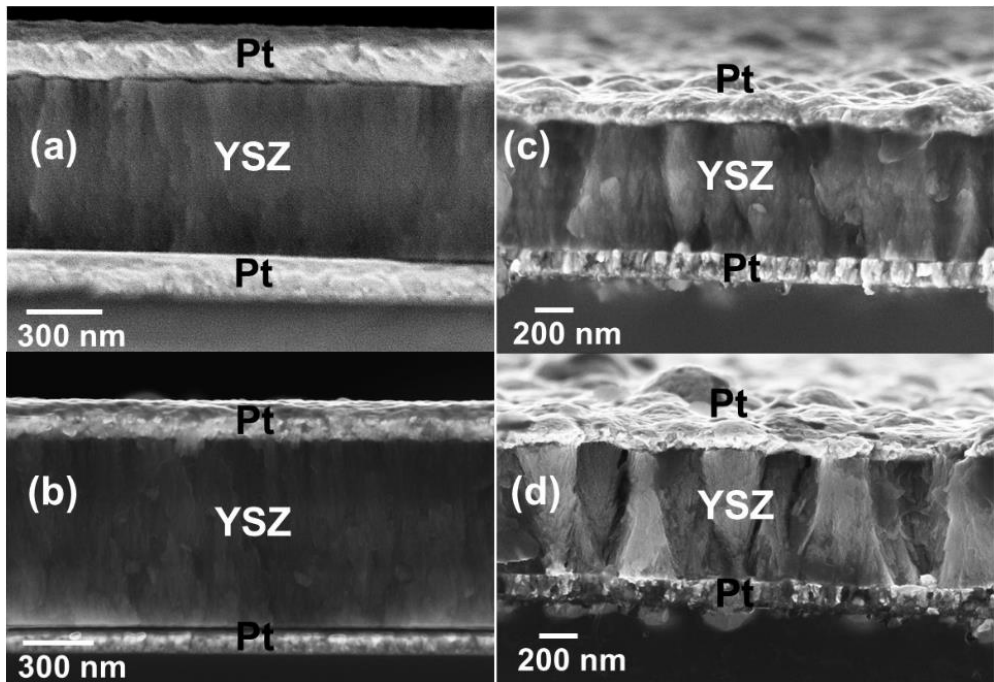
Fig. 71. SEM images of cross-section of three-electrode PEN structures: PEN structure (a) as-deposited and (b) thermally annealed at 600°C for 15 min, respectively; (c) a cross-section of PEN structure, where YSZ was deposited on Pt surface annealed at 600°C for 15 min; (d) PEN structure additionally thermal treated at 600°C for 15 min

The X-ray diffraction patterns of the PEN membrane structures prepared in different ways are displayed in Fig. 72.
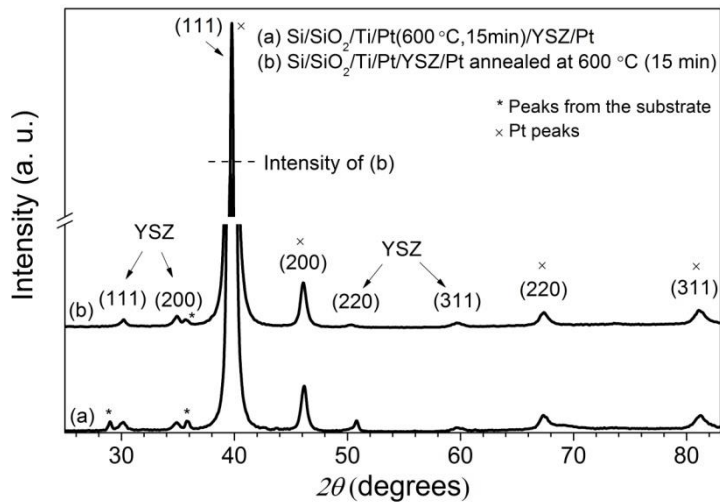
Fig. 72. X-ray diffraction patterns of a PEN membrane structure prepared as follows: on a thermally treated Pt electrode (at 600°C for 15 min) (a) and (b) when the formed PEN structure was annealed at 600°C for 15 min after step-by-step whole structure formation

The peak positions of the (111), (200), (220), (311) reflections correspond to the typical crystal structure of the magnetron sputtered platinum film. In the scan range of $25° \leq 2\theta \leq 90°$, (111), (200), (220) and (311) reflections of the evaporated YSZ thin film were established. It can be assumed that the manufactured structures (electrodes and electrolyte) exhibited cubic crystalline structure with typical columnar growth and grain sizes. From Fig. 72 (a) and (b), it is evident that any drastic changes in the size of crystallites or the composition of the membrane have not been observed.

It is evident that the choice of technological route has a high impact on the resultant surface morphology, as well as porosity, density and growth of the YSZ films. The YSZ film deposited on a low roughness and poreless Pt surface (without any thermal treatment) is uniform and has a dense morphology (Fig. 71 (a)). In contrast, the deposition of YSZ on the thermally annealed Pt (the cross-section of PEN structure (Fig. 71 (c)) demonstrates columnar growth and decreasing density of the YSZ film. This structure leads to lower ionic conductivity, and lower mechanical stability of the final membrane structure. Moreover, it was noticed that a negative Pt electrode sputtered on a bumpy YSZ surface simply replicates its morphology.

If the YSZ surface is too rough, the sputtered platinum thin film (thickness of 200 nm) may not be created and a continuous contact layer could be produced, the electrical short through the YSZ film can be induced. A similar situation was observed for the Pt and PZT structures [196]. Fig. 71 (b) and (d) suggests that the manufacturing conditions have the greatest influence on the surface morphology of the PEN structure compared with the following thermal treatment.

In summary, in order to create a PEN structure exhibiting the required mechanical stability, electrolyte density and porosity of electrodes as well as homogenous contact surface, extra thermal treatment at minimum 600°C temperature after the formation of a tri-layer PEN structure has to be applied.

The designed technological route for manufacturing a μ-SOFC element (PEN structure) was implemented. The fabricated prototype samples are illustrated in Fig. 73.

(a)   (b)

Broken
membrane

(c)
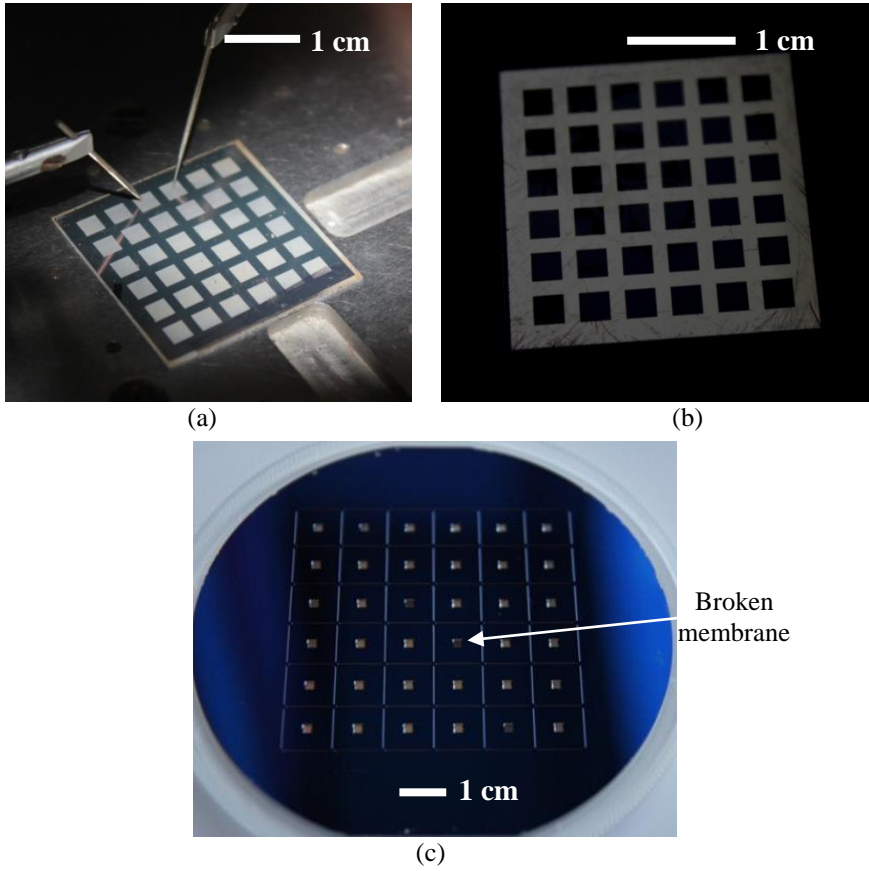
Fig. 73. Test samples of the μ-SOFC (PEN) element: (a) top side (the size of a single membrane is 2.4 x 2.4 mm); (b) back side); (c) free standing membranes (some of them are broken)

4. CONCLUSIONS

1. YSZ and GDC electrolyte ceramics with variable dopant concentration, i.e. (xY$_2$O$_3$ – (1-x)ZrO$_2$), x = 5, 8 and 10 mol%: 5, 8, 10-YSZ; and (xGd$_2$O$_3$ – (1-x)CeO$_2$), x = 10, 12, 15, 18 and 20 mol%: 10, 12, 15, 18, 20-GDC) synthesized by CP synthesis, and CeO$_2$-YSZ ceramic synthesized by the incipient wetness impregnation method are used to prepare the powder. The obtained powder ceramic were used as the targets in the EB-PVD technique for the formation of thin electrolyte films. From the characterization of the electrolyte materials, it was found that the calcination temperature necessary for the formation of a stable single cubic phase structure of 8, 10-YSZ may be reduced from 1500 to 900°C by changing the pH value of the solution from 9 to 6.5.

2. The purposufl selection of technological synthesis parameters (pH value of a solution, process temperature, etc.) and calcination temperature allows to form YSZ and GDC electrolytes exhibiting a fluorite-type structure, thereby higher ionic conductivity. The YSZ and GDC ceramic powder were precipitated with nano-sized crystallites, i.e. in the range of 6–20 and 20–30 nm for YSZ and GDC, respectively.

3. The addition of CeO$_2$ dopant to YSZ ceramic powder (using the impregnation method) do not enhance the ionic conductivity of ceramics (for comparison, the ionic conductivities of 10-YSZ, 10-GDC synthesized by CP synthesis route and impregnated CeO$_2$-YSZ were $5.5 \cdot 10^{-2}$, $1.1 \cdot 10^{-2}$ and $3.4 \cdot 10^{-3}$ S/cm at 750 K temperature, respectively). However, in contrast with YSZ and GDC, CeO$_2$-YSZ thin films exhibited excellent adhesion to the Ni foil substrate, consequently, this structure may be used as an interlayer between the anode and electrolyte.

4. It was proved that the EB-PVD technique is an appropriate method for the formation of a μ-SOFC electrolyte thin films (with a thickness in the range of 500–800 nm) exhibiting the required properties, such as high quality, density, mechanical stability, homogeneity, conductivity, etc. This can be achieved by adjusting a specific composition of the source material (target) used in the evaporation process. It was found that the dopant concentration in the ceramics has to be about 30% higher than the expected concentration in the film (even if the thickness of the film is ~600 nm).

5. Several comparative analyses of impedance spectroscopy measurement devices in a wide range of frequencies (from 1 Hz to 10 MHz) were used in order to evaluate the oxygen ion conduction process in the electrolyte thin films. It is shown that the measurement results strongly depend on the selected impedance spectroscopy measurement method, the quality of the films, the substrate used in the fabrication process, the configuration of Pt electrodes as well as the gap between them (in a case of in-plane configuration), etc. It was determined that the gap of 8 μm between Pt electrodes was optimal in order to assess the ion

conduction mechanisms in 10-YSZ electrolyte thin films through the bulk and grain boundaries.

6. The obtained ionic conductivities and activation energies of YSZ ceramics and thin films reveal the same oxygen vacancy transfer mechanisms; however, the ionic conductivity of the films depends on the structure of the thin film (surface roughness, the growth mechanism, formation of defects, etc.). The measurement applied in-plane and across-plane configurations showed that the ionic conductivity of thin film is lower measuring across the film. 10-YSZ thin film reveals 1.5×10^{-2} and 0.5×10^{-5} S/cm ionic conductivity at 700 K for in-plane and across-plane configuration, respectively.

7. A simplified three-layered μ-SOFC structure has been developed and investigated. It was demonstrated that the formation of a positive/negative Pt electrode with appropriate properties (porosity, microstructure, resistivity), is possible through controlling both deposition conditions, such as Ar gas pressure in the chamber during the magnetron sputtering process and additional thermal treatment (from 400 to 800°C). It was found that 0.065 Pa Ar gas pressure in the chamber and additional thermal treatment at 600°C for 15 min of Pt thin films (with a thickness of 170–200 nm) allow to minimize residual stress in the Pt films down to a magnitude in the order of megapascals (~420 MPa). It was observed that the adhesive Ti layer (thickness of 20 nm) is necessary to improve adhesion between the substrate and Pt electrode as well as the formation of mechanically stable PEN three-layered structure.

8. The improved technological route for the production of a μ-SOFC multi-layered membrane structure by using thin film deposition and microelectromechanical system (MEMS) processing techniques was developed. The manufacturing process during the investigation was modified applying direct Ar^+ ion beam etching of platinum and YSZ or GDC electrolyte thin films instead of lift-off lithography technique in order to increase an effective μ-SOFC membrane network area to (2.4×2.4 cm) (dimensions of one squared membrane are 2.4×2.4 mm) and mechanical stability. The main processes involved back-side photolithography, magnetron sputtering of Pt thin films, electron beam evaporation of YSZ and GDC electrolyte, deep reactive ion etching of silicon, and, finally, the release of a free-standing membrane.

Recommendations

For further ionic conductivity measurements of electrolyte thin films it is recommended to choose the appropriate testing geometry and to follow the optimized way of preparation of the film. Due to the fact that ionic conductivity strongly depends on the quality of the film which may be affected by the roughness of the sample, density of the film, columnar growth etc., it is recommended to use additional annealing of evaporated electrolyte thin films at the temperatures higher than 700°C after forming Pt electrodes.

In testing the geometry it is recommended to increase the distance between Pt electrodes above 10 μm monitoring measurable changes in the wider range of distances, e.g., from 10 to 150 μm. Moreover, to avoid the problem related to laser

cutting, it is proposed to incise the substrate before the deposition of an electrolyte thin film.

REFERENCES

[1]   MUECKE, U.P., et al. Micro Solid Oxide Fuel Cells on Glass Ceramic Substrates. *Adv. Funct. Mater*. 2008, 18, 3158–3168. doi:10.1002/adfm.200700505.

[2]   BIEBERLE-HÜTTER, A., et al. A micro-solid oxide fuel cell system as battery replacement. *J. Power Sources.* 2008, 177, 123–130. doi:10.1016/j.jpowsour.2007.10.092.

[3]   TRAVERSA, E. Toward the miniaturization of solid oxide fuel cells. *Electrochem. Soc. Interface*. 2009, 49–52. [viewed 19/06/2016]. Available from: https://www.electrochem.org/dl/interface/fal/fal09/fal09_p049-052.pdf

[4]   EVANS, A., et al. Micro-solid oxide fuel cells: status, challenges, and chances. *Monatshefte Für Chemie - Chem. Mon.* 2009, 140, 975–983. doi:10.1007/s00706-009-0107-9.

[5]   EVANS, A., et al. Review on microfabricated micro-solid oxide fuel cell membranes. *J. Power Sources.* 2009, 194, 119–129. doi:10.1016/j.jpowsour.2009.03.048.

[6]   ZARKOV, A., et al. Synthesis of nanocrystalline gadolinium doped ceria via sol-gel combustion and sol-gel synthesis routes. *Ceram. Int.* 2015, 42, 3972–3988. doi:10.1016/j.ceramint.2015.11.066.

[7]   ANTONUCCI, V. et al., Integration of µ-SOFC Generator and ZEBRA Batteries for Domestic Application and Comparison with other µ-CHP Technologies. *Energy Procedia*. 2015, 75, 999–1004. doi:10.1016/j.egypro.2015.07.335.

[8]   PANTHI, D. and A. TSUTSUMI. Micro-tubular solid oxide fuel cell based on a porous yttria-stabilized zirconia support. *Sci. Rep.* 2014, 4, 5754. doi:10.1038/srep05754.

[9]   PATIL, T.C. and S.P. DUTTAGUPTA. Micro-Solid Oxide Fuel Cell: A multi-fuel approach for portable applications. *Appl. Energy.* 2016, 168, 534–543. doi:10.1016/j.apenergy.2016.01.111.

[10]   KERMAN, K., B.K. LAI, S. RAMANATHAN. $Pt/Y_{0.16}Zr_{0.84}O_{1.92}/Pt$ thin film solid oxide fuel cells: Electrode microstructure and stability considerations. *J. Power Sources*. 2011, 196, 2608–2614. doi:10.1016/j.jpowsour.2010.10.068.

[11]   REY-MERMET, S., 2008. *Microfabricated Solid Oxide Fuel Cells*. Doctoral dissertation, Swiss Federal Institute of Technology in Lausanne. [viewed 15/07/2016]. Available from: https://infoscience.epfl.ch/record/125690/files/EPFL_TH4175.pdf

[12]   BAE, J., et al. Three-dimensional hexagonal GDC interlayer for area enhancement of low-temperature solid oxide fuel cells. *Surf. Coatings Technol.* 2015, 279, 54–59. doi:10.1016/j.surfcoat.2015.07.066.

[13]   KROGSTAD, H.N., 2012. *Deposition of Thin Film Electrolyte by Pulsed Laser Deposition (PLD) for micro-SOFC Development*. Master thesis, Norwegian University of Science and Technology. [viewed 14/10/2016]

[14]   MUECKE, U.P., et al. Electrochemical performance of nanocrystalline nickel/gadolinia-doped ceria thin film anodes for solid oxide fuel cells. *Solid State Ionics*. 2008, 178, 1762–1768. doi:10.1016/j.ssi.2007.10.002.

[15]   TIMURKUTLUK, B., et al. A review on cell/stack designs for high performance solid oxide fuel cells. *Renew. Sustain. Energy Rev.* 2016, 56, 1101–1121. doi:10.1016/j.rser.2015.12.034.

[16]   CHANDRAN, P.R. and T. V ARJUNAN. A Review of Materials used for Solid

Oxide Fuel Cell. *International Journal of ChemTech Research*. 2015, 7(1), 488–497. ISSN:0974-4290.

[17] PAEK, J.Y. A study on properties of yttrium-stabilized zirconia thin films fabricated by different deposition techniques. *Renew. Energy.* 2014, 65, 202–206. doi:10.1016/j.renene.2013.08.043.

[18] FLEIG, J., et al. Electrodes and electrolytes in micro-SOFCs: a discussion of geometrical constraints. *Solid State Ionics*. 2004, 174, 261–270. doi:10.1016/j.ssi.2004.07.035.

[19] HUANG, H., et al. High-Performance Ultrathin Solid Oxide Fuel Cells for Low-Temperature Operation. *J. Electrochem. Soc.* 2007, 154, B20-B24. doi:10.1149/1.2372592.

[20] RUIZ-MORALES, J.C., et al. Performance of a novel type of electrolyte-supported solid oxide fuel cell with honeycomb structure. *J. Power Sources.* 2010, 195, 516–521. doi:10.1016/j.jpowsour.2009.08.017.

[21] LI, Y., et al. Proton-conducting Micro-solid Oxide Fuel Cells with Improved Cathode Reactions by a Nanoscale Thin Film Gadolinium-doped Ceria Interlayer. *Sci. Rep*. 2016, 6, 1-9. doi:10.1038/srep22369.

[22] WILLIAMS, M., et al. Exergetic Studies of Intermediate-Temperature, Mixed Ionic-Electronic Conducting Solid Oxide Fuel Cell Electrolytes Using the Wagner Mass Transfer Model. *ECS Trans*. 2008, 12, 303–315. doi:10.1149/1.2921556.

[23] GIESBERS, A., 2004. *Development of cathodes for low temperature solid oxide fuel cells Oxygen reduction mechanism*. Master thesis, University of Twente.

[24] KEE, R.J., et al. Solid Oxide Fuel Cells: Operating Principles, Current Challenges, and the Role of Syngas. *Combust. Sci. Technol*. 2008, 180, 1207–1244. doi:10.1080/00102200801963458.

[25] TIETZ, F., H.P. BUCHKREMER, and D. STÖVER. Components manufacturing for solid oxide fuel cells. *Solid State Ionics*. 2002, 152–153, 373–381. doi:10.1016/S0167-2738(02)00344-2.

[26] PANTHI, D., B. CHOI, and A. TSUTSUMI. Fabrication and Evaluation of a Micro-Tubular Solid Oxide Fuel Cell with an Inert Support Using Scandia-Stabilized Zirconia Electrolyte. *J. Electrochem*. Soc. 2015, 162, F1555–F1560. doi:10.1149/2.1031514jes.

[27] LAWLOR, V., et al. Review of the micro-tubular solid oxide fuel cell. Part I. Stack design issues and research activities. *J. Power Sources.* 2009, 193, 387–399. doi:10.1016/j.jpowsour.2009.02.085.

[28] ABAKEVIČIENĖ, B., et al. Modelling and Fabrication of Micro-SOFC Membrane Structure. *Materials Science*. 2014, 20(2), 223–227. ISSN:1392-1320.

[29] SAINIEMI, L., 2009. *Cryogenic Deep Reactive Ion Etching of Silicon Micro and Nanostructures*. Doctoral dissertation, Helsinki University of Technology. [2017-08-14]. http://lib.tkk.fi/Diss/2009/isbn9789512298679/isbn9789512298679.pdf.

[30] FROST, F., et al. Surface engineering with ion beams: From self-organized nanostructures to ultra-smooth surfaces. *Appl. Phys. A Mater. Sci. Process*. 2008, 91, 551–559. doi:10.1007/s00339-008-4516-0.

[31] JACOBSON, A.J. Materials for solid oxide fuel cells. *Chem. Mater.* 2010, 22, 660–674. doi:10.1021/cm902640j.

[32] FERGUS, J.W. Electrolytes for solid oxide fuel cells. *J. Power Sources.* 2006, 162, 30–40. doi:10.1016/j.jpowsour.2006.06.062.

[33] HUI, S. (Rob), et al. A brief review of the ionic conductivity enhancement for selected oxide electrolytes. *J. Power Sources.* 2007, 172, 493–502. doi:10.1016/j.jpowsour.2007.07.071.

[34] FROMHOLD, A. T., eds. *Theory of Metal Oxidation*. Amsterdam (Netherlands): North-Holland Publ. Co, 1980. ISBN: 0-444-853812.

[35] YANG, S.M. et al. Strongly enhanced oxygen ion transport through samarium-doped CeO_2 nanopillars in nanocomposite films. *Nat. Commun.* 2015, 6, 8588. doi:10.1038/ncomms9588.

[36] FIGUEIREDO, F.M.L. and F.M.B. MARQUES. Electrolytes for solid oxide fuel cells. *Wiley Interdiscip. Rev. Energy Environ.* 2013, 2, 52–72. doi:10.1002/wene.23.

[37] HARTMANOVA, M., et al. Correlation between microscopic and macroscopic properties of yttria stabilized zirconia: 1. Single crystals. *Solid State Ionics*. 2000, 136-137, 107–113.

[38] NAVICKAS, E., 2013. *Ion transport at hetero- and homophase boundaries of yttria stabilized zirconia (YSZ) thin films*. Doctoral dissertation, Vienna University of Technology.

[39] HARTMANOVA, M., et al. Thin Film Electrolytes: Yttria Stabilized Zirconia and Ceria. *Russ. J. Electrochem.* 2003, 39, 478–486. doi:10.1023/A:1023864524128.

[40] ZARKOV, A., et al. On the synthesis of yttria-stabilized zirconia: a comparative study. *J. Sol-Gel Sci. Technol.* 2015, 76, 309–319. doi:10.1007/s10971-015-3778-1.

[41] VIAZZI, C., et al. Structural study of metastable tetragonal YSZ powders produced via a sol–gel route. *J. Alloys Compd.* 2008, 452, 377–383. doi:10.1016/j.jallcom.2006.10.155.

[42] UNIVERSITY OF CAMBRIDGE, 2004-2015. *Electrolyte*. In: Teaching and Learning Packages [online]. [viewed 12/04/2016]. Available from: http://www.doitpoms.ac.uk/tlplib/fuel-cells/sofc_electrolyte.php.

[43] SINGHAL, S.C. and K. KENDAL, eds. *High Temperature Solid Oxide Fuel Cells: Fundamentals, design and applications.* UK: Elsevier Advanced Technology, 2003. ISBN: 978-1-85617-387-2

[44] CHOURASHIYA, M.G. and L.D. JADHAV. Synthesis and characterization of 10%Gd doped ceria (GDC) deposited on NiO-GDC anode-grade-ceramic substrate as half cell for IT-SOFC. *Int. J. Hydrogen Energy*. 2011, 36, 14984–14995. doi:10.1016/j.ijhydene.2010.12.083.

[45] ÖKSÜZÖMER, M.A.F., et al. Microstructure and ionic conductivity properties of gadolinia doped ceria (GdxCe1-xO2-x/2) electrolytes for intermediate temperature SOFCs prepared by the polyol method. *Ceram. Int.* 2013, 39, 7305–7315. doi:10.1016/j.ceramint.2013.02.069.

[46] WANG, Y., et al. Low-temperature fabrication and electrical property of 10 mol% Sm_2O_3-doped CeO_2 ceramics. *Sci. Technol. Adv. Mater*. 2003, 4, 229–238. doi:10.1016/S1468-6996(03)00051-2.

[47] BECKEL, D., et al. Thin films for micro solid oxide fuel cells. *J. Power Sources*. 2007, 173, 325–345. doi:10.1016/j.jpowsour.2007.04.070.

[48] LITZELMAN, S.J., et al. Heterogeneously doped nanocrystalline ceria films by grain boundary diffusion: Impact on transport properties. *J. Electroceramics.* 2009, 22, 405–415. doi:10.1007/s10832-008-9445-y.

[49] HSIEH T.H., D.T. RAY, and Y.P. FU. Co-precipitation synthesis and AC conductivity behavior of gadolinium-doped ceria. *Ceram. Int*. 2013, 39, 7967–7973. doi:10.1016/j.ceramint.2013.03.061.

[50] TOK, A.I.Y., L.H. LUO, and F.Y.C. BOEY. Carbonate Co-precipatatioin of Gd_2O_3-doped CeO_2 solid solution nano-particles. *Mater. Sci. Eng. A*. 2004, 383, 229–234. doi:10.1016/j.msea.2004.05.071.

[51] CHIODELLI, G., et al. Synthesis and characterization of $Ce_{0.8}Gd_{0.2}O_2-y$ polycrystalline and thin film materials, Solid State Ionics. 176 (2005) 1505–1512.

doi:10.1016/j.ssi.2005.03.017.

[52]   TULLER, H. Ionic conduction in nanocrystalline materials. *Solid State Ionics*. 2000, 131, 143–157. doi:10.1016/S0167-2738(00)00629-9.

[53]   MORALES, M., et al. Mechanical properties at the nanometer scale of GDC and YSZ used as electrolytes for solid oxide fuel cells. *Acta Mater*. 2010, 58, 2504–2509. doi:10.1016/j.actamat.2009.12.036.

[54]   BIESUZ, M., et al. Conventional and field-assisted sintering of nanosized Gd-doped ceria synthesized by co-precipitation. *Ceram. Int*. 2016, 1–6. doi:10.1016/j.ceramint.2016.04.097.

[55]   MUTHUKKUMARAN, K., et al., Microstructural studies of bulk and thin film GDC. *Ionics*. 2008, 14, 165–171. doi:10.1007/s11581-007-0152-5.

[56]   FUENTES, R.O. and R.T. BAKER. Synthesis and properties of Gadolinium-doped ceria solid solutions for IT-SOFC electrolytes. *Int. J. Hydrogen Energy*. 2008, 33, 3480–3484. doi:10.1016/j.ijhydene.2007.10.026.

[57]   DELL'AGLI, G., et al. Effect of the mineralizer solution in the hydrothermal synthesis of gadolinium-doped (10% mol Gd) ceria nanopowders. *J. Appl. Biomater. Funct. Mater*. 2016, 14, e189-e196. doi:10.5301/jabfm.5000282.

[58]   DÖNMEZ, G., et al. Polyol Synthesis and Investigation of $Ce_{1-x}RE_xO_{2-x/2}$ (RE = Sm, Gd, Nd, La, $0 \leq x \leq 0.25$) Electrolytes for IT-SOFCs. *J. Am. Ceram. Soc*. 2015, 98, 501–509. doi:10.1111/jace.13300.

[59]   JIANG, S.P. A review of wet impregnation - An alternative method for the fabrication of high performance and nano-structured electrodes of solid oxide fuel cells. *Mater. Sci. Eng. A*. 2006, 418, 199–210. doi:10.1016/j.msea.2005.11.052.

[60]   LIU, A.Z., et al. Synthesis and characterization of $Gd_{0.1}Ce_{0.9}O_{1.95}$ nanopowder via an acetic–acrylicmethod. *Ceram. Int*. 2013, 39, 6229–6235. doi:10.1016/j.ceramint.2013.01.044.

[61]   PRASAD, D. H., et al. Superior sinterability of nano-crystalline gadolinium doped ceria powders synthesized by co-precipitation method. *J. Alloys Compd.* 2010, 495, 238–241. doi:10.1016/j.jallcom.2010.01.137.

[62]   IKUMA, Y., et al. X-ray study of cerium oxide doped with gadolinium oxide fired at low temperatures. *Mater. Sci. Eng.* 2003, *B*99, 48–51. doi:10.1016/S0921-5107(02)00546-9.

[63]   ZHA, S., C. XIA, and G. MENG. Effect of Gd (Sm) doping on properties of ceria electrolyte for solid oxide fuel cells. *J. Power Sources*. 2003, 115, 44–48. doi:10.1016/S0378-7753(02)00625-0.

[64]   TIANSHU, Z., et al. Ionic conductivity in the CeO_2–Gd_2O_3 system ($0.05 \leq Gd/Ce \leq 0.4$) prepared by oxalate coprecipitation. *Solid State Ionics*. 2002, 148, 567–573. doi:10.1016/S0167-2738(02)00121-2.

[65]   ARABACI, A. and N. SOLAK. High Temperature - FTIR Characterization of Gadolinia Doped Ceria. *Adv. Sci. Technol.* 2010, 72, 249–254. doi:10.4028/www.scientific.net/AST.72.249.

[66]   ARABACI, A. and M.F. ÖKSÜZÖMER. Preparation and characterization of 10mol% Gd doped CeO_2 (GDC) electrolyte for SOFC applications. *Ceram. Int.* 2012, 38, 6509–6515. doi:10.1016/j.ceramint.2012.05.030.

[67]   LÓPEZ-ROBLEDO, M.J. et al. Processing and mechanical behavior at elevated temperatures of directionally solidified proton conducting perovskites. *J. Eur. Ceram. Soc*. 2010, 31, 1339–1344. doi:10.1016/j.jeurceramsoc.2010.05.022.

[68]   LEE, K.R., J.H. LEE, and H.I. YOO. Grain size effect on the electrical properties of nanocrystalline ceria. *J. Eur. Ceram. Soc.* 2014, 34, 2363–2370. doi:10.1016/j.jeurceramsoc.2014.02.035.

[69]   SHAO, Z., W. ZHOU, and Z. ZHU. Advanced synthesis of materials for intermediate-temperature solid oxide fuel cells. *Prog. Mater. Sci.* 2012, 57, 804–874. doi:10.1016/j.pmatsci.2011.08.002.

[70]   KHARLAMOVA, T., et al. Anode Composites Based on NiO and Apatite-Type Lanthanum Silicate for Intermediate Temperature Solid Oxide Fuel Cells. *Mater. Res. Soc. Symp. Proc (1098-HH07-02)*. 2008, 1098, 3–8.

[71]   FORGERINI, F.L. and R. MARCHIORI. A brief review of mathematical models of thin film growth and surfaces: A possible route to avoid defects in stents. *Biomatter*. 2014, 4, 1–11 [2016-12-01]. http://www.ncbi.nlm.nih.gov/pubmed/24751679.

[72]   CHEN, X., et al. Thin-film heterostructure solid oxide fuel cells. *Appl. Phys. Lett.* 2004, 84, 2700–2702. doi:10.1063/1.1697623.

[73]   SAKALIŪNIENĖ, J., et al. Investigation of Structural and Optical Properties of GDC Thin Films Deposited by Reactive Magnetron Sputtering. *Acta Physica Polonica A*. 2011, 120 (1), 63–65. doi:10.12693/APhysPolA.120.63

[74]   BRIOIS, P. and A. BILLARD. A comparison of electrical properties of sputter-deposited electrolyte coatings dedicated to intermediate temperature solid oxide fuel cells. *Surf. Coatings Technol*. 2006, 201, 1328–1334. doi:10.1016/j.surfcoat.2006.01.061.

[75]   KUO, Y.L., et al. Gadolinia-doped ceria films deposited by RF reactive magnetron sputtering. *Solid State Ionics*. 2009, 180, 1421–1428. doi:10.1016/j.ssi.2009.08.016.

[76]   NAVICKAS, E., et al. Measurement of the across-plane conductivity of YSZ thin films on silicon. *Solid State Ionics*. 2012, 211, 58–64. doi:10.1016/j.ssi.2012.01.007.

[77]   SINGH, J., et al. An Overview: Electron Beam-Physical Vapor Deposition Technology-Present and Future Applications. *Surf. Eng. Sci. Technol. I*. 1999, 59–74. http://www.p2pays.org/ref%5C02/01162.pdf.

[78]   KALININA, E.G., A.A. EFIMOV, and A.P. SAFRONOV. The influence of nanoparticle aggregation on formation of ZrO_2 electrolyte thin films by electrophoretic deposition. *Thin Solid Films*. 2016, 612, 66–71. doi:10.1016/j.tsf.2016.05.039.

[79]   HUANG, H.H., et al. Effects of substrate temperatures on the crystallizations and microstructures of electron beam evaporation YSZ thin films. *J. Alloys Compd.* 2010, 500, 82–86. doi:10.1016/j.jallcom.2010.03.216.

[80]   LAUKAITIS, G. and J. DUDONIS. Microstructure of gadolinium doped ceria oxide thin films formed by electron beam deposition. *J. Alloys Compd*. 2008, 459, 320–327. doi:10.1016/j.jallcom.2007.04.223.

[81]   GALDIKAS, A., et al. Real-time kinetic modeling of YSZ thin film roughness deposited by e-beam evaporation technique. *Appl. Surf. Sci.* 2008, 255, 1929–1933. doi:10.1016/j.apsusc.2008.06.191.

[82]   SAKALIŪNIENĖ, J., et al. Investigation of structural and optical properties of GDC thin films deposited by reactive magnetron sputtering. *Acta Phys. Pol. A*. 2011, 120(1), 63–65. doi:10.12693/APhysPolA.120.63

[83]   HONG, Y.S., et al. Fabrication and characterization GDC electrolyte thin films by e-beam technique for IT-SOFC. *Curr. Appl. Phys.* 2011, S163–S168. doi:10.1016/j.cap.2011.03.071.

[84]   MATTOX, D.M. *Hanbook of Physical Vapor deposition (PVD): Film Formation, Adhesion, Surface, Preparation and Contamination control*. United States of America: Noyes Publications, 1998. ISBN: 0-8155-1422-0.

[85]   WIBOWO, R.A., et al. Single step preparation of quaternary $Cu_2ZnSnSe_4$ thin films by RF magnetron sputtering from binary chalcogenide targets. *J. Phys. Chem. Solids.* 2007, 68, 1908–1913. doi:10.1016/j.jpcs.2007.05.022.

[86]   JUNG, W., J.L. HERTZ, and H.L. TULLER. Enhanced ionic conductivity and phase meta-stability of nano-sized thin film yttria-doped zirconia (YDZ). *Acta Mater.* 2009, 57, 1399–1404. doi:10.1016/j.actamat.2008.11.028.

[87]   LAUKAITIS, G. and D. VIRBUKAS. The structural and electrical properties of GDC10 thin films formed by e-beam technique. *Solid State Ionics.* 2013, 247–248, 41–47. doi:10.1016/j.ssi.2013.05.024.

[88]   RUPP, J.L.M. and L.J. GAUCKLER. Microstructures and electrical conductivity of nanocrystalline ceria-based thin films. *Solid State Ionics.* 2006, 177, 2513–2518. doi:10.1016/j.ssi.2006.07.033.

[89]   INFORTUNA, A., A.S. HARVEY, and L.J. GAUCKLER. Microstructures of CGO and YSZ thin films by pulsed laser deposition. *Adv. Funct. Mater.* 2008, 18, 127–135. doi:10.1002/adfm.200700136.

[90]   LAUKAITIS, G., J. DUDONIS, and D. MILCIUS. Morphology and growth of e-beam deposited YSZ thin films. *Vacuum.* 2007, 81, 1288–1291. doi:10.1016/j.vacuum.2007.01.030.

[91]   SAPORITI, F., et al. Yttria and ceria doped zirconia thin films grown by pulsed laser deposition. *Mater. Res.* 2013, 16, 655–660. doi:10.1590/S1516-14392013005000053.

[92]   UHLENBRUCK, S. et al. Thin film coating technologies of $(Ce,Gd)O_{2-\delta}$ interlayers for application in ceramic high-temperature fuel cells. *Thin Solid Films.* 2007, 515, 4053–4060. doi:10.1016/j.tsf.2006.10.127.

[93]   JI, S. et al. Fabrication of low-temperature solid oxide fuel cells with a nanothin protective layer by atomic layer deposition. *Nanoscale Res. Lett.* 2013, 8, 1–7. doi:10.1186/1556-276X-8-48.

[94]   DUDONIS, J. *Plonų dangų fizika ir nanotechnologijos* [online]. Šiauliai: VšĮ Šiaulių universiteto leidykla. 2007. [viewed 11/11/2015]. e-ISBN 978-609-02-0382-8. Available from: https://www.ebooks.ktu.lt/eb/387/plonu_dangu_fizika_ir_nanotechnologijos/.

[95]   HERRING, D., 2015. *Vapor Pressure and Evaporation in Vacuum Furnaces*. In: Vak Aero International Inc. [online]. [viewed 12/10/2016]. Available from: https://vacaero.com/information-resources/the-heat-treat-doctor/1407-vapor-pressure-and-evaporation-in-vacuum-furnaces.html

[96]   MACKAY, D. and I. VAN WESENBEECK. Correlation of chemical evaporation rate with vapor pressure. *Environ. Sci. Technol.* 2014, 48, 10259–10263. doi:10.1021/es5029074.

[97]   TARANCÖN, A. Strategies for lowering solid oxide fuel cells operating temperature. *Energies*. 2009, 2, 1130–1150. doi:10.3390/en20401130.

[98]   TSIPIS, E. V. and V. V. KHARTON. Electrode materials and reaction mechanisms in solid oxide fuel cells: A brief review : I Electrochemical behavior vs. materials science aspects. *J. Solid State Electrochem.* 2008, 12, 1367–1391. doi:10.1007/s10008-008-0611-6.

[99]   CURTIN, S., et al. Development of Fuel Cell and Hydrogen 2OO9-2O1O. *Technol. Roadmap*. 2014, 22, 55–62. doi:10.1039/b105764m.

[100]   PRESTAT, M., J.F. KOENIG, and L.J. GAUCKLER. Oxygen reduction at thin dense $La_{0.52}Sr_{0.48}Co_{0.18}Fe_{0.8}2O_{3-\delta}$ electrodes: Part I: Reaction model and faradaic impedance. *J. Electroceramics*. 2007, 18, 87–101. doi:10.1007/s10832-007-9012-y.

[101]   HERTZ, J.L., 2006. *Microfabrication methods to improve the kinetics of the yttria stabilized zirconia-platinum-oxygen electrode*. Doctor of Phylosophy in Materials Science and Engineering, Massachusetts Institute of Technology.

[102]   CHAO, C.C., et al. Improved solid oxide fuel cell performance with nanostructured

134

electrolytes. *ACS Nano*. 2011, 5(7), 5692–5696. doi:10.1021/nn201354p.

[103] TSUCHIYA, M., B.K. LAI, and S. RAMANATHAN. Scalable nanostructured membranes for solid-oxide fuel cells. *Nat. Nanotechnol.* 2011, 6, 282–286. doi:10.1038/nnano.2011.43.

[104] AN, J., et al. Three-dimensional nanostructured bilayer solid oxide fuel cell with 1.3 W/cm2 at 450 C. *Nano Lett.* 2013, 13, 4551–4555. doi:10.1021/nl402661p.

[105] AGUSTSSON, J.S., et al. Growth, coalescence, and electrical resistivity of thin Pt films grown by dc magnetron sputtering on SiO2. *Appl. Surf. Sci.* 2008, 254, 7356–7360. doi:10.1016/j.apsusc.2008.05.335.

[106] CHANG, I., et al. Characterization of porous Pt films deposited via sputtering. *Appl. Surf. Sci.* 2013, 282, 463–466. doi:10.1016/j.apsusc.2013.05.153.

[107] AGUSTSSON, J.S., et al. Electrical resistivity and morphology of ultra thin Pt films grown by dc magnetron sputtering on SiO_2. *Journal of Physics: Conference Series, IOP Publishing*. 2008, 100, 82006. doi:10.1088/1742-6596/100/8/082006.

[108] TOGHAN, A., et al. Microstructure of thin film platinum electrodes on yttrium stabilized zirconia prepared by sputter deposition. *Thin Solid Films*. 2011, 519, 8139–8143. doi:10.1016/j.tsf.2011.06.018.

[109] CONFORTO, E. and P.E. SCHMID. Platinum silicide phase transformations controlled by a nanometric interfacial oxide layer. *Thin Solid Films.* 2008, 516, 7467–7474. doi:10.1016/j.tsf.2008.03.033.

[110] TIGGELAAR, R.M., et al. Stability of thin platinum films implemented in high-temperature microdevices. *Sensors Actuators A Phys.* 2009, 152, 39–47. doi:10.1016/j.sna.2009.03.017.

[111] BUCHANAN, D.J. and R. JOHN. Residual stress redistribution in shot peened samples subject to mechanical loading. *Mater. Sci. Eng. A*. 2014, 615, 70–78. doi:10.1016/j.msea.2014.06.118.

[112] WANG, K., K. YAO, and S.J. CHUA. Titanium diffusion and residual stress of platinum thin films on Ti/SiO2/Si substrate. *J. Appl. Phys.* 2005, 98, 013538. doi:10.1063/1.1949715.

[113] NAM, H.J., D.K. CHOI, and W.J. LEE. Formation of hillocks in Pt/Ti electrodes and their effects on short phenomena of PZT films deposited by reactive sputtering. *Thin Solid Films*. 2000, 371, 264–271. doi:10.1016/S0040-6090(00)00970-6.

[114] SREEMANY, M. and S. SEN. Effect of substrate temperature and annealing temperature on the structural, electrical and microstructural properties of thin Pt films by rf magnetron sputtering. *Appl. Surf. Sci.* 2006, 253, 2739–2746. doi:10.1016/j.apsusc.2006.05.040.

[115] BAERTSCH, C.D., et al. Fabrication and structural characterization of self-supporting electrolyte membranes for a micro solid-oxide fuel cell. *J. Mater. Res.* 2011, 19, 2604–2615. doi:10.1557/JMR.2004.0350.

[116] SHIM, J.H., et al. Atomic layer deposition of yttria-stabilized zirconia for solid oxide fuel cells. *Chem. Mater.* 2007, 19, 3850–3854. doi:10.1021/cm070913t.

[117] SU, P.C., et al. Solid oxide fuel cell with corrugated thin film electrolyte. *Nano Lett.* 2008, 8, 2289–2292. doi:10.1021/nl800977z.

[118] GRIGALIŪNAS, V., et al. Two-step Fabrication of Large Area SiO2/Si Membranes. *Mater. Sci.* 2012, 18, 325–329.

[119] GARBAYO, I., et al. Electrical characterization of thermomechanically stable YSZ membranes for micro solid oxide fuel cells applications. *Solid State Ionics*. 2010, 181, 322–331. doi:10.1016/j.ssi.2009.12.019.

[120] JOHNSON, A.C., et al. An experimental investigation into micro-fabricated solid oxide fuel cells with ultra-thin $La_{0.6}Sr_{0.4}Co_{0.8}Fe_{0.2}O_3$ cathodes and yttria-doped

zirconia electrolyte films. *J. Power Sources.* 2009, 186, 252–260. doi:10.1016/j.jpowsour.2008.10.021.

[121] LAI, B.K., K. KERMAN, and S. RAMANATHAN. Methane-fueled thin film micro-solid oxide fuel cells with nanoporous palladium anodes. *J. Power Sources*. 2011, 196, 6299–6304. doi:10.1016/j.jpowsour.2011.03.093.

[122] TAKAGI, Y., S. ADAM, and S. RAMANATHAN. Nanostructured ruthenium - Gadolinia-doped ceria composite anodes for thin film solid oxide fuel cells. *J. Power Sources*. 2012, 217, 543–553. doi:10.1016/j.jpowsour.2012.06.060.

[123] FAN, Z., et al. Thickness effects of yttria-doped ceria interlayers on solid oxide fuel cells. *J. Power Sources.* 2012, 218, 187–191. doi:10.1016/j.jpowsour.2012.06.103.

[124] KERMAN, K., B.K. LAI, and S. RAMANATHAN. Free standing oxide alloy electrolytes for low temperature thin film solid oxide fuel cells. *J. Power Sources.* 2012, 202, 120–125. doi:10.1016/j.jpowsour.2011.11.062.

[125] KERMAN, K., et al. Elastic configurations of self-supported oxide membranes for fuel cells. *J. Power Sources.* 2013, 222, 359–366. doi:10.1016/j.jpowsour.2012.08.092.

[126] KIM, K.J., et al. Micro solid oxide fuel cell fabricated on porous stainless steel: a new strategy for enhanced thermal cycling ability *Sci. Rep.* 2016, 6, 22443. doi:10.1038/srep22443.

[127] HA, S., P.C. SU, and S.W. CHA. Combinatorial deposition of a dense nano-thin film YSZ electrolyte for low temperature solid oxide fuel cells. *J. Mater. Chem. A.* 2013, 1, 9645. doi:10.1039/c3ta11758h.

[128] JI, S., et al. On the reduced electrical conductivity of radio-frequency sputtered doped ceria thin film by elevating the substrate temperature. *Curr. Appl. Phys*. 2016, 16, 324–328. doi:10.1016/j.cap.2015.12.011.

[129] KWON, C.W., et al. The thermomechanical stability of micro-solid oxide fuel cells fabricated on anodized aluminum oxide membranes. *J. Power Sources.* 2012, 210, 178–183. doi:10.1016/j.jpowsour.2012.03.020.

[130] NOH, H.S., et al. Thermo-mechanical stability of multi-scale-architectured thin-film-based solid oxide fuel cells assessed by thermal cycling tests. *J. Power Sources.* 2014, 249, 125–130. doi:10.1016/j.jpowsour.2013.10.101.

[131] KUNDRACIK, F., et al. Ohmic resistance of thin yttria stabilized zirconia film and electrode-electrolyte contact area. *Mater. Sci. Eng. B Solid-State Mater. Adv. Technol.* 2001, 84, 167–175. doi:10.1016/S0921-5107(01)00515-3.

[132] ARONSSON, B.O., J. LAUSMAA, and B. KASEMO. Glow discharge plasma treatment for surface cleaning and modification of metallic biomaterials. *J. Biomed. Mater. Res.* 1997, 35, 49–73.

[133] CORREIA, D.M., et al. Superhydrophilic poly(l-lactic acid) electrospun membranes for biomedical applications obtained by argon and oxygen plasma treatment. *Appl. Surf. Sci*. 2016, 371, 74–82. doi:10.1016/j.apsusc.2016.02.121.

[134] KELLY, P. and R. ARNELL. Magnetron sputtering: a review of recent developments and applications. *Vacuum*. 2000, 56, 159–172. doi:10.1016/S0042-207X(99)00189-X.

[135] BORAH, S.M. Direct Current Magnetron Glow Discharge Plasma Characteristics Study for Controlled Deposition of Titanium Nitride Thin Film. *Hindavi Publishing Corporation*: *Journal of Materials.* 2013, 2013, 1–6. doi:10.1155/2013/852859.

[136] SAFI, I. Recent aspects concerning DC reactive magnetron sputtering of thin films: a review. *Surf. Coatings Technol.* 2000, 127, 203–219. doi:10.1016/S0257-8972(00)00566-1.

[137] BISWAS, A., et al. Advances in top-down and bottom-up surface nanofabrication:

136

Techniques, applications & future prospects. *Adv. Colloid Interface Sci.* 2012, 170, 2–27. doi:10.1016/j.cis.2011.11.001.

[138] WU, B., A. KUMAR, and S. PAMARTHY. High aspect ratio silicon etch: A review. *J. Appl. Phys.* 2010, 108. doi:10.1063/1.3474652.

[139] BETANCOURT, T. and L. BRANNON-PEPPAS. Micro-and nanofabrication methods in nanotechnological medical and pharmaceutical devices. I*nt. J. Nanomedicine.* 2006, 1, 483–495. doi:10.2147/nano.2006.1.4.483.

[140] CHEN, K. et al. Effect of Process Parameters on the Surface Morphology and Mechanical Performance of Silicon Structures After Deep Reactive Ion Etching (DRIE). *J. Microelectromechnaical Syst.* 2002, 11, 264–275. doi:10.1109/JMEMS.2002.1007405.

[141] HOODA, M.K. et al. A systematic study of DRIE process for high aspect ratio microstructuring. VACUUM. 2010, 84, 1142–1148. doi:10.1016/j.vacuum.2010.01.052.

[142] BAHNG, M.K., et al. Current technologies for analysis of biomass thermochemical processing: A review. *Anal. Chim. Acta.* 2009, 651, 117–138. doi:10.1016/j.aca.2009.08.016.

[143] BOYD, J.W., et al. The use of a thermogravimetric analyzer for the generation of primary analytical vapor standards of organophosphate pesticides. *Anal. Chim. Acta.* 2006, 558, 35–41. doi:10.1016/j.aca.2005.11.001.

[144] RUFFELL, A. and P. WILTSHIRE. Conjunctive use of quantitative and qualitative X-ray diffraction analysis of soils and rocks for forensic analysis. *Forensic Sci. Int.* 2004, 145, 13–23. doi:10.1016/j.forsciint.2004.03.017.

[145] LUTTEROTTI, L., et al. Texture, residual stress and structural analysis of thin films using a combined X-ray analysis. *Thin Solid Films.* 2004, 450, 34–41. doi:10.1016/j.tsf.2003.10.150.

[146] LEONI, M., et al. X-ray Diffraction Methodology for the Microstructural Analysis of Nanocrystalline Powders : Application to Cerium Oxide. *J. Am. Ceram. Soc.* 2004, 87, 1133–1140. doi:10.1111/j.1551-2916.2004.01133.x.

[147] X-RAY OPTICAL SYSTEMS, 2017. *Parallel beam X-ray diffraction analysis*. In: Technologies [online]. [viewed 15/04/2016]. Available from: https://xos.com/technologies/xrd/parallel-beam-x-ray-diffraction/.

[148] LE BOURHIS, E., et al. Mechanical properties of hard AlCrN-based coated substrates. *Surf. Coatings Technol.* 2009, 203, 2961–2968. doi:10.1016/j.surfcoat.2009.03.017.

[149] WELZEL, U., M. LEONI, and E.J. MITTEMEIJER. The determination of stresses in thin films; modelling elastic grain interaction. *Philos. Mag.* 2003, 83, 603–630. doi:10.1080/0141861021000042299.

[150] RENAULT, P.O., et al. Damage mode tensile testing of thin gold films on polyimide substrates by X-ray diffraction and atomic force microscopy. *Thin Solid Films.* 2003, 424, 267–273. doi:10.1016/S0040-6090(02)01127-6.

[151] VAZ, F., et al. Residual stress states in sputtered $Ti_{1-x}Si_xN_y$ films. *Thin Solid Films.* 402 (2002) 195–202. doi:10.1016/S0040-6090(01)01675-8.

[152] GOUDEAU, P., et al. Characterization of thin film elastic properties using X-ray diffraction and mechanical methods: Application to polycrystalline stainless steel. *Thin Solid Films.* 2001, 398–399, 496–500. doi:10.1016/S0040-6090(01)01464-X.

[153] ANGELOV, T., et al. Thermo-mechanical transduction suitable for high-speed scanning probe imaging and lithography. *Microelectron. Eng.* 2016, 154, 1–7. doi:10.1016/j.mee.2016.01.005.

[154] GOŁEK, F., et al. AFM image artifacts. *Appl. Surf. Sci.* 2014, 304, 11–19.

doi:10.1016/j.apsusc.2014.01.149.

[155] GADELMAWLA, E.S., et al. Roughness parameters. *J. Mater. Process. Technol.* 2002, 123, 133–145. doi:10.1016/S0924-0136(02)00060-2.

[156] ZHANG, T., et al. AFM measurements of adhesive forces between carbonaceous particles and the substrates. *Nucl. Eng. Des.* 2015, 293, 87–96. doi:10.1016/j.nucengdes.2015.06.022.

[157] SUTTON, M.A., et al. Scanning electron microscopy for quantitative small and large deformation measurements Part I: SEM imaging at magnifications from 200 to 10,000. *Exp. Mech.* 2007, 47, 775–787. doi:10.1007/s11340-007-9042-z.

[158] KRYSZTOF, M. and W. SŁÓWKO. Optimisation of secondary electron detector for variable pressure SEM with Monte Carlo method. *Vacuum.* 2008, 82, 1075–1078. doi:10.1016/j.vacuum.2008.01.017.

[159] JIRUŠE, J., M. HAVELKA, and F. LOPOUR. Novel field emission SEM column with beam deceleration technology. *Ultramicroscopy.* 2014, 146, 27–32. doi:10.1016/j.ultramic.2014.05.006.

[160] ARONNIEMI, M., J. SAINIO, and J. LAHTINEN. Aspects of using the factor analysis for XPS data interpretation. *Surf. Sci.* 2007, 601, 479–489. doi:10.1016/j.susc.2006.10.010.

[161] LI, J.C., Y. WANG, and D.C. BA. Characterization of Semiconductor Surface Conductivity by Using Microscopic Four-Point Probe Technique. *Phys. Procedia.* 2012, 32, 347–355. doi:10.1016/j.phpro.2012.03.568.

[162] MIRONOV, V.S. et al. Comparison of electrical conductivity data obtained by four-electrode and four-point probe methods for graphite-based polymer composites. *Polym. Test.* 2007, 26, 547–555. doi:10.1016/j.polymertesting.2007.02.003.

[163] CESIULIS R.G., H., TSYNTSARU N., and A. RAMANAVICIUS. The study of thin films by electrochemical impedance spectroscopy. In: *Nanostructures and Thin Films for Multifunctional Applications.* Switzerland: Springer, 2016, pp. 3–35 [2016-07-14]. ISBN 978-3-319-30198-3. doi:10.1007/978-3-319-30198-3.

[164] GOMADAM, P.M. and J.W. WEIDNER. Analysis of electrochemical impedance spectroscopy in proton exchange membrane fuel cells. *Int. J. Energy Res.* 2005, 29, 1133–1151. doi:10.1002/er.1144.

[165] LI, J.G., et al. Reactive 10 mol% RE_2O_3 (RE = Gd and Sm) doped CeO_2 nanopowders: Synthesis, characterization, and low-temperature sintering into dense ceramics. *Mater. Sci. Eng. B Solid-State Mater. Adv. Technol.* 2005, 121, 54–59. doi:10.1016/j.mseb.2005.03.001.

[166] KEŽIONIS, A., et al. Four-electrode impedance spectrometer for investigation of solid ion conductors. *Rev. Sci. Instrum.* 2013, 84, 013902-1–013902-8. doi:10.1063/1.4774391.

[167] GERSTL, M., et al. The separation of grain and grain boundary impedance in thin yttria stabilized zirconia (YSZ) layers. *Solid State Ionics.* 2011, 185, 32–41. doi:10.1016/j.ssi.2011.01.008.

[168] ZARKOV, A., et al. On the synthesis of yttria-stabilized zirconia: a comparative study. *J. Sol-Gel Sci. Technol.* 2015, 76, 309–319. doi:10.1007/s10971-015-3778-1.

[169] DROŻDŻ-CIEŚLA, E., A. MAŁECKI, and B. JAJKO. Mechanism of thermal decomposition of zirconyl oxalate $ZrOC_2O_4$. *J. Therm. Anal. Calorim.* 2008, 92, 939–944. doi:10.1007/s10973-007-8878-x.

[170] DESHPANDE, A.S., et al. Improved chemical route for quantitative precipitation of lead zirconyl oxalate (PZO) leading to lead zirconate (PZ) powders. *Mater. Lett.* 2001, 51, 161–171. doi:10.1016/S0167-577X(01)00284-1.

[171] GLASNER, A., E. LEVY, and M. STEINBERG. Thermal decomposition of yttrium

oxalate in vacuum and in various atmospheres. *J. Inorg. Nucl. Chem.* 1963, 25, 1119–1127. doi:http://dx.doi.org/10.1016/0022-1902(63)80132-3.

[172] VASYLKIV, O. Nonisothermal Synthesis of Yttria-Stabilized Zirconia Nanopowder through Oxalate Processing: II, Morphology Manipulation. *J. Am. Ceram. Soc.* 2001, 88, 2484–2488. doi:10.1111/j.1151-2916.2001.tb01040.x.

[173] WENDLANDT, W.W., T.D. George, and G.R. Horton. The Thermal Decomposition of Thorium (IV), Uranium (IV), and the Rare-Earth Metal (III) Differential Thermal Analysis and Weight-Loss Studies. *J. Inorg. & Nuclear Chem*. 1959, 273, 280–286.

[174] COURTIN, E. et al. A composite sol-gel process to prepare a YSZ electrolyte for Solid Oxide Fuel Cells. *J. Power Sources.* 2012, 206, 77–83. doi:10.1016/j.jpowsour.2012.01.109.

[175] TADOKORO, S.K., et al. Synthesis, sintering and impedance spectroscopy of 8 mol% yttria-doped ceria solid electrolyte. *J. Power Sources*. 2004, 130, 15–21. doi:10.1016/j.jpowsour.2003.11.073.

[176] ZHANG, Y.W., et al. Electrical conductivity enhancement in nanocrystalline (RE2O3)(0.08)(ZrO2)(0.92) (RE=Sc, Y) thin films. *Appl. Phys. Lett.* 2000, 77, 3409–3411. doi:10.1063/1.1328099.

[177] FONSECA, F.C. and R. MUCCILLO. Impedance spectroscopy analysis of percolation in (yttria-stabilized zirconia)-yttria ceramic composites. *Solid State Ionics*. 2004, 166, 157–165. doi:10.1016/j.ssi.2003.10.002.

[178] WU, S.G., et al. Y_2O_3 stabilized ZrO_2 thin films deposited by electron beam evaporation: Structural, morphological characterization and laser induced damage threshold. *Appl. Surf. Sci.* 2006, 253, 1561–1565. doi:10.1016/j.apsusc.2006.02.044.

[179] TANHAEI, M. and M. MOZAMMEL. Yttria-stabilized zirconia thin film electrolyte deposited by EB-PVD on porous anode support for SOFC applications. *Ceram. Int*. 2017, 43, 3035–3042. doi:10.1016/j.ceramint.2016.11.097.

[180] BERNARD, B. et al. Thermal insulation properties of YSZ coatings: Suspension Plasma Spraying (SPS) versus Electron Beam Physical Vapor Deposition (EB-PVD) and Atmospheric Plasma Spraying (APS). *Surf. Coatings Technol.* 2016. doi:10.1016/j.surfcoat.2016.06.010.

[181] ZHA, S., et al. GDC-Based Low-Temperature SOFCs Powered by Hydrocarbon Fuels. *J. Electrochem. Soc.* 2004, 151, A1128–A1133. doi:10.1149/1.1764566.

[182] LI, X. et al. Synthesis and electrical properties of $Ce_{1-x}Gd_xO_{2-x/2}$ (x = 0.05-0.3) solid solutions prepared by a citrate-nitrate combustion method. *Ceram. Int.* 2012, 38, 3203–3207. doi:10.1016/j.ceramint.2011.12.025.

[183] HENNINGS, U. and R. REIMERT. Investigation of the structure and the redox behavior of gadolinium doped ceria to select a suitable composition for use as catalyst support in the steam reforming of natural gas. *Appl. Catal. A Gen.* 2007, 325, 41–49. doi:10.1016/j.apcata.2007.02.054.

[184] HONG, J., S.J. HONG, and A. V VIRKAR. Lattice Parameters and Densities of Rare-Earth Oxide Doped Ceria Electrolytes. *J. Am. Ceram. Soc.* 1995, 78 , 433–439. doi:10.1111/j.1151-2916.1995.tb08820.x.

[185] PÉREZ-COLL, D., et. al. Effects of firing conditions and addition of Co on bulk and grain boundary properties of CGO. *Solid State Ionics*. 2005, 176, 2799–2805. doi:10.1016/j.ssi.2005.06.023.

[186] ANANTHARAMAN, S.B. and R. BAURI. Effect of sintering atmosphere on densification, redox chemistry and conduction behavior of nanocrystalline Gd-doped CeO_2 electrolytes. *Ceram. Int.* 2013, 39, 9421–9428. doi:10.1016/j.ceramint.2013.05.059.

[187] HUANG, K., M. FENG, and J.B. GOODENOUGH. Synthesis and Electrical

Properties of Dense $Ce_{0.9}Gd_{0.1}O_{1.95}$ Ceramics. *J. Am. Ceram. Soc.* 1998, 81(2), 357–362. 10.1111/j.1151-2916.1998.tb02341.x/pdf

[188] MURALIDHARAN, P., S.H. JO, and D.K. KIM. Electrical conductivity of submicrometer gadolinia-doped ceria sintered at 1000 °C using precipitation-synthesized nanocrystalline powders. *J. Am. Ceram. Soc.* 2008, 91, 3267–3274. doi:10.1111/j.1551-2916.2008.02644.x.

[189] GERSTL, M., et al. The grain and grain boundary impedance of sol-gel prepared thin layers of yttria stabilized zirconia (YSZ). *Solid State Ionics.* 2012, 225, 732–736. doi:10.1016/j.ssi.2012.02.012.

[190] WANZENBERG E., et al. Influence of electrode contacts on conductivity measurements of thin YSZ electrolyte films and the impact on solid oxide fuel cells. *Solid State Ionics.* 2003, 164, 121–129. doi:10.1016/j.ssi.2003.08.053.

[191] GOURBA, E., et al. Electrical properties of gadolinia-doped ceria thin films deposited by sputtering in view of SOFC application. *J. Solid State Electrochem.* 2004, 8, 633–637. doi:10.1007/s10008-004-0503-3.

[192] YAMAGUCHI, T., et al. Fabrication and characterization of high performance cathode supported small-scale SOFC for intermediate temperature operation. *Electrochem. Commun.* 2008, 10, 1381–1383. doi:10.1016/j.elecom.2008.07.013.

[193] SUZUKI, T., I. KOSACKI, and H.U. ANDERSON, Microstructure-electrical conductivity relationships in nanocrystalline ceria thin films. *Solid State Ionics.* 2002, 151, 111–121. doi:10.1016/S0167-2738(02)00589-1.

[194] BRIOIS, P., et al. Microstructure - Electrical properties relationship of YSZ thin films reactively sputter-deposited at different pressures. *Ionics*. 2005, 11, 301–305. doi:10.1007/BF02430393.

[195] PEREDNIS, D. and L.J. GAUCKLER. Solid oxide fuel cells with electrolytes prepared via spray pyrolysis. *Solid State Ionics.* 2004, 166, 229–239. doi:10.1016/j.ssi.2003.11.011.

[196] MARDARE, C.C. et al. Effects of adhesion layer (Ti or Zr) and Pt deposition temperature on the properties of PZT thin films deposited by RF magnetron sputtering. *Appl. Surf. Sci.* 2005, 243, 113–124. doi:10.1016/j.apsusc.2004.09.050.

[197] KANG, U., T. LEE, and Y.H. KIM. Pt/Ti Thin Film Adhesion on SiNx/Si Substrates. *Jpn. J. Appl. Phys.* 1999, 38, 4147–4151. doi:10.1143/JJAP.38.4147.

[198] ABE, K., et al. Pzt thin film preparation on pt-ti electrode by rf sputtering. *Jpn. J. Appl. Phys*. 1991, 30, 2152–2154. doi:10.1143/JJAP.30.2152.

[199] SEDLAČEK, M., B. PODGORNIK, and J. VIŽINTIN. Correlation between standard roughness parameters skewness and kurtosis and tribological behaviour of contact surfaces. *Tribol. Int.* 2012, 48, 102–112. doi:10.1016/j.triboint.2011.11.008.

[200] CROSA, M., BOERO, V., and M. FRANCHINI-ANGELA. Determination of mean crystallite dimensions from X-ray diffraction peak profiles: a comparative analysis of synthetic hematities. *Clays and Clay Minerals.* 1999, 47, 742–747.

[201] HAUK, V. *Non-destructive methods o f measurement o f residual stresses*. In: Niku-Lari, A., eds. Advances in Surface Treatments: Technology-Applications-Effects: International Guidebook on Residual Stresses. 1987, Vol. 4, UK: Pergamon Press. ISBN 0-08-034062-8.

[202] MORET, M., et al. Damage after annealing and aging at room temperature of platinized silicon substrates. *Thin Solid Films.* 2003, 434, 283–295. doi:10.1016/S0040-6090(03)00453-X.

[203] TAMULEVIČIUS, S. Stress and strain in the vacuum deposited thin films. *Vacuum*. 1998, 51, 127–139. doi: 10.1016/S0042-207X(98)00145-6